POLITECNICO DI TORINO

SCUOLA DI DOTTORATO
Dottorato in Fisica – XXVII ciclo

Tesi di Dottorato

Experimental study of iron-based superconductors: advanced characterization and fundamental properties.

Paola Pecchio

Tutore
Prof. Dario Daghero

Coordinatore del corso di dottorato
Prof.ssa Arianna Montorsi

Febbraio 2015

Abstract

Iron-based superconductors (SCs) were discovered in 2008 and their specific features immediately captured the great interest of the scientific community. The critical temperature of these compounds was the highest known so far with the exception of cuprates. They show a layered crystal structure and quasi-2D Fermi surface, made up of multiple disconnected sheets, and usually with multiple order parameters. Their parent (undoped) compounds are metals and the proximity to magnetism, clearly visible in the phase diagram of these materials, seems to be of fundamental importance in order to understand the superconductivity in Fe-based SCs. Their observed features have led theoretical physicist to propose an unconventional, spin fluctuation-mediated pairing. Many experimental results obtained so far seem to confirm the theoretical predictions, but the final validation of this model still requires additional steps.

The research on Fe-based materials has been recently boosted by the progress in the techniques of film deposition. Films of very high quality are necessary for applications in superconducting electronics, i.e. for the fabrication of Josephson junctions, SQUIDs and so on. However, they can be fruitfully used also to investigate fundamental properties of these compounds (especially for those materials that cannot be grown easily in the form of single crystals). For instance, they are the perfect playground for transport, optical and spectroscopic measurements of various kind; thin films offer an additional way to tune the critical temperature, thanks to strain/stress effects that can be induced by the substrate; finally, they are necessary to realize some proposed phase-sensitive experiments to determine the order parameter symmetry s++ or s± [1]. Many other experimental measurements and theoretical calculations are crucial in order to clarify some open points for example the superconducting order parameter and its symmetry, the amplitude and the number of the energy gaps and their temperature dependence.

This dissertation presents the advanced characterization and the fundamental study of Fe-based superconductors (122 and 11 families) mainly in the form of epitaxial thin films by means of different experimental techniques, namely electrical transport measurements, point-contact Andreev-reflection spectroscopy (used both for advanced characterization and fundamental investigation) and other techniques for the morphological and chemical characterization of the surface (AFM, FESEM, Energy-dispersive X-ray spectroscopy).

This research was developed within the activities of the Eu-Japan project IRON SEA (establishing the basic science and technology for Iron-based superconducting electronics applications) funded within the Seventh Framework Programme FP7 under grant number 283141. The epitaxial thin films of 122 and 11 superconductors were grown by partners of the consortium that are world leaders in this field, and thus they are high-quality state-of-the-art samples. In particular, the Co-doped Ba-122 films were deposited by the group of prof. B. Holzapfel at IFW Dresden, while the Fe(Te,Se) films were grown by the group of prof. A. Maeda at Tokyo University.

The data collected by means of the aforementioned techniques allowed the systematic characterization and the study of the homogeneity of the superconducting properties and of

the chemical composition at the surface, and also the effects of aging and degradation (especially for Ba-122 samples). In the framework of the IRON SEA project, this large amount of information was required in order to assess the possible use of these films for the development of superconducting electronic devices.
From the point of view of the fundamental properties, the PCARS study of the Co-doped Ba-122 and Fe(Te,Se) thin films allowed gathering information about the phase diagram of these materials, i.e. the effect of isovalent and aliovalent doping on the critical temperature (T_c) and on the superconducting gaps (i.e. number, amplitude and symmetry) – or, conversely, the determination of the trend of the gaps as a function of doping and critical temperature. Thanks to a theoretical analysis of the results carried out by Dr. G. Ummarino within the multi-band Eliashberg theory, the results of PCARS measurements allowed extracting the characteristic energy of the mediating boson, verifying the spin-fluctuation mechanism, determining the evolution of the coupling constants from the underdoped to the overdoped regime.
The activity of the candidate has been focused on the experimental aspects of the research. She spent two months (October - December 2012) at IFW Dresden during which she carried out a part of the PCARS measurements on Co-doped Ba-122 films (otherwise carried out at Politecnico di Torino) and contributed to their characterization (i.e. by DC Resistivity, RHEED and X-ray Spectroscopy) as discussed in *chapter 4*. The characterization of these films was completed at Politecnico of Torino by AFM, FESEM and EDX measurements, performed by F. Laviano and M. Raimondi and later analysed by the candidate. Similarly for Fe(Te,Se) films, widely characterized by the Japanese partner, the research was mainly focused on PCARS and transport measurements (*chapter 5*).

The layout of this work is the following:

Chapter 1 gives an introduction on the Fe-based superconductors and shows the interconnection between this work and the state of the art of this topic.

Chapter 2 is a brief overview on the theoretical key points concerning the coupling mechanism in superconductors, with a special attention to the electron-boson coupling in unconventional Fe-based superconductors. Also the symmetry and the amplitude of the order parameter (OP) are discussed here. The final part of the chapter is devoted to point-contact Andreev-reflection spectroscopy (the main technique used in this study) from the theoretical point of view.

Chapter 3 presents the experimental techniques used in this study. The general experimental features of resistivity and point-contact Andreev-reflection spectroscopy measurements are discussed here.

Chapter 4 is devoted to the study of different Co-doped Ba-122 thin films. The homogeneity of the morphological, structural and superconductive properties was verified by using different and complementary techniques. The number and the temperature dependence of the amplitude of the energy gaps are investigated by the candidate by means of

point-contact Andreev-reflection spectroscopy within the BTK model. The PCARS spectra were also analyzed within the Eliashberg theory.

Chapter 5 presents the results of the study of different Se-doped Fe($Te_{1-x}Se_x$) thin films. The resistivity measurements are here reported and the PCARS measurements were fit by using the BTK model and also analysed within the Eliashberg theory.

Chapter 6 presents the general conclusions and the prospective research in this field.

Acknowledgements

I would like to thank my PhD supervisor, prof. Dario Daghero, for supporting me during this three-year work. His commitment to scientific research and to teaching Physics was a great example for me.
A special thanks is devoted to prof. Marina Putti, the referee of this work.
I am also greteful to the group of Superconductivity of Politecnico di Torino: prof. Renato Gonnelli, the head of the group; Dr. Giovanni Ummarino for theoretical discussions and calculations; Mauro Tortello for the help in solving many experimental problems; Francesco Laviano for constructive technical discussions; to all the partners involved in Iron Sea Eu-Japan project in particular prof. Kazumasa Iida, Fritz Kurth, Vadim Grinenko and prof. Tajima. I would like also to thank Mauro Raimondi for technical support in FESEM and EDX measurements.

Vorrei ringraziare i miei genitori, Margherita e Franco, per l'affetto con cui mi hanno sostenuto in questi anni di studio e i miei amici Laura, Massimo e Antonio per avermi aiutato a coltivare anche in questi anni la passione per la Fisica.
Infine rivolgo un ringraziamento speciale a mio marito Paolo, a cui dedico questo lavoro.

Contents

Chapter 1

Introduction

The study of Fe-based superconductors (SCs) is one of the most fruitful fields of present research in superconductivity. These materials, discovered in 2008 [3], represent the first class of superconductors with critical temperature above 50 K after the discovery of the cuprates, the first class of high T_c SCs, in 1986 [4]. It was completely unexpected to find superconductivity in these materials because the presence of iron in their crystal lattice makes their parent compounds strongly magnetic and, historically, magnetism and superconductivity were considered antagonists. Many other interesting features were found in Fe-based SCs. For example, the high critical fields, the multiband electronic structure, the unprecedent sensitivity of the superconducting properties to the structural parameters and the unconventional boson-mediating superconductivity were of great interest for both fundamental reasons and possible applications in transport or electronics and open new avenue in research.
Nowadays five different crystallographic structures (see Fig. 1.1) that support superconductivity have been discovered and they allow defining the classes of Fe-based materials. All exhibit a crystal structure of square planar layers of Fe atoms joined by tetrahedrally coordinated pnictogen (arsenic or phosphorus) or chalchogen (sulfur, selenium or tellurium) atoms. Between these layers, alkali, alkaline-earth, or rare-earth and oxygen/fluorine blocking layers can be also placed. It is universally recognized that the interaction that leads to the high T_c superconductivity originates within the common iron layers.
The generic phase diagram of the Fe-based SCs can be produced by manipulating the chemical or structural properties, by using either chemical doping/substitution or applied external pressure to drive an antiferromagnetic (AFM), non-superconducting parent compound to a superconducting (SC), non-AFM state which occurs in close proximity to the long range-ordered antiferromagnetic ground state in these materials [6]. For example in 122 Fe-based SCs, chemical doping, i.e. partial substitution, of Fe dopants elements, for example Co, Ni [7] or Ru [8], can suppress magnetism [9] on behalf of superconductivity. On the contrary, in 1111 Fe-based compounds, isoelectronic Ru substitutions of Fe can also suppress progressively SDW without the induction of superconductivity [10].
In Fig. 1.2 the schematic phase diagram for 122 family of iron-based superconductors is shown. In this example Ba atoms can be substituted with K atoms (doping with holes), Fe

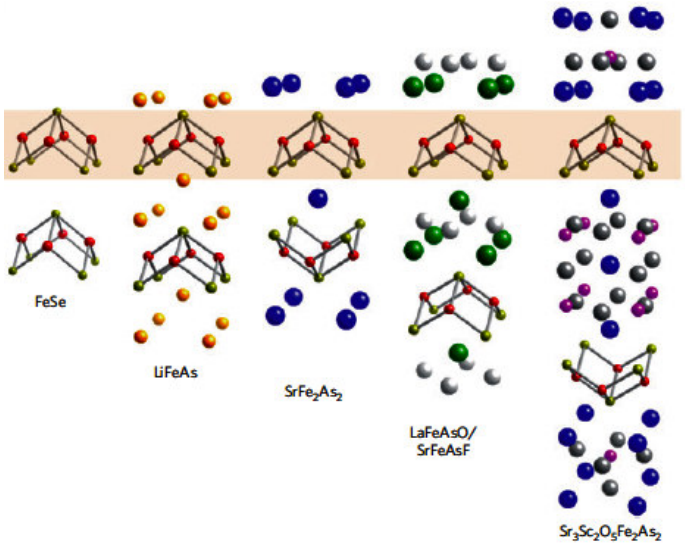

Figure 1.1: The five tetragonal structures of the Fe-based SCs groups adapted from [5].

atoms can be substituted with Co atoms (doping with electrons) or Fe atoms can be substituted with Ru atoms (or As atoms by P atoms), to suppress magnetism without changing the carrier concentration. Therefore, the magnetic and electronic structures of these ma-

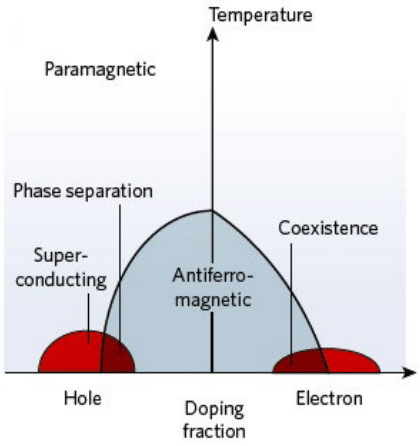

Figure 1.2: Schematic phase diagram for the Ba-122 iron-based superconductors adapted from [11].

terials turns out to play a crucial role in determining the shape of the phase diagram and the charge doping is not the only factor for inducing these compounds to superconductive phase. Even if many open questions still remain on this point, the proximity to a magnetic quantum critical point suggest that magnetic spin fluctuation are instrumental for the electron pairing.
The interplay between magnetism and superconductivity in Fe-based SCs is still under debate, especially due to the implication of this topic for the pairing mechanism. The

electronic structure of their parent compounds suggests that the same magnetic interactions that drive the AFM ordering also produce the pairing state for superconductivity [12]. First-principles DFT calculations and experimental results agree on the idea that the dominant contribution to the electronic density of states at Fermi level (E_F) derives from metallic bonding of the iron *d*-electron orbitals in the iron pnictogen (or chalcogen) layers. These form several bands that cross E_F, both electron-like and hole-like, resulting in multiband system dominated by iron *d* character. This electronic structure suggests that the same magnetic interactions that drive the AFM ordering also produce the pairing state for superconductivity [12].
Theoretical DTF calculations contributed to clarify the shape of the Fermi surface (FS) in Fe-based SCs. A 2D unit cell with two Fe atoms per cell, and the corresponding reciprocal lattice cell were used in the calculations of the FS reported in Fig. 1.3. In these cases, the x and y directions are along the next-nearest-neighbor Fe-Fe bond. Multi-sheet Fermi surface that are separated into two distinct sets of surfaces appeared. In strictly nonmagnetic calculations, when the magnetic moment on each Fe is restricted to zero, two or more hole-like Fermi surfaces near the Γ point [$\mathbf{k} = (0, 0)$], and two electron-like surfaces near the M point [$\mathbf{k} = (\pi, \pi)$] are visible [13].

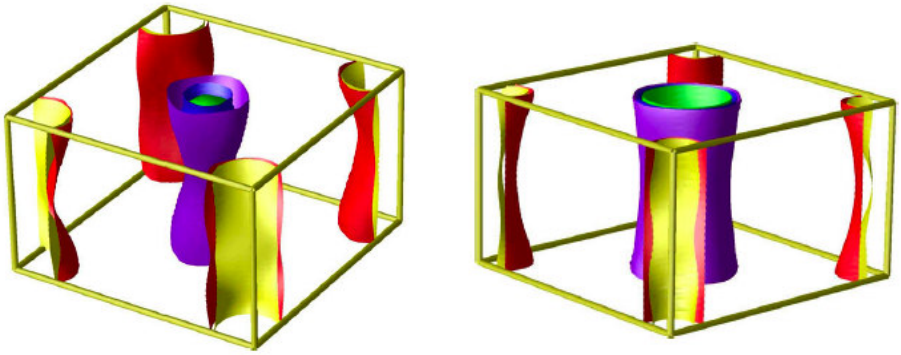

Figure 1.3: (left panel)The Fermi surface of the nonmagnetic $BaFe_2As_2$ for 10% e-doping (Co doping, virtual crystal approximation) [12]. (right panel) The Fermi surface of the nonmagnetic $BaFe_2As_2$ for 10% h-doping (20% Cs doping, virtual crystal approximation) adapted from [12].

It turned out that the density of states (DOS) for holes and electrons is comparable for undoped materials in 122 systems and in 1111 systems. Usually, the doping makes dominant the DOS for electrons or for holes. Theoretical predictions are in agreement with ARPES measurements performed on 1111 [14] and 122 family [15, 16, 17]. These measurements demonstrated the existence of a well-defined FS that consists of hole and electron pockets. Therefore, the location and the relative size of the individual FS sheets agree with the local-density approximation (LDA) expectation, even if the ARPES bandwidth is reduced from these calculations by a factor of $2 - 2.5$, similar to materials with strong itinerant magnetic fluctuations [18]. Also quantum oscillation measurements on P-doped 1111 compounds agree quite well with structure calculations [19] and confirm the mass renormalization as ARPES [20]. Quantum oscillation data on antiferromagnetic 122 compounds [21] indicate that a significant portion of the Fermi surface disappears due to the

opening of a magnetic gap, even if even the undoped pnictides are well-defined Fermi liquids. The frequencies of the magneto-oscillations suggest that the ordered magnetic state has small Fermi surface pockets consistent with the formation of a spin-density wave [12]. A theoretical study underlines the similarity in the electronic states between 11 family superconductors (FeS, FeSe, and FeTe) and the 122 family [22]. Even if the crystalline structure of the Fe-chalcogenides is the simplest among the Fe-based superconductors, the contributions of Fe-3d electrons near the Fermi level and the morphology of the Fermi surface (shown in 1.4) exhibit similarities to the FeAs-based superconductors [23]. This similarity between the FS of the Ba 122 compounds and the $Fe_{1+\delta}Te_{1-x}Se_x$ single crystals is supported by ARPES measurements [24].

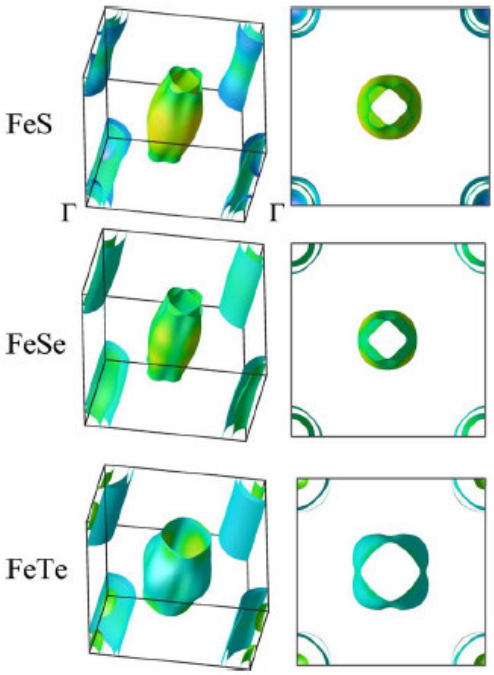

Figure 1.4: LDA Fermi surface of FeS, FeSe, and FeTe from calculations LDA [22]

The general idea is that superconductivity in Fe-based compounds is due to unconventional (non-phonon-mediated) interband pairing mechanism, due to magnetic spin fluctuation. The fundamental mechanism that causes the high temperature in the Fe-based superconductivity is a question of primary importance and since the exact nature of the pairing in not known, many experimental and theoretical efforts have been done in order to determine the pairing symmetry and still need. Experimental measurements of neutron scattering [25] and angle resolved-photoemission spectroscopy (ARPES) [26, 27] pointed out a fully gapped order parameter consistent with $s-$wave symmetry, that was theoretically predicted to have $s-$wave symmetry but with a sign change between different bands in the complex multiband electronic structure. This so called s± superconductivity in which the

sign of the order parameter changes between two sets of Fermi surfaces was theoretical predicted [28, 29]. Experiments probing the order parameter symmetry and amplitude of the superconducting energy gaps provide important information about the energy and momentum dependence of Cooper pairing, helping elucidate the pairing mechanism in this new class of high T_c superconductors.

Although the fundamental research is traditionally focused on single crystals for their high quality and homogeneity, it is a matter of a fact that the research on Fe-based superconductors has been recently boosted by the progress in the technique of film deposition. The synthesis of high quality films is the indispensable step towards the fabrication of superconducting electronic devices that in most cases have Josephson junctions as their basis constituting element [30, 31]. Moreover, thin films turns out to show many interesting characteristics also in fundamental research activity. First, they are more suitable than single crystals for investigation of transport and optical properties, thanks to possibility to control their shape by lithography and also thank to the strong directionality of the structures of these systems (i.e. epitaxial orientation of the grains is one of the typical characteristics of these systems). Second, thin films allow exploring the effects of lattice deformation by strain/stress (hardly accessible in single crystals) on structural parameters, surface morphology, transport and fundamental properties [32, 33, 34].

In the last three years, in the framework of two EU-Japan projects within the Seventh Framework Programme FP7, namely SUPERIRON and IRON SEA, the research on iron-based superconductors thin films was carried out properly in order to establish the basic properties of Fe-based SCs, to explore the technological perspectives, for Iron-based superconducting electronic applications, and also to open up new possibility in this field. The research discussed in this PhD dissertation was developed in the framework of the IRON SEA project, funded within the Seventh Framework Programme FP7 under grant number 283141.

After the characterization of epitaxial Co-doped Ba-122 and Fe(Te,Se) thin films by means of experimental techniques, i.e. AFM, FESEM, Energy-dispersive X-ray spectroscopy, DC resistivity, point-contact Andreev-reflection spectroscopy (PCARS), the fundamental study of these systems was carried out mainly by means of PCARS measurements. The effect of isovalent and aliovalent doping on the critical temperature and on the superconducting gaps (i.e. number, amplitude and symmetry) was investigated. The experimental PCARS spectra were also analysed within the multi-band Eliashberg theory in order to verify the spin-fluctuation mechanism and determine the evolution of the coupling constants from the underdoped to the overdoped regime.

Chapter 2

Unconventional Gap features of Fe-based Superconductors

The complex doping-dependent Fermi surface (FS), the predicted sensitivity of the order parameter (OP) to fine structural details and the electron-boson coupling in Fe-based superconductors (SCs) are introduced in this chapter. These crucial aspects are discussed maily within the case of Pnictides and Chalcogenides, the two Fe-based families studied in this work. In this prospective, the main topics of this research, i.e. the study of the amplitude, the symmetry and the number of the energy gaps as well as the coupling constant of the Fe-bases SCs thin films by the means of point-contact Andreev-reflection spectroscopy, are stressed in order to underline the unexpected results obtained in this research.

2.1 BCS theory: key points

The first microscopic theory of superconductivity was published by Bardeen, Cooper and Schrieer (BCS) in 1957. One of the main prediction of the BCS theory is the existence of an energy gap 2Δ at the Fermi level which is the energy up to the electron states are filled up in a normal metal. In a BCS superconductor below T_c the electron density of states acquires a small gap 2Δ separating the occupied and unoccupied states. This gap is fixed at the Fermi energy, and so it does not prevent electrical conduction, unlike a band gap in a semiconductor or insulator.
In 1960 Gork'ov was able to use the BCS theory to derive the Ginzburg-Landau equations, and hence give a microscopic explanation of the OP that is one of the key point in the superconducting state, since it determines how the charge carriers couple to form Cooper pairs. Gork'ov not only found that the OP is directly related to the wave function for the Cooper pairs, but that it is also directly proportional to the gap parameter Δ [37]. The BCS energy gap 2Δ corresponds to the energy for breaking up a pair into two free electrons. Therefore, in the BCS [38, 39] the order parameter was identified with the "pair function". It was pointed out for the first time that the superconductivity is a phonon-mediated phenomenon. Despite this theory is not suitable for all superconductors, especially for

Fe-based superconductors, nevertheless the electron-phonon interaction theory remains a fundamental key to understand the idea of the attractive interaction between electrons in superconductivity.

2.1.1 The electron-phonon interaction

The first key idea in the BCS theory is that there is an effective attraction for electrons near the FS. While bare electrons repel each other strongly with the electrostatic Coulomb repulsion, this is no more valid for quasiparticles. A quasiparticle is an excitation of a solid consisting of a moving electron together with a surrounding exchange correlation hole [37]. It turns out that the bare Coulomb interaction between two electrons (e^2/r) leads to a repulsive element ($4\pi e^2/r$). This interaction is screened by the other electrons and also by the positive ions in the lattice, i.e. the electrons interacts via their interaction with the phonons on the crystal lattice.
Reading through the Feynman diagram the meaning of this process, one electron emits a virtual phonon, it propagates for a while, and it is then absorbed by a second electron. The net effect of the process is to transfer momentum $\hbar\mathbf{q}$ from one electron to the other. Therefore it implies an effective interaction between electrons.
This effective interaction between the electrons due to exchange of phonons turns out to be of the form:

$$V_{eff}(\mathbf{q},\omega) = |g_{eff}|^2 \frac{1}{\omega^2 - \omega_D^2} \tag{2.1}$$

where the virtual phonon has wave vector $\mathbf{q}$ and frequency $\omega_{\mathbf{q}}$. The parameter g_{eff} is related to the matrix element for scattering an electron from state $\mathbf{k}$ to $\mathbf{k}+\mathbf{q}$ and ω_D is the typical phonon frequency, usually the Debye frequency of the phonons. This is an attractive interaction for phonon frequencies ω which are less than ω_D and repulsive for $\omega > \omega_D$. In BCS theory, only electrons which lie within $\pm k_B T$ of the Fermi energy are taking into accounts. At the temperatures of interest to superconductivity, the regime considered is $\hbar\omega_D \gg k_B T$. Therefore BCS interaction can be approximatively written in the form

$$V_{eff}(\mathbf{q},\omega) = -|g_{eff}|^2 \qquad |\omega| < \omega_D. \tag{2.2}$$

The Hamiltonian for the effective electron-electron interaction is then

$$H_{eff} = -|g_{eff}|^2 \sum_{\mathbf{k},\mathbf{q}} \sum_{\sigma} c^{+}_{\mathbf{k}_1+\mathbf{q}\sigma_1} c^{+}_{\mathbf{k}_2+\mathbf{q}\sigma_2} c_{\mathbf{k}_1,\sigma_1} c_{\mathbf{k}_2,\sigma_2} \tag{2.3}$$

The energy of electrons that are involved in the process is restricted within the range $\pm\hbar\omega_D$ of the FS, $|\epsilon_{\mathbf{k}_i} - \epsilon_F| < \hbar\omega_D$. Therefore, interacting electrons lie near the FS, but the Bloch states far inside or outside it are not involved in this process.

2.1.2 The BCS energy gap and quasiparticle states

Actually this is only the first step in the BCS theory. Passing through many other key steps such as the determination of the full BCS state in which every electron at the FS is

part of a pair and writing down a many-particle wave function in which every electron is paired [37], the Eq. 2.3 becomes approximately

$$H_{BCS} = \sum_{\mathbf{k},\sigma}(\epsilon_{\mathbf{k}} - \epsilon_F)c^+_{\mathbf{k}\sigma}c_{\mathbf{k}\sigma} + \sum_{\mathbf{k}}(c^+_{\mathbf{k}\uparrow}c^+_{-\mathbf{k}\downarrow}\Delta + \Delta^* c_{-\mathbf{k}\downarrow}c_{\mathbf{k}\uparrow}) \tag{2.4}$$

where the new crucial quantity

$$\Delta = -|g_{eff}|^2 \sum_{\mathbf{k}'}\langle c_{-\mathbf{k}\downarrow}c_{\mathbf{k}'\uparrow}\rangle \tag{2.5}$$

was introduced.
The eigenvalues of 2.4 are the energies

$$E_{\mathbf{k}} = \sqrt{(\epsilon_{\mathbf{k}} - \epsilon_F)^2 + |\Delta|^2}. \tag{2.6}$$

The parameter Δ is the amplitude of the OP. Δ is also called the "energy gap" in the superconductor. It is the distance, in energy, between the condensate of Cooper pairs and the first single-particle excitation [37].
Determining the expectation value from the solutions to the BCS Hamiltonian, it is possible to obtain

$$\Delta = |g_{eff}|^2 \sum_{\mathbf{k}} \frac{\Delta}{2E_{\mathbf{k}}} \tanh\left(\frac{E_{\mathbf{k}}}{2k_BT}\right). \tag{2.7}$$

Then if the sum is converted into an integral over energy, the BCS gap equation is calculated

$$1 = \lambda \int_0^{\hbar\omega_D} d\epsilon \frac{1}{E} \tanh\left(\frac{E}{2k_BT}\right) \tag{2.8}$$

where $E = \sqrt{\epsilon^2 + |\Delta|^2}$ and $\lambda = |g_{eff}|^2 g(\epsilon_{E_F})$ is the dimensionless electron-phonon coupling parameter.
The BCS gap equation implicitly determines the gap $\Delta(T)$ at any temperature T. This is the central equation of the BCS theory, since it predicts both the transition temperature T_c and the value of the energy gap at zero temperature $\Delta(0)$.
From the BCS gap equation, taking the limit $\Delta \to 0$ one can obtain the equation for T_c

$$k_BT_c = 1.13\hbar\omega_D \exp(-1/\lambda) \tag{2.9}$$

which has almost exactly the same form as the formula for the binding energy in the Cooper problem. At $T = 0$ also $\Delta(0)$ can be determined, obtaining the formula

$$2\Delta(0) = 3.53k_BT_c. \tag{2.10}$$

This value of the gap is obeyed from one-band weak-coupling low T_c superconductors like aluminum [40].
Even if some Fe-based SCs exhibited a small BCS-like gap as in the case of $SmFeAsO_{0.85}F_{0.15}$ [41], usually in Fe-based SCs the coupling parameter is no longer small. Therefore it is necessary to include the real boson spectrum and the strong electron-boson coupling provided by Eliashberg theory described in section 2.3.2.

2.2 Anisotropy of the energy gap

In general, $\Delta(k)$ can be expanded in a series of spherical functions, which are often labeled as atomic orbitals for example (s, p, d) according to the corresponding value of the internal momentum ℓ of the pairs.
In the previous section, Δ were shown in the simplest form given by the BCS theory. In this theory, it depends only on the modulus of the momentum $\mathbf{k}$, i.e. the gap parameter is independent on the $\mathbf{k}$ direction in momentum space. Due to the spherical symmetry adopted, this is called "isotropic $s-$wave" symmetry.
The **s-wave gap symmetry** is the basis function having $\ell = 0$. The gap is isotropic (i.e. it has the same amplitude at every point of the FS), everywhere positive and real and its phase is everywhere zero (see Fig. 2.1). In this case it can be represented as a single real number

$$\Delta(\phi) = \Delta_0. \tag{2.11}$$

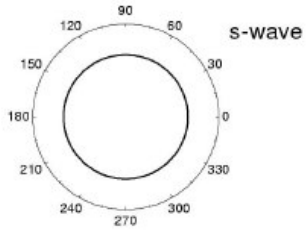

Figure 2.1: Polar plots for the isotropic $s-$wave order parameter in the "angular momentum representation", together with the phase as the function of the ϕ angle.

If the energy gap changes on the FS, it can be written as follow:

$$\Delta(\mathbf{k}) = \int V(\mathbf{k},\mathbf{k}')\Delta(\mathbf{k}') \left[\int_0^{k_B\theta_D} \frac{d\epsilon}{\sqrt{\epsilon^2 + \Delta(\mathbf{k}')^2}} \tanh\left(\frac{\sqrt{\epsilon^2 + \Delta(T)^2}}{2k_BT} \right) \right] dN' \tag{2.12}$$

where $dN' = dS'/4\pi^3\hbar v'_F$ is the infinitesimal element of the density of states associated with the infinitesimal element of area dS' of the Fermi surface. In Eq. 2.12 the summation is over all the bands crossing the Fermi level. The dependence of the pairing interaction $V(\mathbf{k},\mathbf{k}')$ on $\mathbf{k}$ gives rise different values of the energy gap, i.e. to the anisotropy of the amplitude of the OP.
Therefore within the research field of high-temperature superconductors, more complex gap symmetries than the BCS one have been investigated. Phase variations of the OP can indeed mean that the sign change of $\Delta(\mathbf{k})$ and that the symmetry is admitted to be lower than the crystal one. Regions of opposite sign can be separated by nodal lines. For example s means "no nodal lines", p "one nodal lines", d "two nodal lines", according to to the corresponding value of the internal momentum ℓ of the pairs. Actually not all the possible terms of the expansion are allowed in a given compound. For example, if pairs

are spin singlets, ℓ can take only values $\ell = 0,2,4...$ to ensure that the pair wavefunction is symmetric. The problem of determining the gap symmetries that are allowed or forbidden in Fe-based compounds is still a hot topic and will be discuss in the following section.
Some other possible symmetries, which are relevant for the present work, are here presented. The basis functions of the order parameter are described in the 2D form. Since the pairing is limited to electrons with momentum near $\mathbf{k}_F$, the angular variable ϕ so that $\mathbf{k} = k_F(\cos\phi, \sin\phi)$ can be used in the "angular momentum representation" [42]. The qualitative polar plot of the gap amplitude is also shown in some cases.
The **anisotropic s-wave gap symmetry**, can be expressed as

$$\Delta(\phi) = \Delta_0[(1-\epsilon) + \epsilon\cos(2\phi)^4] \tag{2.13}$$

Also in this case the OP is real and positive, the phase is zero but the magnitude diminishes in the $k_y \pm k_x$ directions. In Fig.2.2 the function is shown for the case $\epsilon = 0.3$.

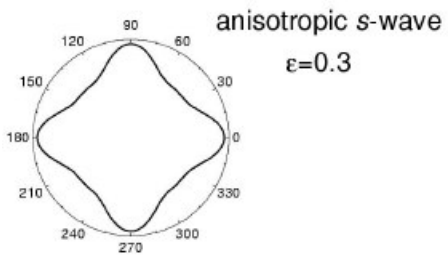

Figure 2.2: Polar plots for the $s-$*anisotropic* wave order parameter in the "angular momentum representation".

The **d-wave symmetry** includes two different basis functions each of them with $\ell = 2$. The gap in the $d_{x^2-y^2}$ symmetry can be represented in the reciprocal k space as:

$$\Delta(\phi) = \Delta_0\cos(2\phi) = \Delta_0[\cos(\phi)^2 - \sin(\phi)^2] \tag{2.14}$$

The gap is real and it is zero for $\phi = \pi/4 + n\pi/2$ (see Fig. 2.3), i.e. along the $k_y = \pm k_x$ lines (nodal lines) and displays four lobes in the directions of the axes. The plot of the gap phase shows that its sign changes when a nodal line is crossed. The maximum (minimum) gap value is reached along the k_x (k_y) axis. The other basis function gives the d_{xy} symmetry which is expressed by:

$$\Delta(\phi) = \Delta_0\sin(2\phi) = 2\Delta_0(\cos\phi\sin\phi) \tag{2.15}$$

In this case, the nodal lines coincide with the axes (in practice, this is the previous symmetry rotated by an angle of $\pi/4$). The situation in which the degree of the symmetry of the order parameter is lower than the crystal's one is usually referred to as unconventional pairing. For instance this is the case of the high temperature superconductivity in cuprate superconductors [43].

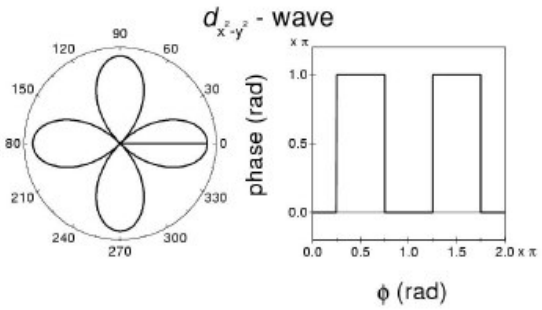

Figure 2.3: Polar plots for the $d-$wave order parameter in the "angular momentum representation", together with the phase as the function of the ϕ angle.

Symmetry of the OP in Fe-based SCs

The general idea on the symmetry of the OP in Fe-based compounds is the $s\pm$ symmetry model, which combines s-wave symmetry with a sign change of the OP. In Fig. 2.4 a schematic representation of the $s\pm$ OP is reported with the OPs discussed in this section.

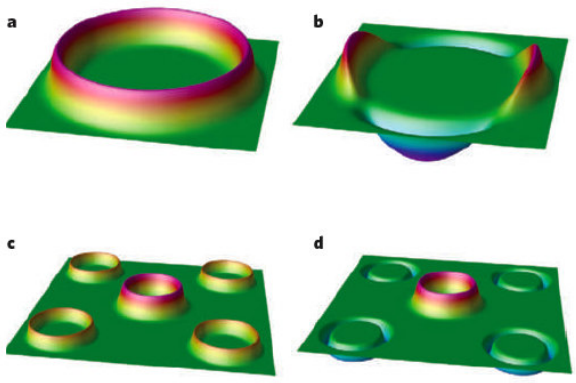

Figure 2.4: Schematic representation of the superconducting order parameter in different cases: a conventional, uniform, s wave symmetry (a); d wave symmetry (b); two-band s wave with the same sign symmetry (c); $s\pm$ wave symmetry (d) [11].

ARPES measurements on hole-doped 122 systems [15] probed a fully gapped OP consistent with a fully symmetric s-wave symmetry [28]. Gaps with different amplitude on different FS sheets are universally accepted for 122-compounds [27]. Theoretical calculations on electron-doped systems supported a peculiar FS, consisting of multiple sheets with $s\pm$ pairing symmetry [28]. Later on also full gaps in both electron and hole bands but with opposite signs of the order parameters between two were predicted [12]. Three-dimensional nodal structures were predicted to appear in the largely warped hole Fermi surface having a strong $Z^2/XZ/YZ$ orbital character [44] on isovalent doping 122 Fe-based superconductors. The presence of nodes in some 122 system is an open point, despite some experimental

evidence of these theoretical predictions. A nodal symmetry such as $d-$wave has been proposed to explain resistivity and thermal conductivity measurements [45, 46] as well as line nodes to justify the results of penetration depth, thermal transport and NMR measurents [47, 48]. Also Raman spectroscopy [49] and directional conductivity [50] seems to support accidental nodes within general $s\pm$wave symmetry. Despite many evidence and the few phase-sensitive experiments performed on Fe-based SCs [51, 52] that seems to confirm the $s\pm$ pairing symmetry, the definitive response is still missing.

2.3 Coupling mechanism in multi-band superconductors

If the Fermi surface is composed of different sheets, as in Fe-based superconductors, the energy gap can be different on each of them giving rise to the multi-band superconductivity. Multi-band superconductivity can be also regarded as a specific case of anisotropic superconductivity. The extension of the BCS theory for two or more superconducting bands is due to Suhl *et al.* [53] and independently to Moskalenko [54]. Suhl *et al.* elaborated a model considering overlapping of s and d bands but their results can be generalized to any type of bands.

2.3.1 BSC multi-band model

In the two band case the electronic terms of the Hamiltonian can be written as

$$\begin{aligned} H = & \sum_{\mathbf{k}\sigma} \epsilon_{1,\mathbf{k}} c^{+}_{1,\mathbf{k}\sigma} c_{1,\mathbf{k}\sigma} + \sum_{\mathbf{k}\sigma} \epsilon_{2,\mathbf{k}} c^{+}_{2,\mathbf{k}\sigma} c_{2,\mathbf{k}\sigma} + \\ & - \sum_{\mathbf{k}\mathbf{k}'} V_{11} c^{+}_{1,\mathbf{k}\uparrow} c^{+}_{\mathbf{1},-\mathbf{k}\downarrow} c_{\mathbf{1},-\mathbf{k}'\downarrow} c_{1,\mathbf{k}'\uparrow} - \sum_{\mathbf{k}\mathbf{k}'} V_{22} c^{+}_{2,\mathbf{k}\uparrow} c^{+}_{\mathbf{2},-\mathbf{k}\downarrow} c_{\mathbf{2},-\mathbf{k}'\downarrow} c_{2,\mathbf{k}'\uparrow} \\ & - \sum_{\mathbf{k}\mathbf{k}'} V_{12} c^{+}_{1,\mathbf{k}\uparrow} c^{+}_{\mathbf{1},-\mathbf{k}\downarrow} c_{\mathbf{2},-\mathbf{k}'\downarrow} c_{2,\mathbf{k}'\uparrow} + c^{+}_{\mathbf{2},-\mathbf{k}\uparrow} c^{+}_{\mathbf{2},-\mathbf{k}\downarrow} c_{\mathbf{1},-\mathbf{k}'\downarrow} c_{\mathbf{1},-\mathbf{k}'\uparrow} \end{aligned} \tag{2.16}$$

where the bands are labelled 1 and 2 and $\epsilon_{i,\mathbf{k}}$ is the kinetic energy for band i. V_{ij} is the averaged pairing potential which results from phonon emission and absorption by an $i-j$ process. Different bands can have different pairing potentials, that are assumed to be constant on each sheet of the FS. The first and the third terms concern the superconductivity in band 1 while the second and the fourth in band 2. Without the fifth term the two bands would have a different T_c. The pairing potential V_{12} is associated to the *interband coupling* and acts in the same way as V_{11} and V_{22} which are associated to the *intraband coupling* between two bands.
From Eq. 2.16 it is possible to obtain the equations for the two energy gaps, which are

assumed to be constant on each sheet of the FS [55]:

$$\begin{aligned}\Delta_1 = \Lambda_{11}\Delta_1 \int_0^{k_B\theta_D} d\epsilon \, \frac{\tanh(\sqrt{\epsilon^2+\Delta_1^2}/2k_BT)}{\sqrt{\epsilon^2+\Delta_1^2}} \\ + \Lambda_{12}\Delta_2 \int_0^{k_B\theta_D} d\epsilon \, \frac{\tanh(\sqrt{\epsilon^2+\Delta_2^2}/2k_BT)}{\sqrt{\epsilon^2+\Delta_2^2}}\end{aligned} \tag{2.17}$$

$$\begin{aligned}\Delta_2 = \Lambda_{22}\Delta_2 \int_0^{k_B\theta_D} d\epsilon \, \frac{\tanh(\sqrt{\epsilon^2+\Delta_2^2}/2k_BT)}{\sqrt{\epsilon^2+\Delta_2^2}} \\ + \Lambda_{21}\Delta_1 \int_0^{k_B\theta_D} d\epsilon \, \frac{\tanh(\sqrt{\epsilon^2+\Delta_1^2}/2k_BT)}{\sqrt{\epsilon^2+\Delta_1^2}}\end{aligned} \tag{2.18}$$

assuming that the two bands have the same Debye temperature.
In Fig. 2.5 the temperature dependence of the normalized gaps (numerical solutions obtained from Eq. 2.17 and 2.18) is shown: (i) bands completely decoupled (V_{ij}, solid lines): the critical temperature of the bands depend on the relevant intraband coupling; (ii) weakly coupled bands (dashed lines). While Δ_1 follows the same standard BCS temperature dependence (but with $2\Delta/k_BT_c > 3.53$), Δ_2 features a high-temperature tail and closes at the same T_c as Δ_1, and (iii) strongly coupled bands (dashed-dotted lines). The small gap still deviates from a BCS-like behavior but smoothly decreases on heating, to finally close rather quickly at T_c. The gap ratios $2\Delta/k_BT_c$ for the two gaps are greater and smaller than the single-band BCS value of 3.53, respectively.
In other words, considering Eq. 2.16 when $V_{12} = 0$ there are two distinct transition temperatures, one for each gap. When $V_{12} \ll \sqrt{V_{11}V_{22}}$ the lower transition temperature disappears as shown in Fig. 2.5. The band with higher T_c also called "stronger" and the other is called "weaker". The interband coupling is the pairing interaction that leads to the formation of pairs [53].
The critical temperature for a weak-coupling superconductors can be also calculated within this formula (analytical solution from Eq. 2.17 and 2.18):

$$k_BT_c = 1.14k_B\theta_D \exp\left(-1/\lambda_{eff}\right) \tag{2.19}$$

where λ_{eff} in the effective coupling constant and it defined as the maximum eigenvalue λ_{max} of the matrix $\Lambda ij = V_{ij}N_j$ with the density of states N_j at the Fermi energy in the jth band. The conventional isotropic λ can be defined in terms of Λ_{ij} as

$$\lambda = \sum_{ij} \Lambda_{ij}N_i/N = \sum_i \lambda_{ij}N_i/N \tag{2.20}$$

where $\lambda_i = \sum_j \Lambda_{ij}$ and $N = \sum_i N_i$.

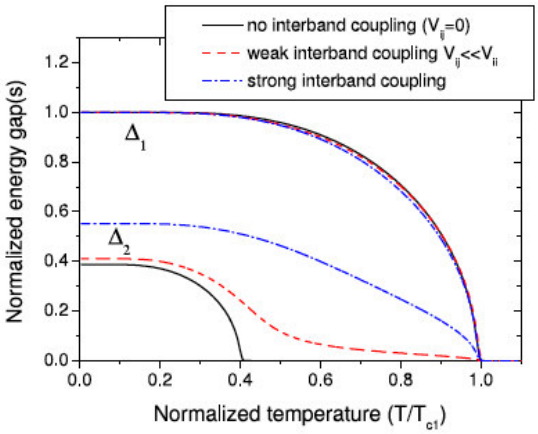

Figure 2.5: Temperature dependence of the gaps Δ_1 and Δ_2 in a two-band BCS model, calculated in the cases of: no interband coupling (solid lines); weak interband coupling (dotted lines) and strong interband coupling (dashed-dotted lines). The intraband coupling constants are arbitrary [2].

The generalization of the Eq. 2.17 and 2.18 for M-bands superconductors is here reported:

$$\Delta_i = \sum_{ij=1}^{M} \Lambda_{ij}\Delta_j \int_0^{k_B\theta_{D_{ij}}} d\epsilon \frac{\tanh(\sqrt{\epsilon^2+\Delta_j^2}/2k_BT)}{\sqrt{\epsilon^2+\Delta_j^2}} \tag{2.21}$$

Multi-band superconductivity became really important in 2001 when MgB_2 was found to be a two-band superconductor. Indeed it represents a particular case where one "leading" band enjoys the strongest pairing interactions, while the interband-pairing interaction, as well as the intraband pairing in the other band, is weak [56, 57]. However Fe-based SCs represent another limiting case: the pairing interaction is predominantly interband, while the intraband pairing in both bands is weak. It was shown by Dolgov O.V. et al. [58] that the two-band superconductivity is qualitatively incorrectly described by the BCS formalism even for the weak-coupling limit. In a only interband superconductive system the weak-coupling limits of the Eliashberg and the BCS theories are not equivalent. It was found by Ummarino G.A. [59] that a multi-band Eliashberg model with a very small number of free parameters can account surprisingly well for the phenomenology of Fe-based superconductors.

2.3.2 Multi-band Eliashberg theory

The interpretation of the data within Eliashberg theory turned out to be really useful when information on the nature and the energetic scale of the electron-boson coupling function are not reliable. The proximity between superconducting state and static magnetic order in the phase diagram of Fe-based SCs suggests the pairing mechanism mediated by spin fluctuations (SFs) [60], also supported by experimental studies of the antiferromagnetic spin dynamics [61]. In the strong-coupling regime information on the spectrum of the mediating boson can be obtained from PCARS [62, 63, 64] which allows detecting the

coupling between electrons and FSs. In the Eliashberg theory [49] the order parameter is a complex function of energy

$$\Delta(E) = Re[\Delta(E)] + iIm[\Delta(E)] \tag{2.22}$$

where the imaginary part accounts for the finite lifetime of Cooper pairs and retains information about the electron-boson spectrum (or Eliashberg function) $\alpha^2F(\omega)$. Also the superconducting DOS $N(E) = Re[E/(E^2 - \Delta^2)]$ gives evidence of the electron-boson interaction [65].
The values of the gaps and the critical temperature of Fe-based SCs were already reproduced within Eliashberg theory in $Ba(Fe_{0.92}Co_{0.08})_2As_2$ single crystals [66], on LiFeAs [67], on $SmFeAsO_{0.8}F_{0.2}$ [68], on $LaFeAsO_{0.9}F_{0.1}$ and on $Ba_{0.6}K_{0.4}Fe_2As_2$ [69]. Indeed, even if in multiband superconductors is not possible to extract the $\alpha^2F(\omega)$ as in single-band superconductors [64], it is possible to try to reproduce the observed features in the conductance curve and its second derivative by choosing different electron-boson spectra. Also in this work PCARS experimental results were analysed within the Eliashberg theory. The first assumption of the model is that the electronic structure of Fe-based SCs can be approximately described by one hole band (indicated in the following as band 1) and two electron bands (2 and 3) [59, 66]. The gap symmetry is assumed to be $s\pm$ [12] the sign of one gap for example Δ_1 is opposite to that of the other for example Δ_2 and Δ_3.
Although many spectroscopic techniques, provides at most two gap amplitudes for pnictides and chalcogenides and does not allow associating them to a particular FS sheet, the use of (at least) three effective bands and thus three gaps is necessary for the Eliashberg model to be able to reproduce the experimental results.
To obtain the gaps and the critical temperature within the s± wave three-band Eliashberg model one has to solve six coupled equations for the gaps $\Delta_i(i\omega_n)$ and the renormalization functions $Z_i(i\omega_n)$, where i is a band index ($i = 1...3$).
The equations are:

$$\begin{aligned}\omega_n Z_i(i\omega_n) = \omega_n + \pi T \sum_{m,j} \Lambda^Z_{ij}(i\omega_n, i\omega_m) N^Z_j(i\omega_m) + \\ + \sum_j \left[\Gamma^N_{\mathrm{ij}} + \Gamma^M_{\mathrm{ij}}\right] N^Z_j(i\omega_n)\end{aligned} \tag{2.23}$$

$$\begin{aligned}Z_i(i\omega_n)\Delta_i(i\omega_n) = \pi T \sum_{m,j} \left[\Lambda^\Delta_{ij}(i\omega_n, i\omega_m) - \mu^*_{ij}(\omega_c)\right] \times \\ \times \Theta(\omega_c - |\omega_m|) N^\Delta_j(i\omega_m) + \sum_j [\Gamma^N_{\mathrm{ij}} + \Gamma^M_{\mathrm{ij}}] N^\Delta_j(i\omega_n)\end{aligned} \tag{2.24}$$

where Γ^N_{ij} and Γ^M_{ij} are the non magnetic and magnetic impurity scattering rates, $\Lambda^Z_{ij}(i\omega_n, i\omega_m) = \Lambda^{ph}_{ij}(i\omega_n, i\omega_m) + \Lambda^{sf}_{ij}(i\omega_n, i\omega_m)$, $\Lambda^\Delta_{ij}(i\omega_n, i\omega_m) = \Lambda^{ph}_{ij}(i\omega_n, i\omega_m) - \Lambda^{sf}_{ij}(i\omega_n, i\omega_m)$.
Θ is the Heaviside function and ω_c is a cutoff energy.
In particular, $\Lambda^{ph,sf}_{ij}(i\omega_n, i\omega_m) = 2\int_0^{+\infty} d\Omega\Omega\alpha^2_{ij}F^{ph,sf}(\Omega)/[(\omega_n - \omega_m)^2 + \Omega^2]$.

$\mu^*_{ij}(\omega_c)$ are the elements of the 3×3 Coulomb pseudopotential matrix.
Finally, $N_j^{\Delta}(i\omega_m) = \Delta_j(i\omega_m)/\sqrt{\omega_m^2 + \Delta_j^2(i\omega_m)}$ and $N_j^{Z}(i\omega_m) = \omega_m/\sqrt{\omega_m^2 + \Delta_j^2(i\omega_m)}$.
The electron-boson coupling constants are defined as $\lambda_{ij}^{ph,sf} = 2\int_0^{+\infty} d\Omega \frac{\alpha^2_{ij}F^{ph,sf}(\Omega)}{\Omega}$. Their solution requires a large number of input parameters (18 functions and 9 constants); however, some of these parameters are correlated, some can be extracted from experiments and some can be fixed by suitable approximations. For example, the coupling constant matrix λ_{ij} can be greatly simplified. In general, one should consider that each matrix element has a contribution from phonons and one from antiferromagnetic (AFM) spin fluctuations (SF), i.e. $\lambda_{ij} = \lambda_{ij}^{ph} + \lambda_{ij}^{sf}$. However, the coupling between the two electron bands is small, and we thus take $\lambda_{23} = \lambda_{32} = 0$; the total electron-phonon coupling in pnictides is generally small [70] and phonons mainly provide intraband coupling, so that it was assumed for Ba122 and Fe(Te,Se) compounds $\lambda_{ij}^{ph} = 0$; spin fluctuations mainly provide interband coupling between the two quasi-nested FS sheets [28], and thus it was assumed $\lambda_{ii}^{sf} = 0$.
Finally, the electron-boson coupling-constant matrix λ_{ij} takes the following form [12, 59, 66]:

$$\lambda_{ij} = \begin{pmatrix} \lambda_{11}^{ph} & \lambda_{12}^{sf} & \lambda_{13}^{sf} \\ \lambda_{21}^{sf} & \lambda_{22}^{ph} & 0 \\ \lambda_{31}^{sf} & 0 & \lambda_{33}^{ph} \end{pmatrix} \tag{2.25}$$

where $\lambda_{21}^{sf} = \lambda_{12}^{sf}\nu_{12}$ and $\lambda_{31}^{sf} = \lambda_{13}^{sf}\nu_{13}$, with $\nu_{ij} = N_i(0)/N_j(0)$ and $N_i(0)$ is the normal density of states at the Fermi level for the i-th band. Another fundamental ingredient is the electron-boson spectral function $\alpha^2F(\Omega)$ of the boson responsible for the pairing. The shape of the electron-phonon spectral function is taken from literature [71] and we assume $\alpha^2_{11}F^{ph}(\Omega) = \alpha^2_{22}F^{ph}(\Omega) = \alpha^2_{33}F^{ph}(\Omega)$ with $\lambda_{ii}^{ph} = 0.2$ [72].
As for spin fluctuations, we assume their spectrum to have a Lorentzian shape [59, 73, 74, 75]:

$$\alpha^2_{ij}F^{sf}(\Omega) = C_{ij}\big\{L(\Omega + \Omega_{ij}, Y_{ij}) - L(\Omega - \Omega_{ij}, Y_{ij})\big\} \tag{2.26}$$

where $L(\Omega \pm \Omega_{ij}, Y_{ij}) = \frac{1}{(\Omega \pm \Omega_{ij})^2 + Y_{ij}^2}$ and C_{ij} are normalization constants, necessary to obtain the proper values of λ_{ij} while Ω_{ij} and Y_{ij} are the peak energies and half-widths of the Lorentzian functions, respectively [59].
In all the calculations we set $\Omega_{ij} = \Omega_0^{sf}$ and $Y_{ij} = Y_{ij}^{sf} = \Omega_0^{sf}/2$ [76].
Here, Ω_0^{sf} is the characteristic energy of the AFM SF, assumed to be equal to the spin-resonance energy. Its value is determined according to the empirical relation $\Omega_0^{sf} = 4.65 k_B T_c$ (proposed in ref. [5]). Bandstructure calculations provide information about the factors ν_{ij} that enter the definition of λ_{ij}. As a first approximation, these values have been used here for all Co contents. Moreover, based on the fact that the Coulomb pseudopotential is probably small in these compounds [77] we assume all the elements of the pseudopotential matrix to be identically zero ($\mu^*_{ii} = \mu^*_{ij} = 0$); finally, we neglect the effect of disorder, owing to the high quality of the films.
Finally, only two free parameters remain, i.e. the coupling constants λ_{12}^{sf} and λ_{13}^{sf}. These parameters can be tuned in such a way to reproduce the PCARS experimental values (see

section 2.4) of the small gap Δ_S and of the critical temperature, which are the best-defined experimental data.
Experimental results obtained (by means of PCARS measurements) on $Ba(Fe_{1-x}Co_x)_2$ and on $Fe(Te_{1-x}Se_x)$ thin films were analysed by means of the three-band Eliashberg calculations are discussed in Sections 4.3.3 and 5.3.3.

2.4 Andreev reflection

In this section the Andreev reflection is introduced from the theoretical point of view. This is one of the most relevant phenomenon observed in superconductors and was also a strong confirmation of both the existence of the existence of the Cooper pairs as well as the BCS energy gap. The experimental details the point-contact Andreev reflection spectroscopy (PCARS), the main experimental technique used in this research, will be described in the follow chapter.

2.4.1 Andreev reflection

If a normal metal (N) is brought in direct ballistic contact (i.e. the size of the contact is smaller than the mean free path of electrons in the bulk material) with a superconductor (S), with no potential barrier between them and a voltage $V < \Delta/e$, Δ being the energy gap in the S side, the whole voltage drop occurs at the interface. An electron coming from the N side will not be able to propagate through the interface because only Cooper pairs exist in this energy range in S. But if a hole is reflected and two electrons are transmitted in S as a Cooper pair (see Fig. 2.6) the total charge and momentum are conserved. This phenomenon is called Andreev reflection [78] and can be theoretically described by solving the Bogoliubov-de Gennes equations [79] at an N/S interface.

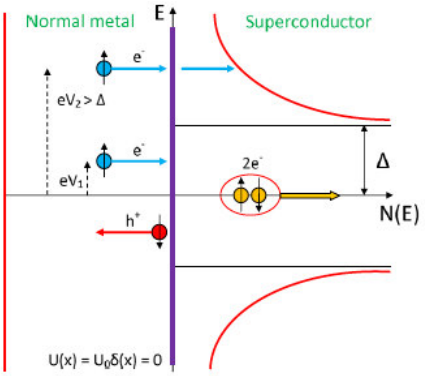

Figure 2.6: Electrical transport at an barrierless N/S interface at $T = 0$. Incoming electrons with $eV \ll \Delta$ are reflected as holes and, for each electron, a Cooper pair is transmitted (Andreev reflection). Electrons approaching the interface with $eV \gg \Delta$ are normally transmitted as electron-like quasiparticles adapted from [2]

Since a doubling of the conductance occurs in correspondence of the energy gap, Andreev

reflection can be a good tool to determine the value of the energy gap. If the applied voltage is much greater than the gap ($eV \gg \Delta$), all the electrons whose energy is lower than the gap still undergo Andreev reflection giving a constant current contribution, while the all the electrons whose energy is higher than the gap are transmitted across the interface giving a voltage-dependent current contribution. The total current for $eV \gg \Delta$ is:

$$I \propto ev_F(eV - \Delta) + 3ev_F \approx \frac{V}{R_S} + \frac{\Delta}{eR_S} \tag{2.27}$$

The second term on the right-hand side of Eq.2.27 is called "excess-current" and is the hallmark of the superconducting state even at the energies much higher than the gap. This result is exact only if the gap rises from zero up to the bulk value over a distance larger than the superconducting coherence length ξ. If the gap is instead modeled as a sharp barrier at the interface an additional term equal to $\Delta/3eR_S$ must be included. The conductance of the junction turns out to be doubled for $eV \ll \Delta$ when Andreev reflection occurs. This suggests a way to determine the energy gap in the S side by point-contact spectroscopy. This technique is often referred to as point-contact Andreev-reflection spectroscopy (PCARS). The details of this experimental technique will be described in the following chapter.

2.4.2 The BTK model

A complete theoretical discussion of the Andreev Reflection (AR) was given in 1982 by Blonder, Thinkam and Klapwijk [80]. In their model, called the BTK model, the differential conductance (dI/dV) was calculated at $T = 0$ (see Fig. 2.7), including the effect of a non-ideal interface (oxide layer and mismatch of Fermi velocities between the two materials) [2].
In the simplified 1D-BTK model, the momenta of the electrons coming trough the interface are considered to be normal to the interface between the normal metal and the superconductor. In this case, it is supposed to be in the yz plane.The barrier, represented by a repulsive potential $U_0\delta(x)$ located at the interface, is introduced into the calculations with the dimensionless parameter $Z = U_0/\hbar v_F$.
According to this model, the coming from the normal metal can be involved in four different processes. The specific probability associated to each process (their sum must be 1) is here reported:

- A is the probability of AR. The probability decreases with increasing Z for eV$< \Delta$ and is always small for eV$> \Delta$;
- B probability of normal specular reflection. This probability increases with Z, i.e. on decreasing the barrier transparency;
- C probability of transmission in S as an electron-like quasiparticle (ELQ). The probability decreases if Z increases but it is always zero for eV$< \Delta$;
- D probability of transmission with FS crossing (i.e. as a hole-like quasiparticle, HLQ). The probability is small for eV$> \Delta$ and always zero for eV$< \Delta$.

Therefore the expression of the total current across the junction can be written as:

$$I_{NS} = I_0 \int_{\infty}^{\infty} [f(E - eV) - f(E)][1 + A(E) - B(E)]dE \tag{2.28}$$

where $f(E)$ is the Fermi distribution function, $A(E)$ and $B(E)$ are the coefficients giving the probability of Andreev and ordinary reflection respectively, and I_0 is a constant dependent on the area of the junction, on the density of states and on the Fermi velocity, and $[1 + A(E) - B(E)]$ is the transmission probability often called $\sigma(E)$.
The first derivative of the current with respect of the bias voltage dI_{NN}/dV provide the conductance as is shown in Fig. 2.7 where the I-V characteristic of an ideal, barrierless N-S junction ($Z = 0$) at $T = 0$, in the hypothesis that there is no AR for $eV \gg \Delta$ (blue line) compared to the I-V characteristic of a N-N junction having the same resistance (black dotted line). The normalized conductance curve, i.e. divided by the normal conductance dI/dV_{NN}, of the same junction calculated by using the BTK model is shown in the lower panel. The normalized conductance G is the outcome of the point-contact AR measurements.

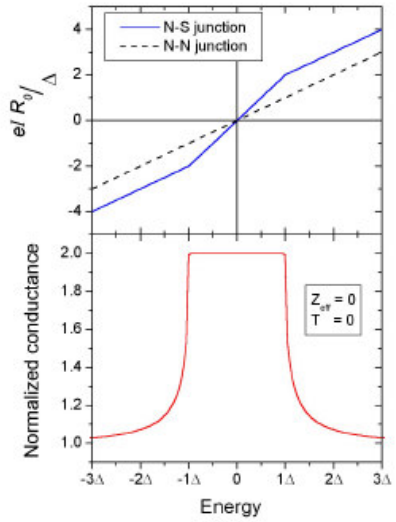

Figure 2.7: The I-V characteristic (upper panel) of an ideal, barrierless N-S junction at $T = 0$, in the hypothesis that there is no Andreev reflection for $eV \gg \Delta$ (blue line) compared to the I-V characteristic of a N-N junction having the same resistance (black dotted line) and the normalized conductance curve (lower panel) of the same junction calculated by using the BTK model adapted from [2].

Kashiwaya S. et al. [81] developed an approach to AR in which the normalized conductance $G = (dI)_{NS}/(dI/dV)_{NN}$ at $T = 0$ can be written as a function of $\gamma(E)$ where:

$$\gamma(E) = \sqrt{\frac{E - \sqrt{E^2 - \Delta^2}}{E + \sqrt{E^2 - \Delta^2}}} = \frac{E - \sqrt{E^2 - \Delta^2}}{\Delta} \tag{2.29}$$

In order to understand better the BTK model, which will be used in the 2D generalization to analyse the measurements discussed in the follow chapters, the BTK conductance σ_E

at $T = 0$ is here reported. By using, γ, previous defined, and the transparency τ_N of the barrier in the BTK approximation of current injection totally perpendicular to the N/S interface identified as:

$$\tau_N = \frac{1}{1 + Z^2} \tag{2.30}$$

it is possible to calculate the BTK conductance at $T = 0$

$$\sigma(E) = \tau_N \frac{1 + \tau_N|\gamma(E)|^2 + (\tau_N - 1)|\gamma(E)^2|^2}{|1 + (\tau_N - 1)\gamma(E)^2|^2}. \tag{2.31}$$

The normalized conductance curves of an N/S interface at $T = 0$ calculated within the BTK model as a function of the barrier parameter Z, from pure Andreev regime ($Z = 0$) to pure tunneling ($Z = 10$) regimes is shown in Fig. 2.8. In between these two possibilities, when $Z > 0$ the model predicts that two peaks appear at $|eV| \approx \Delta$ with their amplitude increasing on increasing Z and the zero-bias conductance peak (ZBP) is depressed.

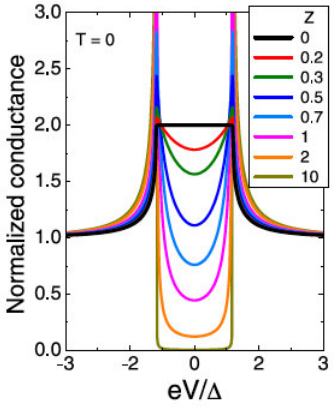

Figure 2.8: Effect of barrier parameter Z, from pure Andreev ($Z = 0$) to pure tunneling ($Z = 10$) regimes a normalized conductance curves of an N/S interface at $T = 0$ calculated within the BTK model adapted from [2].

Despite the strong simplifications, the BTK model turned to be a really powerful tool for experimental data analysis because it can reproduce by changing the Z parameter the different possible experimental situations. In the next section the extension of the formalism used in this work will be discussed.
The case of a real junction, i.e. presence of potential barrier at the interface or mismatch in the Fermi velocities in the two materials, the phenomenological parameter Z_{eff} was introduced in the BTK model [82] the effective barrier parameter defined as:

$$Z_{eff} = \sqrt{Z^2 + \frac{(1 - r)^2}{4r}} \tag{2.32}$$

where $r = v_S/v_N$ is the Fermi velocity ratio, v_S and v_N are the Fermi velocities in the superconductor and in the normal metal. The normal-state resistance at high voltage is given by $R_N = R_S(1 + Z_{eff}^2)$ where R_S is the Sharvin resistance [82], i.e. the resistance

of the contact when the mean free path of the superconductor is smaller then the contact size (see 3.2.1). Increasing Z_{eff}, a pure tunnel regime is achieved, i.e. the I-V curve has more and more a tunnel-like appearance.
Actually in most cases the BTK model predicts much sharper gap features than those observed in the low-temperature conductance curves. This means that the AR structures in the experimental spectra are not only depressed in amplitude but also spread in energy. This effect is due to both the reduction of the quasiparticle lifetime [83] and the inelastic scattering centers at the N/S interface [84]. In order to take this effect into account, a broadening parameter Γ [84, 85] in the form of imaginary part of the energy ($E \rightarrow E + i\Gamma$) was introduced which modify $\sigma(E)$ [83, 84].

The 2D-BTK model

The generalization of the 1D-BTK model allows describing the more realistic situation in which the charge carriers approach the interface from any direction. The AR theory set the two conditions that the total charge and the component of the **k** vector parallel to the interface are conserved in all processes.
In the left panel of Fig. 2.9 the schematic view of a ballistic AR contact shows the reflected hole coming back in N with k opposite to that of the incident electron. It traces back its trajectory until the first scattering event in N occurs. In the S side a Cooper pair propagates essentially in the same direction as the incident electron.

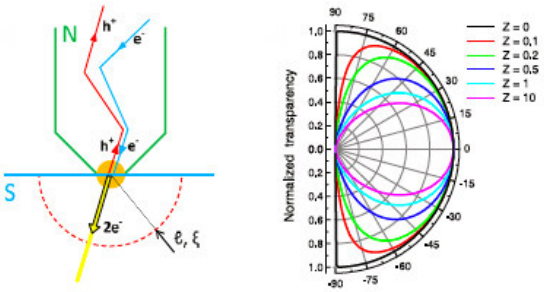

Figure 2.9: Sketch of AR phenomenon (left panel) and a polar plot of the normalized transparency of an NS junction (right panel) as a function of the angle of injection of the current for different values of the Z adapted from [2].

Therefore considering the angle θ_N between the direction of the direction of the incident electron and the normal to the interface and the conservation of the transverse momenta, the transparency τ_N can be written as:

$$\tau_N(\theta_N) = \frac{\cos(\theta_N)^2}{\cos(\theta_N)^2 + Z^2} \tag{2.33}$$

In the right panel of Fig. 2.9 the normalized transparency $\tau_N(\theta_N)/\tau_N(0)$ is shown for different value of the parameter Z. For $Z = 0$ is described the case in which the quasiparticles are transmitted with the same probability in the half space $-\pi/2 \leq \theta_N \leq \pi/2$, while when Z decreases is described the situation in which the transmission becomes progressively

weaker and more directional around the perpendicular to the interface.
By introducing the expression (2.33) in the Eq. (2.31), and integrating over the whole half-plane, the normalized conductance at $T = 0$ of the so called "2D-BTK" model [81] is obtained. Therefore the normalized conductance for a system with isotropic gap and spherical FS, i.e. rotational symmetry, can be written as

$$G_{2D}(E) = \frac{\int_{-\pi/2}^{+\pi/2} \sigma(E, \theta_N) \cos\theta_N d\theta_N}{\int_{-\pi/2}^{+\pi/2} \tau(\theta_N) \cos\theta_N d\theta_N}. \tag{2.34}$$

The temperature dependence of the G_{2D} can be calculated by a convolution with the Fermi function [2, 81].

2.4.3 The 3D-BTK model

The 2D-BTK model can properly describe the isotropic superconductors or the layered ones, like cuprates, provided that the current is injected along the ab plane but it can not express the c-axis conductance in layered superconductors, or more generally, the conductance in multiband superconductors with complex shapes of the FS sheets. Therefore, the generalization on the 2D-BTK model known as "3D-BTK" model was proposed [36, 68].
In this model the general expression of the normalized conductance of a point-contact NS junction at $T = 0$ is given by:

$$\langle G(E)\rangle_{l||\mathbf{n}} = \frac{\sum_i \langle \sigma_{i\mathbf{k},n}(E)\tau_{i\mathbf{k},n}\frac{v_{i\mathbf{k},n}}{v_{i\mathbf{k}}}\rangle_{FS_i}}{\sum_i \langle \tau_{i\mathbf{k},n}\frac{v_{i\mathbf{k},n}}{v_{i\mathbf{k}}}\rangle_{FS_i}} \tag{2.35}$$

where i is the band index, the brackets indicate the average over the $i-$th FS sheet, the subscript n refers to the direction of current injection and $v_{i\mathbf{k},n} = \mathbf{v}_{i\mathbf{k}} \cdot \mathbf{n}$ is the projection of the Fermi velocity in the $i-$th band (that is thus perpendicular to the ith FS sheet) along the direction of the unit vector $\mathbf{n}$ parallel to the injected current.
The normal-state barrier transparency is defined as

$$\tau_{i\mathbf{k},n} = \frac{4 v_{i\mathbf{k},n} v_{N,n}}{(v_{i\mathbf{k},n} + v_{N,n})^2 + 4Z^2 v_N^2} \tag{2.36}$$

where $\mathbf{v}_{N,n} = \mathbf{v}_N \cdot \mathbf{n}$ and $\mathbf{v}_N$ is the Fermi velocity in the normal material supposed constant in magnitude (spherical FS). The quantity $\sigma_{i\mathbf{k},n}(E)$ is the superconducting-state relative barrier transparency expressed by the following equation:

$$\sigma_{i\mathbf{k},n}(E) = \frac{1 + \tau_{i\mathbf{k},n}|\gamma_+(E)|^2 + (\tau_{i\mathbf{k},n} - 1)|\gamma_+(E)\gamma_-|^2}{|1 + (\tau_{i\mathbf{k},n} - 1)\gamma_+(E)\gamma_-(E)\exp(i\varphi_d)|^2} \tag{2.37}$$

where

$$\gamma_\pm(E) = \frac{(E + i\Gamma) - \sqrt{(E + i\Gamma)^2 - |\Delta_{i\mathbf{k}}^\pm|^2}}{|\Delta_{i\mathbf{k}}^\pm|} \tag{2.38}$$

and

$$\varphi_d = -i \ln \left[\frac{\Delta^+_{i\mathbf{k}}/|\Delta^+_{i\mathbf{k}}|}{\Delta^-_{i\mathbf{k}}/|\Delta^-_{i\mathbf{k}}|} \right] \tag{2.39}$$

is the phase difference seen by the holelike quasiparticles (HLQ) with respect to the electronlike ones (ELQ), being $\Delta^+_{i\mathbf{k}}$ and $\Delta^-_{i\mathbf{k}}$ the different (in phase and/or in magnitude) $\mathbf{k}$-dependent order parameters of the $i-$th band felt by the ELQ and by the HLQ, respectively. The complete knowledge of the $\mathbf{k}$-dependence of the FS sheets (i.e. their geometry in the reciprocal space) and of the order parameters (i.e. their symmetry), under some simplifying conditions, can give all the ingredients required to calculate the normalized conductance. Indeed the points at the Fermi energy can be supposed to be close to the top or the bottom of parabolic-like bands (where the effective mass approximation holds). Then the Fermi velocity at any $\mathbf{k}$ point can be uniquely expressed as a function of the constant effective mass and of the FS shape and dimensions [36, 68].
In case of spherical FS and isotropic order parameters, when the barrier at the NS interface has a negligible transparency (i.e. $Z \to \infty$ that corresponds to a tunnel junction), Eq. 2.35 reduces to a weighted average of the relative superconducting state transparencies of the bands $\sigma_i(E)$ where the weights can be expressed as $\langle N_{i\mathbf{k}} v^2_{i\mathbf{k},n} \rangle_{FS_i}$, $N_{i\mathbf{k}}$ being the normal density of states (DOS) of the $i-$th band at the Fermi energy and at the wave vector $\mathbf{k}$ in the superconductor. When instead the barrier at the NS interface is completely transparent (i.e. $Z = 0$), the total normalized conductance is again a weighted average $\sigma_i(E)$ but the weights can be now expressed as $\langle N_{i\mathbf{k}} v_{i\mathbf{k},n} \rangle_{FS_i}$ [68, 86]. Since the normal DOS is always proportional to the reciprocal of the Fermi velocity, it turns out that the previous average on the FS returns the area of the projection of the ith FS sheet on a plane perpendicular to $\mathbf{n}$. The implications of this result is that, in the case of ballistic point contacts on normal metals (NN$'$ junctions with $Z = 0$) the conductance is not expected to contain any information on an energy-dependent DOS.

2.4.4 The two-band BTK model

In the previous section, the standard one-band BTK model has been discussed. The multi-band structure of the Fe-based SCs calculated by DFT calculation and confirmed by experimental results [5] required the generalization to at least the two-band BTK model. Unfortunately a multi-band model (with more then two bands) would have too many free parameters and the fit procedure would become difficult in order to obtain reasonable results, in reasonable time. Moreover it is not trivial to measure more than two gaps by means of PCARS. Actually there were evidence of two gaps in PCARS measurements on these compounds in this work, as it will be shown in the following chapters. Therefore the two-band BTK model were used systematically in order to obtain the number and the values of the amplitude of energy gaps.
Brinkman et al. [87] proposed a theoretical model in order to explain multi-band superconductivity in tunneling from a normal metal (N) into MgB_2 in an extended BTK model within the the Eliashberg theory, taking into accounts strong coupling effects. They calculated the conductance curve for various transparency, considering the current injection

in the $a-b$ plane, in the $c-$axis direction and under arbitrary angle.
They grouped the four FS sheets in MgB_2 according to Liu et al. [88], describing an effective two-band model that is here adapted to Fe-based SCs systems.
Therefore in the two-band BTK model the normalized conductance G of the NS ballistic junction is a weighed sum of the conductance curves $G^{'}$ and $G^{''}$ for each band:

$$G \equiv \frac{(dI/dV)_{NS}}{(dI/dV)_{NN}} = \frac{(\omega_p^{''})^2 G^{''}(V) + (\omega_p^{'})^2 G^{'}(V)}{(\omega_p^{''})^2 + (\omega_p^{'})^2} \tag{2.40}$$

In this model, the dimensionless conductance $G^{''}(V)$ and $G^{'}(V)$ can be provided by the BTK model with the calculated values of the plasma frequencies $\omega_p^{'}$ and $\omega_p^{''}$ [87].
The Eq. 2.40 can be written as:

$$G = \omega^{''} G^{''} + (1 - \omega^{''}) G^{'} \tag{2.41}$$

where $\omega^{''} = {\omega_p^{'}}^2 / ({\omega_p^{''}}^2 + {\omega_p^{'}}^2)$ is the weight of the band-2 with respect to the total conductance and depends on the direction of the current injection.
$G^{'}$ and $G^{''}$ are expressed as in the standard BTK model and thus depend on the relevant amplitude of the two gaps ($\Delta^{'}$ and $\Delta^{''}$), on the effective barrier parameter ($Z^{'}$ and $Z^{''}$) and o the broadening parameter ($\Gamma^{'}$ and $\Gamma^{''}$). $Z^{'}$ and $Z^{''}$ depend on the potential barrier at the interface as well as the on the Fermi-velocity mismatch between two banks of the junction. Since v_F is different in the two bands, it is reasonable that $Z^{'} \neq Z^{''}$. Seven fitting parameter must be determined taking into accounts that $\omega^{''}$, $Z^{''}$ and $Z^{''}$ must be independent of the temperature of temperature and magnetic field. Furthermore, $\Gamma^{'}$ and $\Gamma^{''}$ should be lower than $\Delta^{'}$ and $\Delta^{''}$ respectively [89].
The uncertainty on $\Delta^{'}$ and $\Delta^{''}$ can be defined, for a given curve, as the maximum range of the gap values that allow a good fit of the curve, when the other parameters are changed too.

Chapter 3

Experimental techniques

This chapter is devoted to introduce the experimental details of the resistivity measurements and point-contact Andreev-reflection spectroscopy (PCARS). The superconducting properties in terms of critical temperature and energy gaps were systematically measured by using these complementary techniques in view of the possible use of epitaxial thin films for superconducting electronic application. In particular the results of local and non-local techniques were compared in order to check the homogeneity of the superconducting properties (critical temperature and gap amplitudes).

3.1 Resistivity measurements

The measurement of the electrical resistivity (and resistance) remains one of the standard way to measure the critical temperature of the superconductors on a millimeter scale. In this section the different techniques used in order to characterise the critical temperature of the samples analysed in this work are described.

3.1.1 The conventional technique

Conventional four-probe method allows measuring the resistivity of a certain bar shape material. Fig.3.1 shows the two current contacts on the short edge of the sample and two voltage contacts on the surface of the sample. The four terminal configuration ensures that the measured voltage does not include the voltage drop due to the current contacts. Indeed it eliminates lead resistance by forcing a current through the sample with one pair of leads while measuring the voltage drop with a second pair of leads [90].
The resistivity ρ is given by the formula:

$$\rho = \frac{V_{\mathrm{C}} - V_{\mathrm{D}}}{i} \frac{\mathcal{S}}{\ell_{\mathrm{CD}}} \tag{3.1}$$

where ℓ_{CD} is the distance between points C and D, and $\mathcal{S}$ is the cross-section of the sample in the direction of the current flow.
The average of the voltage values obtained by inversion of the current flow removes the

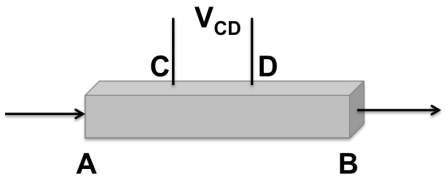

Figure 3.1: Conventional four-probe configuration for the measurements of the resistivity.
Current is injected through contact A and drained from contact B. The voltage drop is measured between contact C and D.

possible contribution of thermoelectric effects. Indeed the so called "Delta method" consists of measuring the voltage drop across the material with the current in one direction, then reversing the polarity of the current source and taking a second voltage measurement. Three voltage measurements are used to calculate each resistance value. In cases where hysteresis, non-linearity, or asymmetry is apparent, the current can be varied from one value to another of the same polarity. This will provide the average resistance between these two currents [90].
The strong limit to this technique is the mandatory request that the current density is equal on each point of the sample cross-section and that the equipotential surfaces must be planes parallel to the current electrode. Therefore this technique could be used only to measure on single crystals, that are usually considered the more homogeneous systems in term of electrical, transport and chemical properties.

3.1.2 The collinear technique

Another four-probe mode for resistance measurements involves bringing four equally spaced probes into contacts with the material under study. The probe array is usually place in the central part of the surface of the samples as shown in Fig 3.2. In the left panel the schematic our-point collinear probe resistivity method is reported while in the right panel an example of the measurements performed on Ba122 thin film is reported (AD current source - BC voltage). The "AB*CD" configuration were considered in order to check if after 4 days (putting keeping the sample in dry atmosphere) the transition curve shows signs of change aging effects (as it will be discussed in Section 4.2).
The two outer probes source current (injected) while the two inner probe measure the resulting voltage drop across the sample. The resistivity can be calculated by using the formula [90]:

$$\rho = \frac{\pi}{\ln 2} \frac{V}{I} t\, k \tag{3.2}$$

where ρ is the resistivity (Ωcm); V is the measured voltage (Volt); I is the source current (Ampere); t is the sample thickness (cm); k is the correction factor based on the ratio of the probe spacing to wafer diameter on the ratio of wafer thickness to probe spacing.

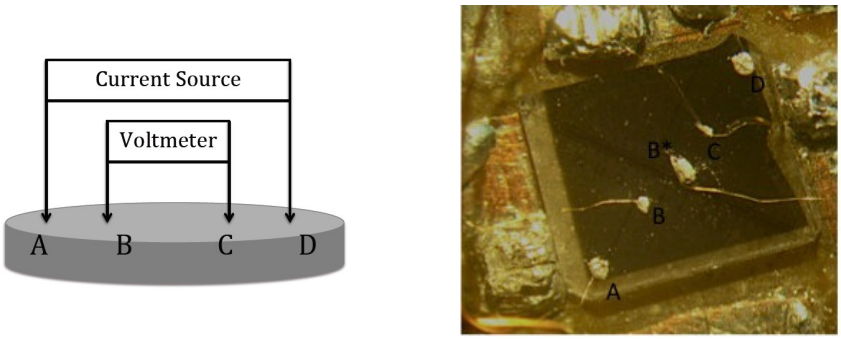

Figure 3.2: Schematic four-point collinear probe resistivity method (left panel) and four-point collinear probe resistivity measure on 8% Co-doped Ba122 thin film (right panel).

3.1.3 The Van der Pauw technique

An effective and widely used four-probe mode of determining the resistivity of materials in the form of thin films is the van der Pauw (vdP) technique introduced by Leo J. van der Pauw in 1958 [91, 92]. This technique was developed in order to measure the specific resistivity and the Hall effect of flat sample of arbitrary shape. The specific resistivity can be measured without knowing the current pattern by using this technique if the sample satisfies the following four requirements:

- The contacts are on the edge of the sample (on the corner for thin films in this work).
- The contacts are sufficiently small.
- The sample is homogenous in thickness.
- the sample does not have isolated holes.

Under this conditions, the resistance of the material is defined from the following equation of general validity:

$$\exp\left(-\pi\frac{R_{\mathrm{AB,CD}}\,d}{\rho}\right)+\exp\left(-\pi\frac{R_{\mathrm{BC,AD}}\,d}{\rho}\right)=1 \tag{3.3}$$

where

$$R_{\mathrm{AB,CD}}=\frac{V_{\mathrm{D}}-V_{\mathrm{C}}}{i_{\mathrm{AB}}} \tag{3.4}$$

and ρ is the resistance, d is the thickness of the sample, i_{AB} is the current entered the sample at the contact A and left it at the contact B, as shown in Fig.3.3.
Unfortunately, some of these requirements usually collide with experimental limits. The effects of those conditions missing were calculated in the case of different shape [93, 94].
In practical application, this method is used for measuring the resistivity on a flat sample

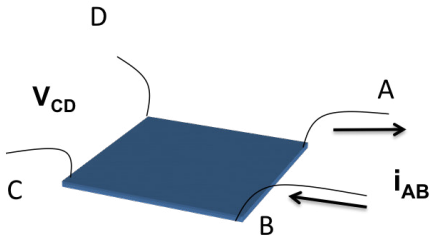

Figure 3.3: Example of contact disposition on the edge of a sample, in the van der Pauw configuration.

making four small contacts along its edge and measure the two resistance $R_{\mathrm{AB,CD}}$ and $R_{\mathrm{BC,DA}}$ and the thickness of the sample. From equation 3.3 is possible to write ρ as:

$$\rho = \frac{\pi d}{\ln 2} \frac{R_{\mathrm{AB,CD}} + R_{\mathrm{BC,DA}}}{2} f\left(\frac{R_{\mathrm{AB,CD}}}{R_{\mathrm{BC,DA}}}\right) \tag{3.5}$$

where f is called the "correction function". This is a function of the ratio of $R_{\mathrm{AB,CD}}$ and $R_{\mathrm{BC,DA}}$ only and can be analytically calculated from the equation:

$$\frac{R_{\mathrm{AB,CD}} - R_{\mathrm{BC,DA}}}{R_{\mathrm{AB,CD}} + R_{\mathrm{BC,DA}}} = \frac{f}{\ln 2} \mathrm{arccosh}\left(\frac{\exp \ln 2/f}{2}\right). \tag{3.6}$$

When the material under study is not highly homogeneous as requested from the vdP conditions, a modification of the method is advisable. This slight caution allows also testing the internal consistency of resistance data, i.e. this is a quantitative indirect measurements of the homogeneity of the sample, a important information to collect in the study of superconductors thin films. In this work many efforts were make in order to verify the homogeneity of the superconductive properties of these systems. As previous introduced the synthesis of high-quality films is the indispensable step towards the fabrication of Josephson junctions, the basic constituents of many electronic devices [31]. The systematic investigation of the resistivity can reveal many characteristics of the samples. Indeed if the sample is not homogeneous anomalous peak can appear in the resistance measurements performed on different side. An example of an anomalous peak next to the superconductive transition in the R vs T curve is reported in Fig. 3.4. The peak shown in Fig. 3.4, can be explained with the effect of the small stoichiometric inhomogeneities described by Mosqueira J. et al. [95]. In Fig. 3.5 the example of this peak is reported. The authors suggest to verify its by using magnetic field. But in this work a simplest way to verify the nature of the anomalous peak was adopted. Indeed the peak may be absent in some cases by just changing the location in the sample of the voltage and the current leads. Indeed by changing the current -voltage configuration of the measurements or the position of one of the spot on the surface the peak disappear.
In general voltage values measured with opposite direction of current flow, are not expected to be exactly equal in magnitude because of the possible presence of thermoelectric effects which can be eliminated by averaging the two values.

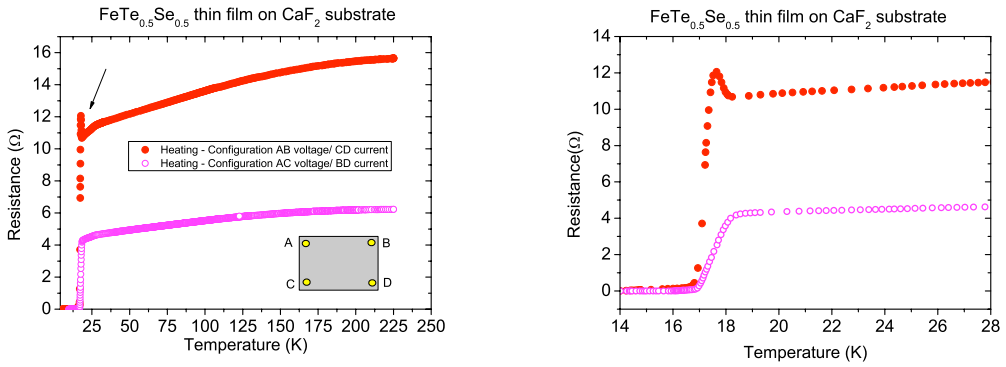

Figure 3.4: Resistance measurements of Fe(Te,Se) thin film. In the left panel two of the eight possible configurations in vdP method are reported. In the right panel the particular the resistance across the superconductive transition is reported where is clearly visible an anomalous peak in one of them.

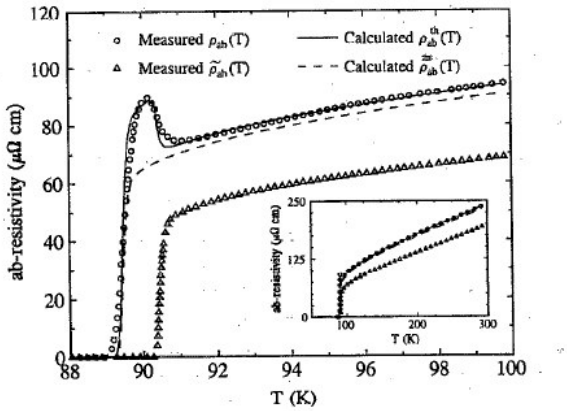

Figure 3.5: ab-plane resistivities vs temperature for the crystal YSll adapted by [95].

With respect to the collinear configuration, the vdP one allows probing a much larger region of the sample surface, and thus provides a well-representative measure of its average normal-state properties. If the measured resistivity is written as a weighted average over the entire sample surface, i.e. $< \rho >= \int \rho(x,y)g(x,y)\,dxdy$ where $g(x,y)$ is a position-dependent weighting function, the vdP configuration allows maximising the geometrical extension of the region (the so-called "sweet-spot" [96]) where the weighting function is maximum. In the case of a square sample with the contacts on its corners, as in our case, the van der Pauw resistance measurements probe an extended region of the film (of the order of some square millimetres) [96, 97].
In the case of a square sample, as the thin films analysed are generally in this work, the vdP configuration resistance measurements performed with contacts on the corners of the samples probe an extended region (of the order of some square millimetres) of the thin films (of the order of 1 cm x 1 cm). This technique is the more appropriate to measure

the resistance in thin films and this is way it was used in general for measurements on thin films.
The schematic vdP configuration and an example of the measurements performed on 8% Co-doped Ba122 thin film are reported in Fig. 3.6.

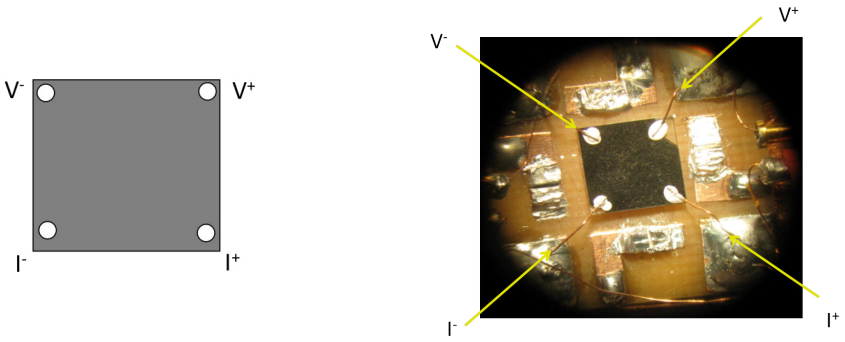

Figure 3.6: Van der Pauw configuration for resistivity measurements: schematic mounting (left side) and mounting on the 8% Co-doped Ba122 thin film (right side).

3.2 Point-contact Andreev-reflection spectroscopy (PCARS)

Point Contact Spectroscopy (PCS) was first developed by Yanson [62] to investigate the current-voltage characteristics of point contacts between metals in order to provide information about the scattering mechanisms of conduction electrons. Small microconstrictions between two metals that show nonlinearities in the I-V characteristic was found to be the hallmark of inelastic scattering of electrons by phonons. Such non-linearities are a measure of the inelastic scattering of conduction electrons and the applied voltage defines the energy scale of the interaction process. The second derivative of the voltage respect to the current shows structures which are proportional to the electron-phonon interaction function or Eliashberg function $\alpha^2 \mathcal{F}$.
The point-contact technique was later used to study all kinds of scattering of electrons by elementary excitation in metals [98, 99] and also to study superconducting materials [2]. When one of the sides of a point contact is a superconductor, quantum phenomena such as quasiparticle tunneling or Andreev reflection occur at the interface. In this configuration the I-V characteristic contains fundamental information on the excitation spectrum of the quasiparticles, i.e. on the superconducting energy gap and its properties in the direct and reciprocal space.
In this work, the point-contact technique is the main technique used to characterise and to study the fundamental properties of thin films. The study of the local critical temperature on millimeter scale as well as the doping and temperature dependence of the superconducting gap in different compounds will be described later on.

3.2.1 Point-contact in normal metal

Nowadays, the most common configuration used in PC is called "needle-anvil" in which the sample to be studied is one of the electrodes and the other is a metallic tip, electrochemically or mechanically sharpened, which is gently pressed against the sample surface (see Fig. 3.7 a). One of the advantages of this technique is that it is not destructive and several measurements can be carried out using the same sample. The main drawbacks of this configuration is the poor thermal and mechanical stability of the junction. Since 2001, the so-called "sotf" point-contact technique were adoped. In this configuration, the contact is made between the clean sample surface and a small drop (about 50 μm in diameter) of Ag paste or a small In flake. The Ag or In counter electrode is connected to current and voltage leads through a thin Au wire (10-25 μm in diameter) stretched over the sample (see Fig. 3.7 b). All the measurements discussed in this work were performed by using this latter configuration.

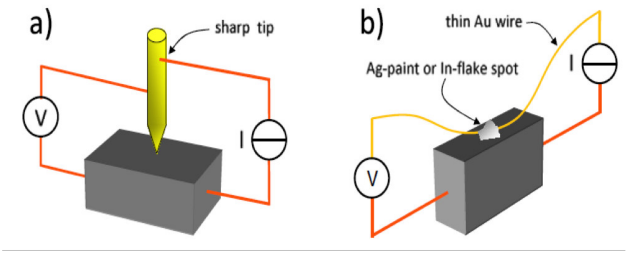

Figure 3.7: (a) Experimental arrangement for point-contact measurements with the typical needle-anvil technique. A metallic tip (Au, Pt-Ir, Pt, Ag) is gently pressed against the surface of the sample. (b) The "sotf" point-contact technique where a tiny spot of Ag paste (or a tiny flake of In) replaces the tip [2].

Some important spectroscopic criteria must be fulfilled in order to obtain energy-resolved information on the inelastic scattering of electrons with elementary excitation in metals. Considering the contact as a circular orifice in a non-conducting layer separating the electrodes, the Knudsen ratio $K = l/\mathrm{a}$ (where l is the mean free path in the metal and a is the contact radius) can be defined. The value of this fundamental parameter identifies thermal (or Maxwell), ballistic and diffusive spectroscopic regime. Reliable information can be obtained in the ballistic regime and also in the diffusive one.

Ballistic regime

In the ballistic regime the electron mean free path l is much larger than the contact radius a ($l \gg a$ or $K \gg 1$). In these conditions, almost all the voltage drop V between the electrodes is localized in the contact region. Electrons are accelerated when passing through the orifice and are then injected in the counterelectrode with a maximum excess energy eV (see Fig. 3.8 a).
The resistance of the contact

$$R_S = \frac{4\rho\ell}{3\pi a^2} \tag{3.7}$$

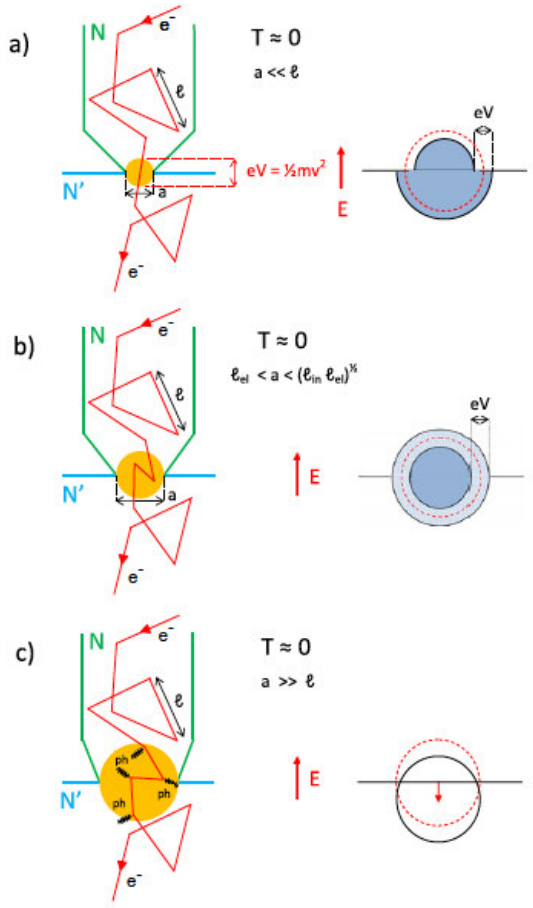

Figure 3.8: Schematic diagram of the contributions to the current in a point contact obtained by solving the Boltzmann equation. (a) Zeroth-order Sharvin current (no scattering). (b) Diffusive regime (only elastic scattering in the contact area). (c) Thermal regime with inelastic scattering in the contact region. The right sides of the figures show electron distribution functions at the center of the contact for the three main regimes: (a) ballistic regime. The FS is formed by two half-spheres with different radii, i.e. defined by the surfaces at energy E and E + eV. (b) Diffusive regime. The elastic scattering redistributes the electrons over the sphere but only in an energy shell with a width given by eV. (c) Thermal regime. The inelastic scattering reduces the shift in energy space as is usual for normal transport in a conductor [2].

was calculated by Sharvin [99], where ρ is the resistivity of the material under study and $\rho \propto l^{-1}$, i.e. R_S is independent from the mean free path, but depends only on the contact geometry. The Sharvin resistance R_S is obtained from the zeroth-order solution of the Boltzmann equation for the point contact-problem [98] and it described the ballistic injection of electrons without any scattering. Therefore the I-V characteristics of a ballistic junction would be perfectly linear and would not give any spectroscopic information.
Inelastic scattering events taking place in the bottom electrode give rise to a measurable (negative) correction to the current only if they cause the backflow of carriers through the orifice (see Fig. 3.8 b and c). The backscattered electron must jump back onto the shrunken FS and this is possible only if it can lose an energy eV in the scattering process.

This explains why in the ballistic regime the applied voltage sets the energy scale of the spectroscopic investigation. The first-order correction to the total current due to the backscattered electrons is:

$$I = -\frac{2\pi e}{\hbar}\Omega_{eff}N(0)\int_0^{eV} d\epsilon \int_0^{\epsilon} d\epsilon' S(\epsilon - \epsilon') \tag{3.8}$$

where Ω_{eff} is the effective volume in which the inelastic scattering of electrons contributing to I occurs, $N(0)$ is the density of states at the Fermi level and and $S(\epsilon)$ is the spectral function for the concerned interaction. If the elementary excitations are phonons, $S(e\mathrm{V})$ is the so-called "soft point-contact electron-phonon spectral function" $\alpha^2_{PC}\,\mathcal{F}(e)\mathrm{V}$ which differs only slightly due to the efficiency function from the thermodynamic Eliashberg function $\alpha^2\,\mathcal{F}(e\mathrm{V}\ )$ [100]. It is possible to show that:

$$\frac{d^2I}{dV^2} = -\frac{2\pi e^3}{\hbar}\Omega_{eff}N(0)S(eV) \tag{3.9}$$

is the second derivative of the current with respect to the voltage, which is proportional to the spectral function $S(\epsilon)$. Therefore, a direct measurements of the spectral function by means of point-contact spectroscopy is thus possible. According to equation 3.9, the experimental $-d^2I/dV^2$ is expected to rapidly fall to zero above the Debye energy but this very often this is not the case [98, 100] and a considerable background is found, which has been attributed to the presence of non-equilibrium phonons. In any case, it is possible to correct for the background and to determine the point-contact electron-phonon interaction function [100].

Thermal regime

If the contact radius a is much larger than the mean free path of the electrons in the metal ($K \ll 1$), the "thermal or Maxwell" regime is defined. In this case, the resistance (obtained by solving Poisson equation [100]) is:

$$R_M = \frac{\rho\ell}{2a} \tag{3.10}$$

where ρ is the bulk resistivity of the metal.
In the thermal regime, the electrons lose their energy in the contact area and this leads to a voltage-dependent heating effect and to an increase in temperature at the orifice itself. The maximum temperature T_{max} at the center of the contact can be estimated [100] by:

$$T^2_{max} = T_{bath} + V^2/4L \tag{3.11}$$

where T_{bath} is the bath temperature and L is the Lorenz number. In this case the resistance in voltage-dependent. Since in metals ρ increases with temperature, the I-V curves become S-Shaped and the conductance decreases with bias [101]. Any spectroscopic information on the electron inelastic scattering is impossible to obtain.

Diffusive regime

The intermediate regime between the ballistic regime and the Maxwell regime is called the diffusive regime. In this regime, the elastic mean free path l of the electrons is small compared with the contact radius a but the diffusion length $\Lambda = \sqrt{l_i l_e}$ for inelastic scattering is still bigger than a ($a \ll \Lambda$). The quasiparticles experience elastic scattering processes inside the contact region but not inelastic ones (see Fig.3.7 b). No heating occurs in the contact area, but the elastic scattering redistribute the electrons isotropically over the Fermi sphere, in an energy shell of width eV (see Fig.3.7 b). In this regime, direct energy-resolved information about the inelastic scattering can be obtained as well as in the ballistic regime, even if some slight differences exist. The effective volume Ω_{eff} in which the inelastic scattering of electrons give rise to the backflow current is reduced by a factor a/l with respect to the ballistic regime (see Eq.3.8). This is due to the fact that the probability for an electron to cross the contact, undergo an inelastic scattering event and then flow back through the orifice is reduced by elastic scattering in the contact region. The intensity of the spectroscopic signal (proportional to $-d^2I/dV^2$) is thus strongly reduced. Finally, a different efficiency function must be used in the spectral function $S(\epsilon)$ (see Eq. 3.9), since the elastic scattering relaxes the requirement of momentum conservation.
A simple interpolation formula for the contact resistance was derived by Wexler [102]:

$$R_N = \frac{4\rho\ell}{3\pi a^2} + \Gamma(K)\frac{\rho}{2a} \tag{3.12}$$

where the first term is the Sharvin resistance for ballistic conduction and the second one is the Maxwell resistance for the thermal regime multiplied by function of the Kundsen ratio K. Γ is always of the order of unity.
If the two metals kept in PC configuration are different, the resistance is defined as the sum of the contribution of both electrodes. If a geometrically symmetric heterocontact is supposed as well as equal Fermi parameters of the metals, the equation can be written as:

$$R_N = \frac{4\rho\ell}{3\pi a^2} + \Gamma(K)\frac{\rho_1 + \rho_2}{2a} \tag{3.13}$$

In both Eq. 3.12 and Eq. 3.13 the prevalence of the Sharvin or Maxwell terms depends only on the size of the contact. For high-resistivity materials and large-area contacts, the Maxwell contribution plays a predominant role and viceversa for clean metals and small constrictions the Sharvin resistance dominates.

3.2.2 Point-contact spectroscopy in superconductors

If the material under study is a superconductor, in addition to the information about the inelastic scattering, the point-contact technique provides a measure of the gap amplitude. This is possible thank to the Andreev reflection, the phenomenon that occur at an ideal interface between a normal-metal (N) side and the superconductor (S) to an electron that moves towards the NS interface, as described in the section 2.4.1.
It was already mentioned that the theoretical description of the AR derives from the solution of the Bogoliubov-de Gennes equations [79] near an N/S interface. In this section,

some experimental aspects will be pointed out in order to introduce the application of this technique to the study of this films, i.e. the main experimental part of this work, that will described in the next one.
In order to obtain relevant information from PCARS, the contact must fulfill the condition of ballistic regime even if also diffusive regime is reliable as well (see section 3.2.1). In ballistic contacts the gain in energy of the electrons crossing the junction is well define. Therefore in order to obtain PCARS measure, the voltage across the junction will reach values of the order of the gap or even greater. If the contact is ballistic the current density become overcritical in the contact while just outside the contact the current density decreases until it will be assume the critical value [39, 103].
Therefore it is necessary to adopt contacts which are smaller than the electron mean free path in order to avoid heating but also smaller than the coherence length in order to avoid proximity effect and destruction of superconductivity in the contact region [104]. Indeed the AR occur over a length scale of the order of the coherence length ξ at the interface which is also the length over which the proximity effect can occurs, depressing the amplitude of the gap. This effect can be neglected if the contact size is smaller than the coherence length, i.e. if the contact is ballistic.

3.2.3 Point contact spectroscopy in superconductors thin films

The measurements reported in this work were performed mainly on epitaxial thin films of $Ba(Fe_{1-x}Co_x)_2As_2$ with different Cobalt content and on $FeTe_{1-x}Se_x$ with different Selenium content. The films of both compounds were grown on CaF_2 (100) substrate. Also a sample of $Ba(Fe_{1-x}Co_x)_2As_2$ with $x = 0.08$ on MgO substrate with buffer layer was analysed. The experimental details of each sample are postpone to the follow chapter. Here the configuration of the point-contact measurements on thin films is discussed.

Experimental setup

The I-V characteristic curve of the small contact between a normal metal and the superconductive thin film were measured by using two different point-contact technique. In the first case (see Fig. 3.9) a gold wire of $\phi = 125\,\mu$m was gently pressed on the surface of the superconductor. This configuration can be seen as as an application of the "shear method" described by Naydiuk Y.G. and Yanson I.K. [105]. In this procedure the contact is formed by slightly bringing together the edges of two electrodes which can have random shapes and then by shifting one electrode along the other. In our case one electrode is the thin film and the other is the gold wire. Contacts can be obtained in many points of the surface of the film and due to the shear stresses the metal deformations and contaminations near the constriction are not so important.
Being the characterization of the sample and the study of the homogeneity of the fundamental properties one the main goal of this work, PCARS was performed in many different zone on the surface of the sample in order to build a virtual matrix of at least five different points to investigate. In this perspective the fact that the "shear" PCARS is not a destructive technique make it a good candidate for the measurements. Unfortunately

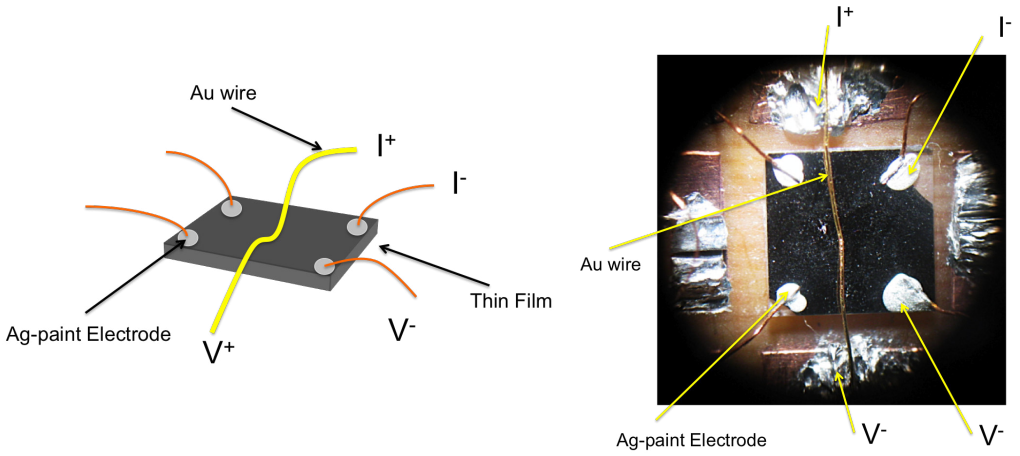

Figure 3.9: Conventional PCARS schematic mounting (left panel) and picture of PCARS on $Ba(Fe_{1-x}Co_x)_2As_2$ thin film (right panel). The current flows from the wire to the thin film and the voltage is collected between the sample and the wire.

the poor thermal and mechanical stability makes temperature dependence measurements really difficult to perform. Really few temperature dependence measures were obtained before that the resistance of the contact had changed. A lucky example obtained on 8% Co-doped $Ba(Fe_{1-x}Co_x)_2As_2$ thin film on Fe-buffer layer+MgO substrate is reported in Fig. 3.10. Therefore, the "soft" point-contact technique was preferred instead of this one.

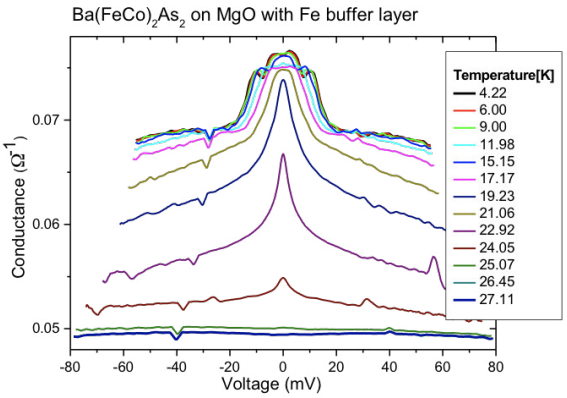

Figure 3.10: Temperature dependence of the spectrum of "shear" PCARS on the $BaFe_{1.84}Co_{0.16}As2$ thin-film show in right panel of Fig. 3.9.

In this second case a thin Au wire ($\phi = 10\mu$m) is fixed on the surface by using a small spot of Ag paint (see Fig. 3.11). The dimension of the microscopic contact is about 50μm in diameter and it is manually made. Even if the contact size is not comparable to the mean free path of the superconductor, the effective area of the contact is much smaller because the pint does not stick completely on the surface of the crystal. Furthermore the contact is

actually the parallel of several microjunctions, i.e. the measure is an average over a certain region of the surface.
Also in this configuration pressure is is not applied on the sample. It is not a destructive technique and the contact has also good mechanical and thermal stability. Good temperature dependence measurements were performed by using this technique and many of the results discussed in this work were obtained in this way.

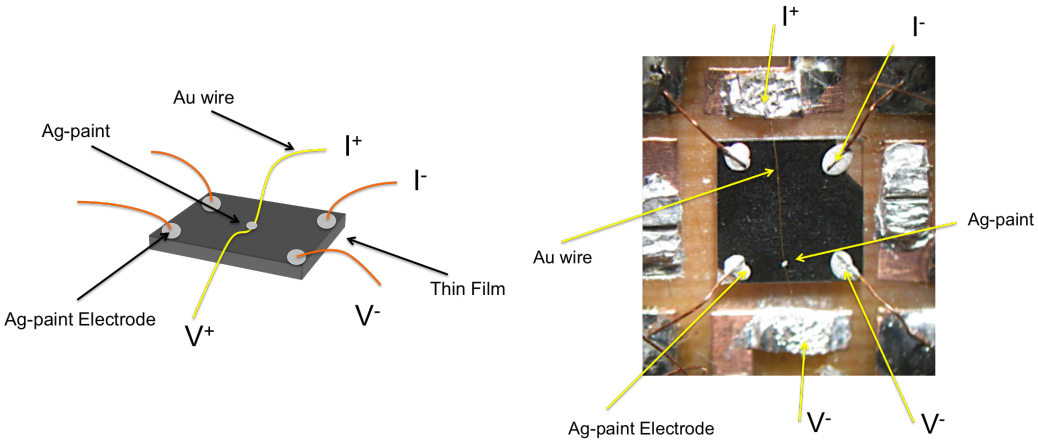

Figure 3.11: Unconventional PCARS schematic mounting (left panel) and picture of PCARS on $Ba(Fe_{1-x}Co_x)_2As_2$ thin film (right panel).

In this two configurations of this pseudo four-probe technique, the current is injected from the gold wire into the sample and the voltage is collected at the other two terminals (see Fig.3.9 and Fig.3.11). The current is not injected only along one direction, as in tunnelling spectroscopy, but through a large-angle cone as was described in section 2.4.1 where the transparency as a function of the angle between the direction of the incident electron and the normal to the interface NS in the BTK model was introduced.
Each thin film or part of the thin film (for example in case of the $Ba(Fe_{1-x}Co_x)_2As_2$ which was of 1cm x 1cm size where cut in four pieces) is fixed on the board where four tin-electrodes are connected to the sample by using wire and Ag conductive paste. The device is usually assembled in a glove box under inert atmosphere (Nitrogen, Helium or Argon) in order to protect the sample from degradation during al mounting time. The board on which the sample was mounted was then fixed on the cryogenic insert as shown in Fig. 3.12, ready to be cooled in a standard liquid He dewar.

A DC current is injected and for each value the current is inverted. The I-V characteristics is then acquired and the differential conductance is obtained by numerical differentiation calculated by ad hoc made Labview programs.
The current is injected into the sample by means of current source (Keithley 220) and voltage is measured on a voltmeter Hewlett Packard 3457A. The temperature is registered by means of an SMD sensor mounted very close to the sample. The thermometer was connected either to a Digit-multimeter Agilent 34410A.

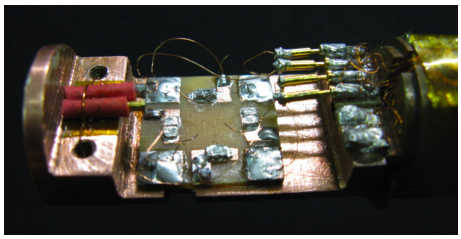

Figure 3.12: Cold head of the cryogenic insert with the board for the PC.

Non-ideal effects in the contact

The experimental normalized conductance curves obtained by means of "soft" PCARS technique show a systematic lower height and larger width than what expected in theory. Here the main effects that can modify the ideal BTK conductance curves are introduced briefly.

- *Dips*
  The point-contact spectrum between a normal metal and a superconductor often shows unexpected sharp dips in the differential conductance at voltage values that are larger than the superconducting energy gap, or sometimes close to the gap values as it is reported in Fig. 3.13. These dips are not predicted in the BTK theory,

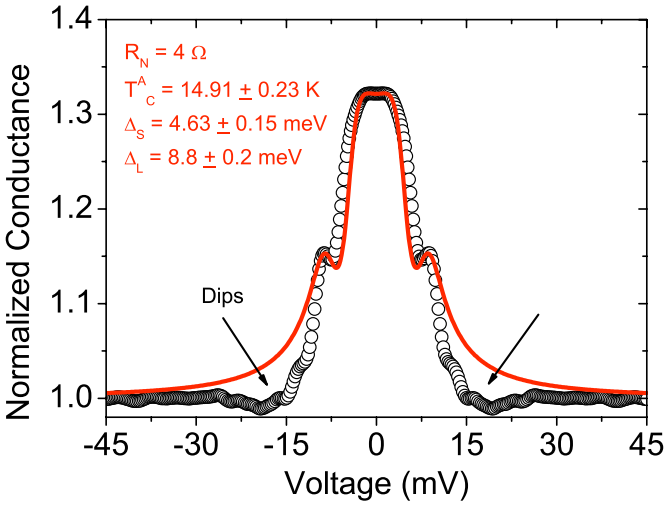

Figure 3.13: Normalized differential conductance of a point contact between a normal metal and a superconductor.

which is commonly used to fit conductance curves. Sheet et al. [106] performed a systematic study of this phenomenon in great number of contacts between different combinations of superconductors and normal metals. It turns out that the dips are the sign of non pure ballistic regime because, at low current values through the

contact. Indeed the resistance of the contact (see Eq. 3.12) has a Sharvin and a Maxwell contribution: when the current reaches the critical values in the superconductor, a normal region can appear next to the contact. Therefore, a sharp rise in the voltage across the junction (due to contribution of the non-zero resistance of the superconductor) occurs and a dip appears in the differential conductance. When a PCARS spectrum shows dips, it is usually analyzed by using BTK model ignoring them if they are small, because the BTK is not able to reproduce them. However this procedure introduces a small error in the determination of the gap [106].

- *Diffusivity of the contact*
  The diffusivity in the contact has been theoretically addressed by Mazin et al. [107] and turns out to affect only the Z parameter. A diffusive AR contact can be viewed as a contact between the normal and the superconducting compounds which, in addition to the interface, are separated by the diffusive region larger than the electronic mean free path. In this case the conductance of a diffusive junction with a given barrier parameter Z can be fitted with a ballistic (BTK) model with an effective $Z_{eff} > Z$ and then it is difficult to discern the effect of a finite Z in a ballistic contact from the effect of diffusive transport [2]. This is even more common at higher temperatures and for higher values of the lifetime broadening, i.e. when the curves are more smeared out.

- *Proximity effect*
  In order to avoid the proximity effect, the radius of the contact should be smaller than the coherence length. Actually in iron based superconductors thin films is not an easy task due to the strong effects of the substrate. Therefore, in order to check also this aspect, the obtained gap values measured in those systems are always compared with the values obtained by other experimental techniques.

- *The spreading resistance*
  A so-called "spreading resistance", i.e. a non-negligible additional resistance which can shift the conductance peaks to higher energies, leading an overestimation of the gap is considered in series with the contact resistance [101, 108] in measurements performed in thin films. In these systems it plays an important role while in bulk or highly conductive samples it is much smaller than the contact (junction) resistance and can thus be neglected.
  The anomalous shift of the tails observed in the conductance curves of thin films just above T_c is probably due to this effect. In Fig. 3.14 is shown an example of this effect, due to a temperature- and current-dependent spreading resistance contribution. Despite Chen [109] and Döring [110] have already proposed a model in order to explain this phenomenon, a model that allows a quantitative analysis of the conductance curve still lacks. The difficult arises from the large number of the parameters which are required. The resistivity ρ(T), the shape of the current I(V) and the critical current J_c(T) and their variation as a function of the temperature

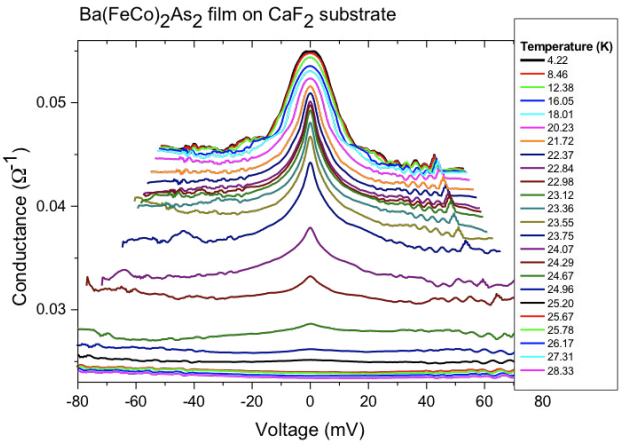

Figure 3.14: Temperature dependence of the spectrum of a point contact on 8% Cobalt-doped thin film up to the critical temperature and above.

have to be known in this quantitative model. Neither of them is easy to know, in particular the critical current. On the other side, the contact radius "a", the mean free path "ℓ" as well as the resistance due to the Sharvin resistance of the compounds in the normal state can be treated as free parameters, as it is impossible almost to determine by direct measurements.
The normalisation of the PCARS spectra measured on thin films resulted rather critical because of the unusual features and the details of this process will be explained in the follow lines.

A possible explanation for unusual features of PCARS spectra in thin films

A possible explanation of these unusual features of PCARS spectra in thin films was argued within the model that is here introduced. The schematic image of the resistance values of a junction between the gold wire and the thin film is shown Fig. 3.15. The current is injected from the wire into sample and the voltage is measured between the wire and and the surface of the film.

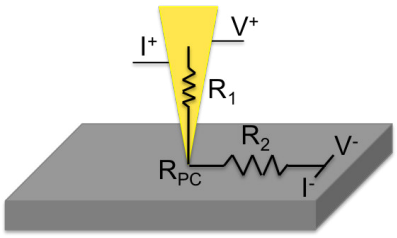

Figure 3.15: Schematic view of the resistance values in a PC mounting.

When the point contact between two normal metals NN is perfect ballistic (see 3.2.1), the

resistance between the two electrodes is given by three different contributes due to the resistance of the gold wire, the resistance of the point contact [64] and the resistance of the thin film in normal state. Therefore it can be written as

$$R = R_1 + R_{PC} + R_2(T) \tag{3.14}$$

where the resistance of the contact R_{PC} is given by Eq. 3.7 and the resistance of the thin films R_2 depends on the temperature of the bath.
When the point contact between two normal metals NN is not ballistic (see 3.2.1), the resistance R_{PC} is given by the sum of the Sharvin term and the Maxwell term:

$$\begin{aligned} R &= R_1 + R_{PC} + R_2(T) && (3.15)\\ &= R_1 + R_S + R_M + R_2(T) && (3.16)\\ &= R_1 + \frac{4\rho\ell}{3\pi a^2} + \frac{\rho_1(T)}{4a} + \frac{\rho_2(J,T)}{4a} + R_2(T) && (3.17) \end{aligned}$$

When the thin film becomes superconductive (i.e. the temperature and the current density are below to the critical values) $R_2 = 0$. The resistance of the point contact in a diffusive-regime between normal metal and superconducting metal NS can be written as a sum of the resistance of the gold wire, the Sharvin term and the Maxwell term of the resistance of the wire:

$$R = R_1 + \frac{4\rho\ell}{3\pi a^2} + \frac{\rho_1(T)}{4a}. \tag{3.18}$$

where $\rho_1(T)$ is the resistivity of the wire (normal metal) as a function of the effective temperature of the contact (i.e. the temperature of the bath and the heating term) and $\rho_2(J,T)$ (i.e. the resistivity of the thin film) is zero if $T < T_c$ and $J < J_c$.
When $\rho_2(J,T) \neq 0$ the Maxwell term due to the superconductor appears in Eq. 3.18. This can happen even when below T_c if the current flowing into the contact becomes overcritical. However when this happens, heating occurs in the contact region so that the temperature there can increase very much the temperature above the bath. In terms this makes the critical current density decrease. Clearly accounting these effects in a model requires a recursive solutions of self-consistent equations. This point is under revision and technical aspects remain still open.
In the following T is the temperature of the bath and the heating contribution to the temperature of the contact is neglected. The measured voltage is given by the sum of the voltage difference that the electrons feel when they are Andreev reflected (V_{AR}) and the voltage due to the additional resistance that comes from the not-ballistic contact and the portion of film between the point contact and the voltage electrode (see Fig. 3.15).
The voltage measured in the proximity of the resistive transition can be written as:

$$\begin{aligned} V &= V_{AR} + (R_1 + R_1^M + R_2^M(J,T) + R_2(T))I \\ &= V_{AR} + \left(R_1 + \frac{\rho_1}{4a} + \frac{\rho_2(J,T)}{4a} + R_2(T)\right) && (3.19) \end{aligned}$$

since the resistivity of a good conductor (Au wire in this case) $\rho_1(T)$ is considered a constant at low temperature and the resistivity of the superconductor $\rho_2(J,T)$ depends

only on the temperature of the bath in first approximation.
Therefore, the conductance turns out to be

$$\begin{aligned}\frac{dI}{dV} &= \frac{\frac{dI}{dV_{AR}}}{1+(R_1+R_1^M+R_2^M(J,T)+R_2(T))\frac{dI}{dV_{AR}}} \\ &= \frac{\sigma_{BTK}}{R_{NN}\left(1+\frac{R_1+R_1^M+R_2^M(J,T)+R_2(T)}{R_{NN}}\sigma_{BTK}\right)}.\end{aligned} \tag{3.20}$$

where σ_{BTK} is the normalized conductance as described by the BTK model and R_{NN} is the normal-state resistance of the contact. The experimentally observed shift of the tails of the PCARS spectra in the proximity of T_c is explained by the last term, while the change in the slope of the high voltage tails is explained also by the second-last term.
In other words, if the contact is in the diffusive regime, the additional resistance cannot be eliminated by reducing the distance between the electrodes and the resistance of the contact is given by Wexler formula (Eq. 3.13) for two different materials, i.e in this case $\rho_1 = \rho_{Ag}$ and $\rho_2 = \rho_{film}$. When the film is superconducting, only the resistivity of the Ag paste plays a role and it is approximately temperature-independent. If the contact is in diffusive regime, also the resistivity of the superconductors gives a contribution across the transition and causes a stretching of the curves along the V axis, i.e. a small overestimation of the gap. If the resistive transition of the film is not too narrow, the resistivity of the film starts playing a role at $T_c^{zero}$and this causes the downward shift of the curves and the stretching of the voltage axis at high T as shown in Fig. 3.16.

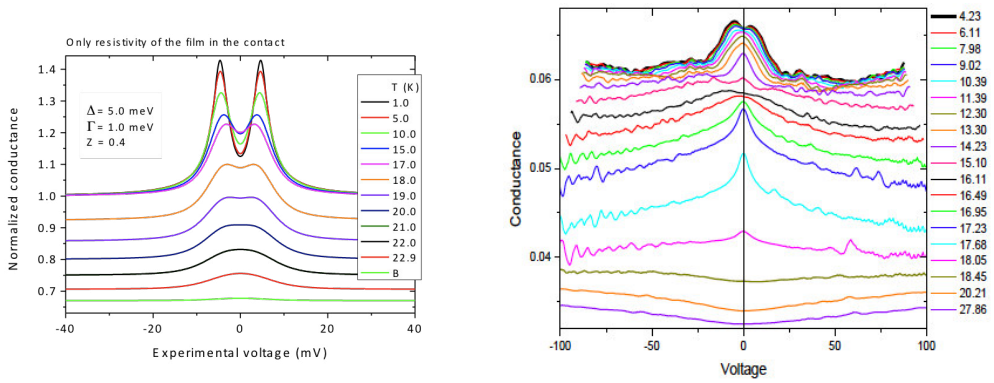

Figure 3.16: Downward shift of the curves calculated within the spreading resistance model (left panel) and PCARS spectra measured on epitaxial $FeSe_{0.5}Te_{0.5}$ thin film (right panel).

Therefore considering the contribution of the spreading resistance here described, the current I can be expressed as a function of the normalized conductance (calculated within the BTK model) as

$$I(V_{AR}) = \int_0^{V_{AR}} \frac{dI}{dV'}dV' = \frac{1}{R_{NN}}\int_0^{V_{AR}} \sigma_{BTK}(V')dV'. \tag{3.21}$$

In this way, the experimental value of the conductance dI/dV can be calculated as a function of the voltage V_{AR} (i.e. the voltage drop associated with Andreev reflection). This is

convenient since σ_{BTK} is expressed as a function of V_{AR} (see Eq. 3.19. Unfortunately, V_{AR} is not accessible experimentally since it depends on $\rho_2(J,T)$. Therefore, once the experimental conductance curve $dI/dV(V_{AR})$ has been calculated, the voltage transformation $V_{AR} \rightarrow V$ has to be carried out to reproduce the horizontal stretching of the curves.
This is only the preliminary model elaborated in order to study these features of the thin film PCARS spectra and many steps are still required before it can be used in fitting procedures.

The fit of experimental conductance curves

In this work, the normalized curves were fitted preliminary with the BTK model generalized by Kashiwaya and Tanaka [81, 111] (called the "2D-BTK model") in order to extract the gap values, as discussed in the following part of this chapter. This model is based on the assumption of spherical FSs in both the normal metal and the superconductor, which is clearly a strong simplification in the case of Fe-based compounds but allows obtaining good results as a first approximation, as is shown in the two chapters devoted to the Ba122 and Fe(Te,Se) compounds.
In order to fit the experimental conductance curves, obtained by numerical differentiation of the measured I-V curves, the first fundamental step is the normalization procedure. Each experimental conductance curve has to be divided by its relevant normal-state conductance curve measured at the temperature $T < T_c$ of the PCARS and applying a magnetic field $H > H_{c_2}$. Usually in Fe-based SCs and also in High T_c SCs, H_{c_2} is too high to be experimental accessible. Therefore the normal state curve of the contact is measured at $T > T_c$ over the critical temperature which unfortunately in Fe-based materials is usually different to the normal-state curve al low temperature, due mainly to the the anomalous features previous described.
In this work the low-temperature conductance curves ware divided by a polynomial curve obtained as a fit of their own high-voltage conductance curve. Examples of normalized curve of each compounds will be shown in the following chapters.

Local critical temperature measured on micrometer scale

At the end of this chapter on resistance measurements and PCARS techniques, a useful application (even not the traditional one) of the PCARS is shown here. In order to characterize the homogeneity of the superconducting properties of each sample, as previous described, the critical temperature in ab-plane was measured by collinear and van der Pauw technique. The R vs T curve measured by this traditional technique is then compared to the local T_c^A measured by PCARS in order to check whether the T_c measured in in a specific point of the sample surface (i.e. a region of 10 x10 μm and more) is representative not only of the local properties of the same sample. In this case, the local T_c is identified with the temperature T_c^A at which Andreev-reflection features disappear. The comparison between the values of T_c^A measured in different points (yellow points in the inset) of a thin film and the R vs T curve of the same film measured by van der Pauw technique (red points in the inset) is shown in Fig. 3.17. Since the PCARS spectrum is

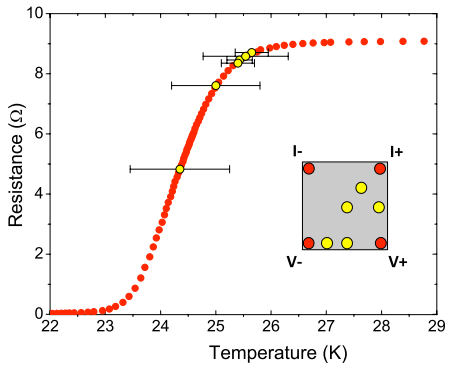

Figure 3.17: The local T_c^A values determined by PCARS (yellow points) compared with the R vs T curve (red points) on a 8%-Cobalt doped Ba122 thin film. The inset shows schematically the surface of the film, with the contacts of for resistance measurements (red dots in the main figure) and the regions where the point-contact measurements were carried out (yellow dots). The horizontal coordinate of the yellow points in the main figure represents the local T_c^A, while the vertical coordinate is arbitrary and has been chosen to coincide with the resistance of the film at that temperature.

acquired at thermal equilibrium, the uncertainty on T_c^A comes from the temperature step between the first normal state spectrum and the last superconductive one. In most of the measurements, the local T_c^A agrees very well with the R vs T curve and lie between T_c^{90} and T_c^{10}. This confirm the good homogeneity in term of superconductive transport properties of the thin film and also indicates that there is no significant heating in the contact region (i.e. the temperature of the contact is not higher than that of the bath). Further results will be shown for each materials studied in this work.

Chapter 4

$Ba(Fe,Co)_2As_2$

In this chapter are discussed the measurements collected on epitaxial $Ba(Fe,Co)_2As_2$ thin films with nominal Co content x ranging from 0.04 to 0.15, i.e., from the underdoped to the overdoped region of the phase diagram.
The systematic surface characterization and resistance measurements were performed on the samples. Then PCARS measurements collected on them were analysed within the 2D and 3D BTK model and also within Eliashberg theory in order to give a contributution to the study of the number and the amplitude of the energy gaps, and the coupling mechanism in Fe-based superconductors.

4.1 Surface characterization of $Ba(Fe,Co)_2As_2$ thin films

In this section the systematic characterization of the thin films by using different and complementary techniques is discussed. The morphological characteristics of the surface, the structural properties, the transport properties, in terms of critical temperature on millimeter and micrometer scales, and energy gaps were studied in order to check the homogeneity of the superconductive properties. The superconducting properties (critical temperature, number and amplitude of the energy gap) are also compared with those of single crystals of the same compound. Here the study of the 8% Co doped sample is discussed in details, but all the samples were characterized by using the same procedure.

4.1.1 Samples growth

The $Ba(Fe_{1-x}Co_x)_2As_2$ thin films with a thickness of 50 nm were deposited on $(001)CaF_2$ substrates by pulsed laser deposition (PLD) [112] using a polycrystalline target with high phase purity [112, 113] by the group of prof. Holzapfel at IFW Dresden. The surface smoothness was confirmed by in-situ reflection high energy electron diffraction (RHEED) during the deposition; only streaky pattern were observed for all films indicative of smooth surfaces. The details of the structural characterization and of the microstructure of these

high-quality, epitaxial thin films can be found in ref. [112]. Standard four-probe resistance measurements were performed in a ^{4}He cryostat to determine the transport critical temperature and the transition widths, reported in Table I. With respect to most phase diagrams of $Ba(Fe_{1-x}Co_x)_2As_2$ single crystals [114, 115, 116], where the optimal doping corresponds to $x \simeq 0.065$, the highest T_c^{90} of our films is attained for $x = 0.10$ and in the $x = 0.15$ sample the T_c^{90} is still about 22 K. This wide doping range of high T_c could be due to a combination of epitaxial strain from the substrate and of reduced Co content in the film with respect to the nominal one.
In the follow, the doping content of the target is usually the reference doping content. This does not hamper the discussion, since all the results are referred to the critical temperature of the contact, which is a local property directly correlated to the gap amplitudes (as demonstrated in many different cases [2]) and is thus well defined irrespectively of the actual Co content.
One $Ba(Fe,Co)_2As_2$ (with 8% Cobalt content) thin film was also deposited on MgO (001) single-cristalline substrate with a Fe buffer layer of 20 nm in between the substrate and the thin film [113]. The superconducting transition of the film has a midpoint at $T_c^{mid} = 23.80$ K and the width of the transition is $\Delta T_c = T_c^{90\%} - T_c^{10\%} = 1.50$ K. The measurements performed on this sample will be discussed in the last section of this chapter where directional PCARS in Co-doped Ba122 thin films is reported.
In Fig. 4.1 the schematic structure of the two different kinds epitaxial thin films are reported in order to clarify the geometry of the systems analysed in this chapter.

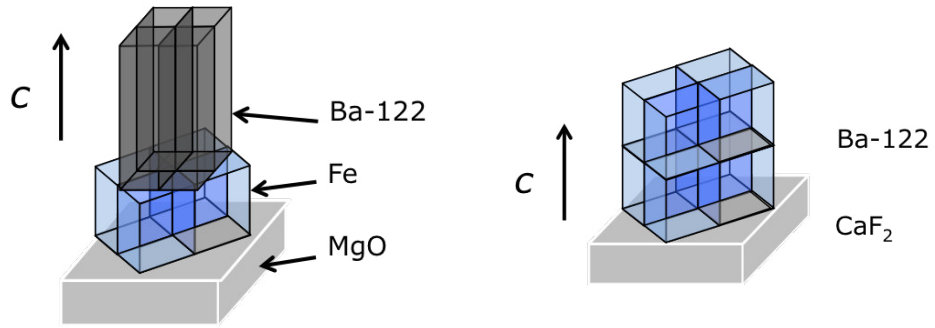

Figure 4.1: Schematic illustration of the Ba 122 thin film structures on on MgO substrate with Fe layer (left) and on CaF_2 substrate (right).

4.1.2 Chemical analysis

Energy dispersive X-Ray (EDX) spectroscopy remains on of the standard way to measure the quantity of chemical elements (especially metallic) in compounds. Also Fe-based SCs were characterized by this techniques [117, 118].
In superconducting thin films, the chemical characterization is a crucial analysis in order to understand the effects of the chemical doping on the superconducting properties and then the phase diagram of the compounds. In these systems, strain/ stress of the substrate,

doping content and impurity disorder can play similar effects on the superconducting properties [32, 119]. Because of the strain/stress induced by the substrate in this systems, it is impossible to determine the doping content by measuring the lattice parameters and comparing the results with single crystals data, as instead is commonly done in the case of the bulk material.
The Cobalt content was measured directly on the Ba122 thin films by means of energy dispersive X-Ray (EDX) spectroscopy (with an EDX Oxford X-ACT spectrometer), even if the doping content of the target is usually considered as the reference doping. Different spectra were obtained on the same film, either over areas of a few square microns, or in single points.
An example of the EDX analysis performed on the 8% Co-content thin film on CaF_2 is shown in Fig. 4.2 where the EDX spectrum and the SEM image which shows the area analyzed are reported.

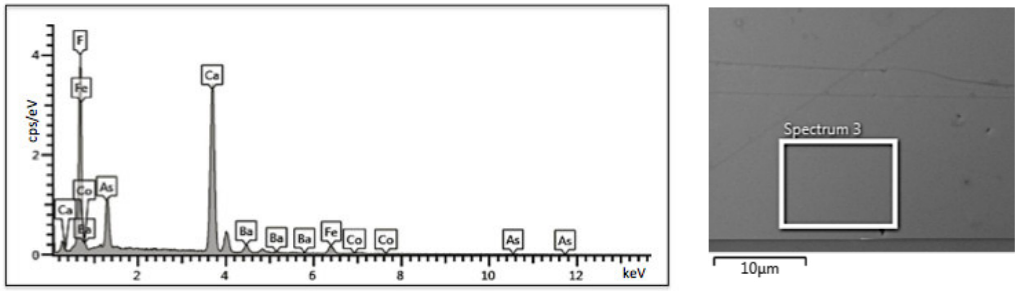

Figure 4.2: EDX spectrum of 8% Co-content thin film on CaF_2 (left panel) and the corresponding SEM image of the analyzed area (right panel).

Element	Atomic (%)
F	67.55
Ca	23.54
Fe	2.82
Co	0.24
As	4.49
Ba	1.37
Total	100.00

Table 4.1: Element of the 8% Co-content thin film on CaF_2 measured by EDX analysis shown in Fig. 4.2.

Because of the very small thickness of the films as compared to the depth probed by EDX, a large signal from the CaF_2 substrate was always observed, as it is also shown in Table 4.2 where the composition of the Atomic % analysis of the EXD spectrum shown in Fig. 4.2 is reported. In Fig. 4.3 the EXD analysis of a sample with the 8% Co-doped Ba122 compounds on MgO substrate with Fe layer in between them is reported. Also in this case a large signal from the elements of the substrates was detected and the quantity of Fe element of the superconductor is more difficult in respect to the samples on CaF_2 substrate

due to the presence of the Fe buffer layer.

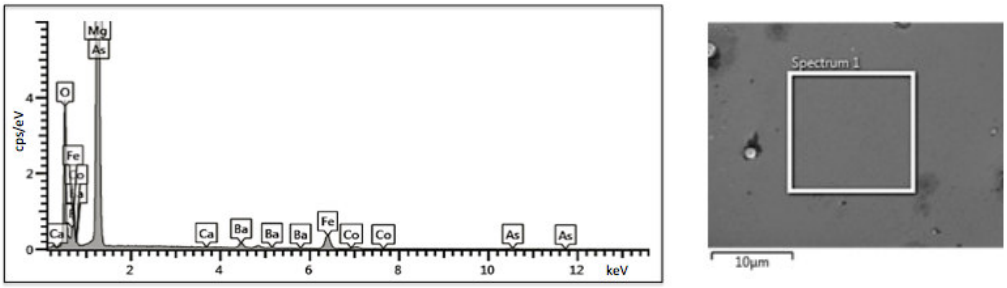

Figure 4.3: EDX spectrum of 8% Co-content thin film on MgO + Fe buffer layer (left panel) and the corresponding SEM image of the analyzed area (right panel).

Element	Atomic (%)
O	45.64
F	0.00
Mg	46.75
Ca	0.00
Fe	5.09
Co	0.21
As	1.44
Ba	0.85
Total	100.00

Table 4.2: Element of the 8% Co-content thin film on CaF_2 measured by EDX analysis shown in Fig. 4.2.

The chemical compositions was determined from all the spectra analysed in this study and it turned out to be well consistent with one another. On averaging over all the spectra, the values obtained for the Co content in the different samples, are in general in good agreement with the nominal value. For example, the experimental Co content $x = 0.084 \pm 0.017$ was measured in the sample with nominal Co content $x_{nom} = 0.08$ referred to Fig. 4.2. The uncertainty $\delta = 0.017$ is here equal to one half of the spread of x values obtained in single spectra.

4.1.3 Surface morphology

The morphological characteristics of the surface (granularity, roughness) and the structural properties (epitaxy, texture) are discussed in this subsection.
Fig. 4.4(a) shows a reflection high-energy electron diffraction (RHEED) image of one of the CaF_2 substrates of the thin films after cleaning and thermal treatment. Here the incident electron beam is parallel to the [110] direction of the CaF_2 substrate. Streaks and well distinct Kikuchi lines are observed, which indicate a smooth and single-crystal surface of the CaF_2 substrate. A RHEED image of the Co-doped Ba-122 thin film grown on this

substrate, taken just after the deposition, is shown instead in Fig 4.4b. The pattern in this case shows long streaks perpendicular to the shadow edge, and centered at positions on the Laue circles. This is typical for a multilevel surface, i.e. for a high number of grains with smooth terraces. This is only one example of the RHEED measurements performed by K. Iida and coworkers [33] in order to check the quality of the deposition. In one of the thin film with 8% Co content, the morphology suggested by the RHEED is confirmed by direct imaging of the film surface direct imaging of the thin film surface performed by field emission-scanning electron microscopy (4248 Merlin ZEISS FESEM). This is one of the common techniques used to the study of morphological characteristics of thin films microstructural analysis on superconducting chalcogenides and pnictides compounds [120, 121].
Fig. 4.5a shows a secondary-electron (SE) image taken over an area of about 1.8 x 1.8 m^2. This image mainly carries morphological/topographical information; flat and smooth terraces, with parallel edges of about $100-150$ nm in size are clearly visible, which protrude from a pattern of well connected grains. This further indicates that Co-doped Ba-122 films grow in a terraced island mode. Fig. 4.5b reports a greater-magnification (i.e. smaller-scale) image taken on a different region of the film surface, and Fig. 4.5c shows a backscattered-electron (BSE) image of the same area. A diagonal stripe-like pattern not related to the granular structure is very clearly seen in this picture (and also, though less clearly, in panel (b)); this pattern might be associated with correlated defects along the c axis. Additional and complementary information about the surface morphology was collected by means of atomic-force microscopy (AFM) measurements. Fig. 4.6a and b show two AFM images taken on the same region of the film, though on a different scale. The correspondence between color and height is shown by the vertical bar on the right side of each picture. The flat terraces with parallel edges already observed by FESEM are very clearly visible here; the additional information is that their top surface is flat but not perfectly horizontal. The distribution of heights calculated over the whole area shows a broad maximum at 5 nm. The root mean square (RMS) roughness is 1.15 nm while the size of the terraces, determined by means of z-height profile cuts, ranges between 50 and 200 nm. Fig. 4.6c and 4.6b show the same image but in the second one a Prewitt gradient filtering was applied. This allows highlighting the elevation of the terraces above the background.
The surface analysis of the 8% Co-doped Ba-122 thin film previous discussed is only an example of the result obtained on the different Co-content Ba-122 samples. In Fig. 4.7 FESEM measurements (left panel) performed on the 2% Co-doped Ba-122 thin film are compared with the results of the AFM analysis (right panel). Clear, regular, flat terraces of rectangular shape are visible also in this sample even the sample seems to show a less ordered structure in respect of the 8% Co-doped Ba-122 sample and less visible in the AFM image. The root mean square (RMS) roughness is 2.23 nm while the size of the terraces, determined by means of z-height profile cuts, ranges between 15 and 100 nm.
FESEM measurements were also performed on the 8% Co-content Ba122 thin film on MgO substrate. In Fig. 4.8 some defects of this sample are shown. Deep cracks (panel a), layered growth on the surface (panel b) and deep hole in which disordered grains appear (panel c) are clear visible in this sample together with the regular, flat terraces of rectangular

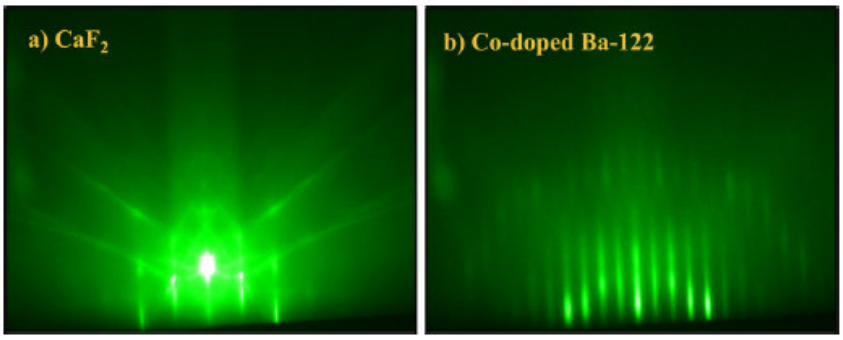

Figure 4.4: RHEED images of (a) the CaF_2 substrate and (b) the 8% Co-doped Ba-122 thin film. In the latter case, the picture was acquired after the deposition at room temperature. The basal plane of Co-doped Ba-122 is rotated by 45◦ with respect to the substrate. Hence the electron beam is here parallel to the [100] direction of the Co-doped Ba-122.

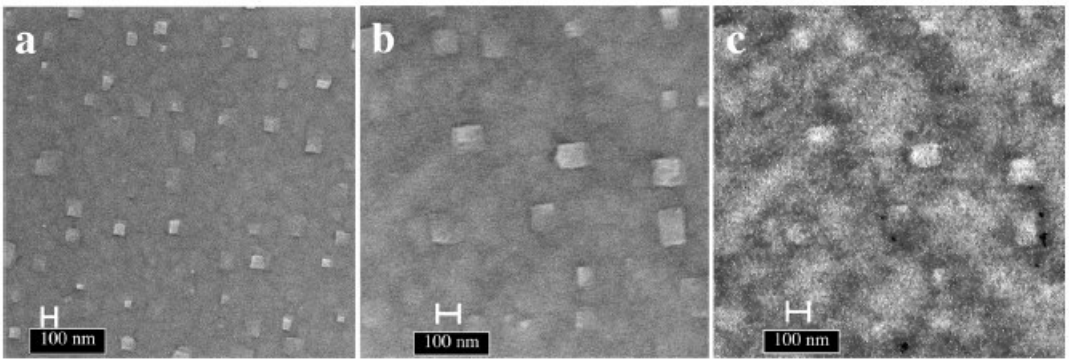

Figure 4.5: FESEM images of the surface of a 8% Co-doped Ba-122 thin film deposited on CaF_2 substrate. (a and b) Two representative secondary-electron (SE) images with different magnifications (the scale is indicated in the labels). Clear, regular, flat terraces of rectangular shape (side length approximately 100 nm) are seen that protrude from an arrayof well-connected grains. (c) Backscattered-electron (BSE) image of the same area as in (b), that shows a diagonal stripe-like pattern not related to the granular structure, and possibly indicating the existence of correlated defects parallel to the c axis (i.e. perpendicular to the plane of the figure).

shape characteristic of the Co-doped Ba-122 thin films. The defects revealed by FESEM analysis sum up to the evidence of the current shunting by the Fe-layer have induced to prefer Ba-122 material deposited on CaF_2 substrate.

4.2 Resistance measurements

Standard four-probe resistance measurements were performed in a ^{4}He cryostat in order to determine the transport critical temperature and the transition width. The measurements were conducted by using either the standard collinear configuration (with contacts along the diagonal of the 5 mm x 5 mm film) or the van der Pauw (vdP) configuration, with four contacts on the corners (see the Fig. 4.9). A typical result of a R(T) measurement

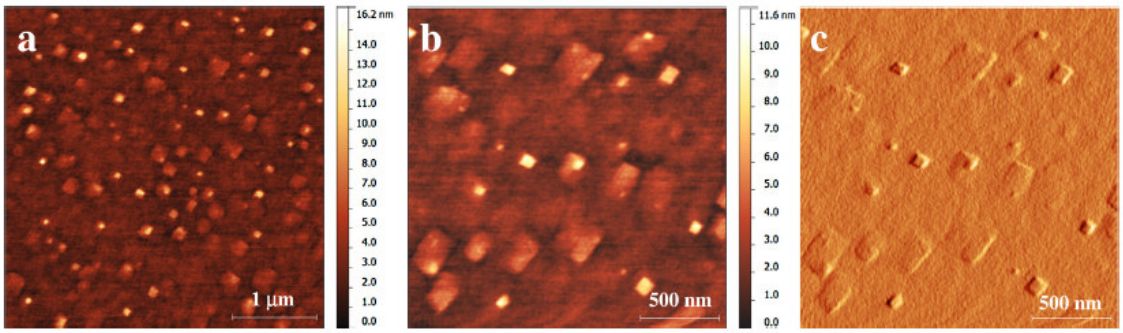

Figure 4.6: Examples of AFM measurements on the surface of a Co-doped Ba-122 thin film. (a) AFM image over an area of 3.75μm x 3.75μm, exhibiting a clear pattern of flat, rectangular terraces of about 100 nm in size. A comparison with the FESEM image of Fig. 4.5a (taken on a similar scale) shows that the morphological information provided by FESEM and AFM is perfectly consistent; note that the latter does not show the stripe-like pattern seen in Fig. 4.5c. (b) AFM image over a smaller area of 2μm x 2μm and thus with a greater magnification. (c) The same image as in (b) but after application of a Prewitt horizontal gradient filter so as to highlight the elevation of the terraces above the background of well-connected grains.

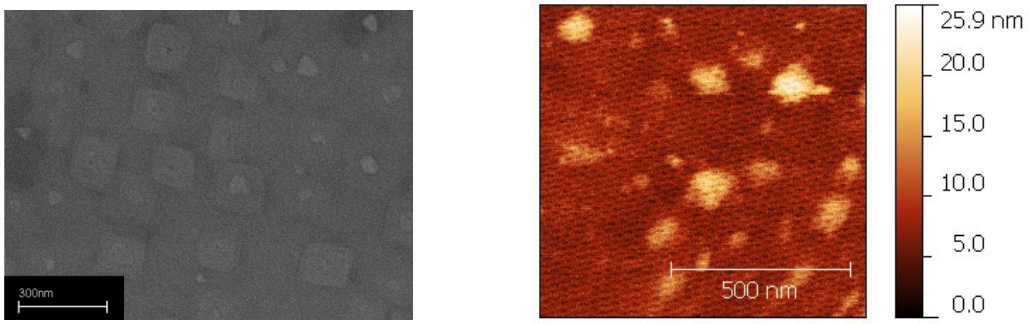

Figure 4.7: FESEM image of the surface of a 2% Co-doped Ba-122 thin film deposited on CaF_2 substrate (left panel). A representative secondary-electron (SE) image shows regular, flat terraces of rectangular shape, that are less visible in the AFM image (right panel).

up to 250 K is shown in the right inset to Fig. 4.9 (solid line) where the measure on 8% Co-doped Ba122 thin film is reported. Here the vdP configuration was used; current was flowing through the two top contacts and the voltage drop was measured across the bottom ones (see left inset). None of the curves measured in the films showed anomalies that could suggest the existence of macroscopic inhomogeneities either in the transition temperature or in the normal-state conductivity [95, 122]. In the normal state, the R(T) curve displays a minimum around 75 K. A comparison with the resistivity curves of single crystals [115] shows that this shape is typical of the underdoped region, while in optimally-doped ($x = 0.061$) and overdoped crystals the R(T) curve is monotonic. The right inset in Fig. 4.9 shows the resistance of the film compared to the resistivity of a single crystal with $x = 0.051$ (dashed line), both normalized to their values at 250 K. Further indication

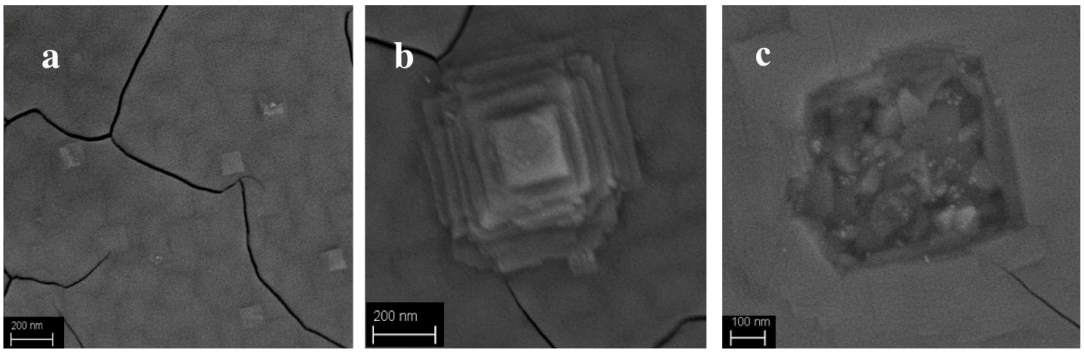

Figure 4.8: FESEM images of three different defects of the surface of the 8% Co-doped Ba-122 thin film deposited on MgO substrate with Fe buffer layer. Deep cracks (a), layered growth on the surface (b) and deep hole in which disordered grains are clear visible (c).

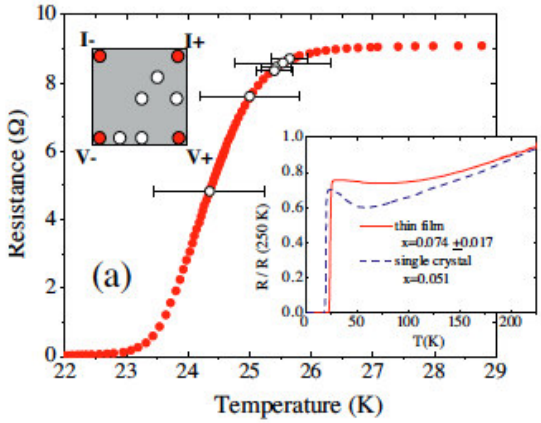

Figure 4.9: Transport measurements on a Co-doped Ba-122 thin film. The local critical temperature determined by PCARS (hollow symbols) compared to the resistive transition of the same film (red filled symbols). Left inset: a drawing of the film indicating the contacts used for the resistance measurement (red dots) and the regions where the point contacts were made (white dots). Right inset: the normalized resistance $R(T)/R(250K)$ compared to that of slightly underdoped single crystals [115].

that our films lie in the slightly underdoped region of the phase diagram comes from the fact that in the films deposited on CaF_2 substrate the highest T_c is achieved for $x = 0.10$ [35] as it will be clear in the next section.
Considering the superconducting transition, it is possible to notice that the resistance drops to 90% of its residual value at $T_c^{90} = 25.2$ K and to 10% at $T_c^{10} = 23.5$ K (see main panel of Fig. 4.9). The zero-resistance state is reached at $T_c^0 = 22.9$ K. Resistance measurements over a whole set of films with the same doping content (but from different batches) have given the average values $T_c^{10} = (23.85 \pm 0.35)$ K and $T_c^{90} = (25.4 \pm 0.2)$ K.
The same investigation were performed on the other Ba-122 thin films. The results of the resistance measurements in term of T_c^{90} and T_c^{10} are summarised in Table 4.3. The resistivity measurements shows that the film with $x = 0.15$ is in the overdoped region, since:

i) its $\rho(T)$ curve does not show the low-temperature upturn typical of underdoped samples [115], observed instead in the films with $x = 0.04$ and 0.08; ii) its critical temperature is smaller than in the optimally-doped film ($x = 0.10$). The phase diagram of these films

x	T_c^{10} (K)	T_c^{90} (K)	ΔT_c (K)
0.04	7.0	9.5	2.5
0.08	23.9	25.5	0.8
0.10	26.6	24.6	1.0
0.15	22.0	20.6	0.7

Table 4.3: Critical temperatures of our films determined from electric transport measurements. T_c^{90} and T_c^{10} are the temperatures at which the resistance (the resistivity) is 90% and 10% of the normal-state value immediately before the transition. ΔT_c is defined here as $(T_c^{90} - T_c^{10})/2$. The values reported for $x = 0.08$ are actually averaged over 3 different films.

shows a superconducting dome which is shifted to higher doping (and also extends to higher temperature) with respect to that of single crystals (see Fig. 4.10). The confirmation of the Co content of the films provided by EDX (see above) rules out a systematic overestimation of the doping, so that the only factor responsible for the wider superconducting dome of films is the effect of the substrate [112].

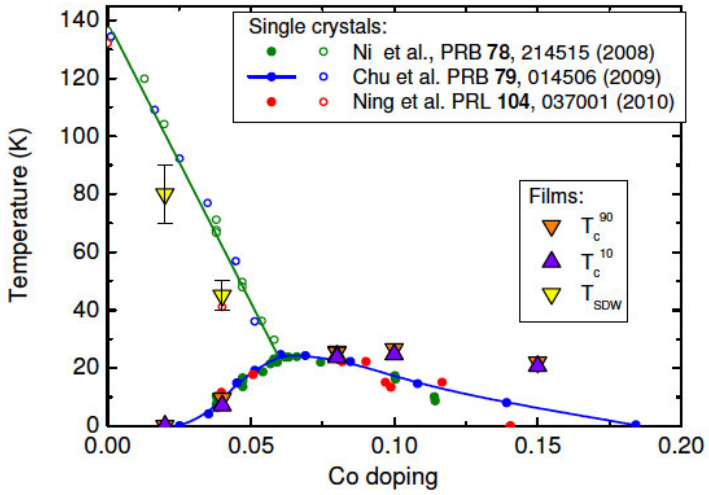

Figure 4.10: Critical temperatures (T_c^{10} and T_c^{90}) of the Co-doped Ba-122 thin films analysed as a function of doping, compared to that of single crystals. The wider superconducting "dome" observed in films may arise from a reduced Co content of the films with respect to the nominal one, and/or from lattice strain due to the CaF_2 substrate. It has been recently found [123] that the critical temperature of films grown with the same method on MgO perfectly agree with those of single crystals; this seems to indicate that the CaF_2 substrate has a predominant effect in the enhancement of T_c in these films.

As mentioned in the previous chapter, the resistance measurement is definitely not a local one; and also the critical temperature is averaged over a large portion of the film. To check whether this measurement is representative of the local properties, PCARS technique,

which is very seldom employed for that purpose, was used. Since the energy gap closes at the local critical temperature of the region where it is measured, PCARS can provide point-like measurements of the critical temperature, already defined as the temperature T_c^A at which the features associated to Andreev reflection disappear and the normal-state conductance is recovered. The experimental details on PCARS measurements will be described in the section 4.3, where the complete study of the energy gap by means of this technique is reported.
The comparison between the values of T_c^A measured in different regions of a given film (hollow symbols) with the relevant R vs T curve (red filled symbols) is shown in the main panel of Fig. 4.9. Here the abscissa of each hollow circle is the local T_c^A of a point-contact; since each PCARS spectrum must be acquired at thermal equilibrium, the uncertainty on T_c^A comes from the temperature step between the first normal-state spectrum and the last superconducting one. The ordinate of the points does not have a special meaning (it has been adjusted so that the points are superimposed to the R(T) curve for ease of comparison). Actually the values of the local T_c^A are close to T_c^{90} or lie between this temperature and T_c^{10} in all the thin films studied as shown in Fig. 4.11 where also two different part of the same 8% Co-content thin film are reported. The absence of T_c^A values that fall in the lower 10% of the resistive transition is an experimental evidence common to all the measured films. This fact certainly indicates that there is no significant heating in the contact region (i.e. the temperature of the contact is not higher than that of the bath), as instead would happen if the contacts were not in the proper spectroscopic regime.

4.2.1 Aging effect

Different regions of the film surface in the same pattern of current density were probed by using four-probe dc resistance measurements in collinear configuration fixed current source and drain contacts (placed on opposite corners of the films) and different sets of voltage contacts placed between them are reported in Fig. 4.12.
The consistency of the transition temperatures (T_c^{10}, T_c^{90}, T_c^0) is usually confirmed, as well as the homogeneity of the critical temperature over a millimeter scale. An example is shown in Fig. 4.12, where the critical temperatures of different 5 mm x 5 mm pieces cut from the same 1cm x 1cm film, each measured in two different configurations of voltage contacts are shown.
In particular, it turns out that the homogeneity of each part of the sample is very good. As in evidence in Fig. 4.12, the R vs T curve measured in the two contacts configurations (conf. A and conf. B) show the same values of T_c^{90} and T_c^{10}.
The homogeneity is also very good over different regions of the same 1 cm x 1 cm film as shown in Fig. 4.13. The R vs T curves of the three different pieces, measured with two different linear configurations of the V contacts and with the vdP configurations, show a spread in T_c^{90} that is only equal o 0.17 K, and a spread in T_c^{10} which is only slightly larger (0.25 K). This means that the films differ only in the width of the transition and not in its onset. Also aging effects (due to reaction with air/moisture) were analysed on the thin films by using resistance measurements because it gives rise to a decrease in the critical

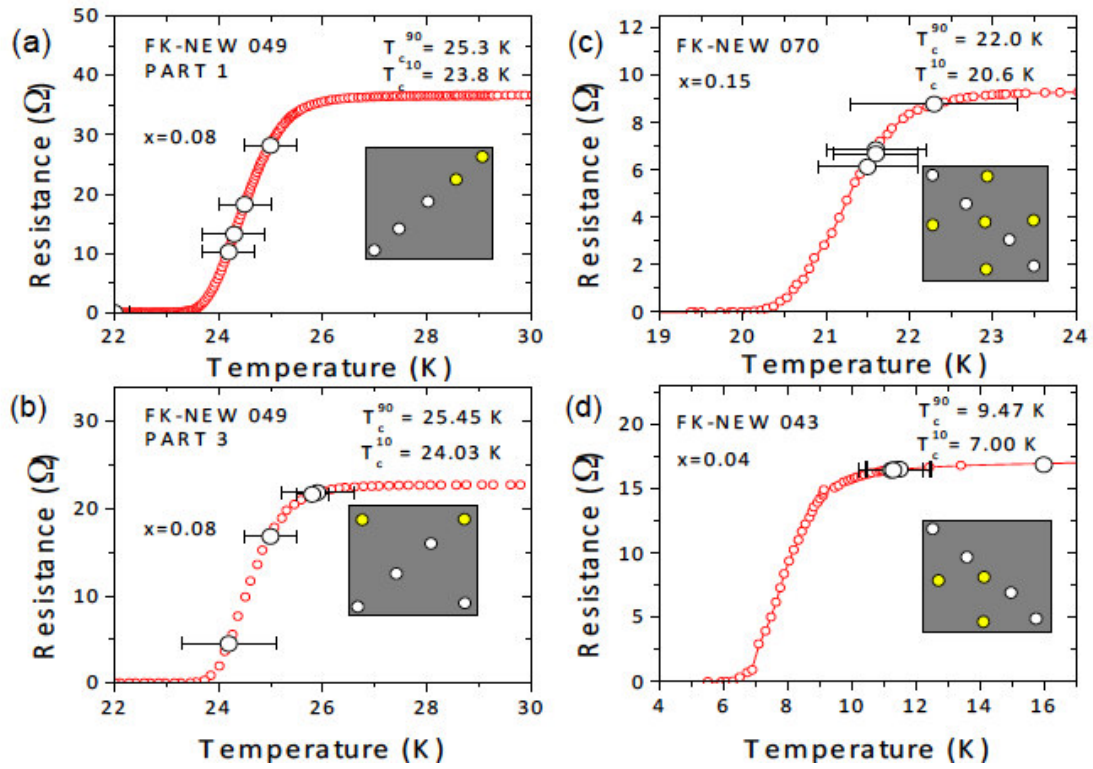

Figure 4.11: The local T_c^A values determined by PCARS (black points) compared with the R vs T curve (red points) in: a,b) two different 5 mm x 5 mm pieces of film FK-NEW 049 (8% Co-doped); c) film FK-NEW-070 (15% Co doped); d) film FK-NEW-043 (4% Co-doped). The inset shows schematically the surface of the film, with the contacts for resistance measurements (white dots) and the regions where the point-contact measurements were carried out (yellow dots). In some cases, e.g. in (a) and (b) they partially coincide. Note that in these graphs the horizontal coordinate of the black points represents the local T_c^A, while their vertical coordinate is arbitrary and has been chosen for convenience to coincide with the resistance of the film at that temperature.

temperature and to an increase of non homogenous results on thin films as shown in Fig. 4.14.

In this figure the resistance versus temperature curves obtained in Cobalt-doped Ba-122 thin film with two different linear configurations immediately after that they were kept aou of the vacuum and after one week of exposure to atmosphere and moisture.

The above means that a single resistance measurements with the vdP configurations (that probes a wider area of the surface than the collinear one) provides a good estimation of the critical temperature on the thin films, and that local variations in the critical temperatures are within the experimental uncertainty in both the linear and the vdP configuration measurements. Specific results of the measurements performed on different compounds will report in the follow chapters devoted to each compounds analysed in this work.

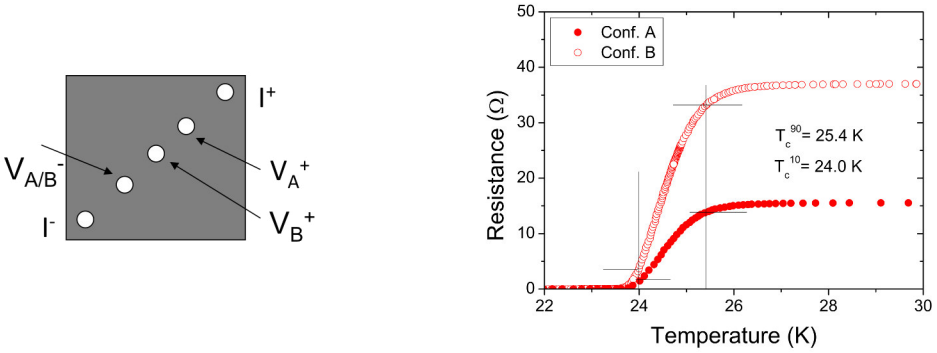

Figure 4.12: Schematic mounting of resistance measurements in two different collinear configurations is shown in the right panel. R vs T curves obtained in Co-doped Ba 122 thin films with the two contact configurations is shown in the left panel of figure.

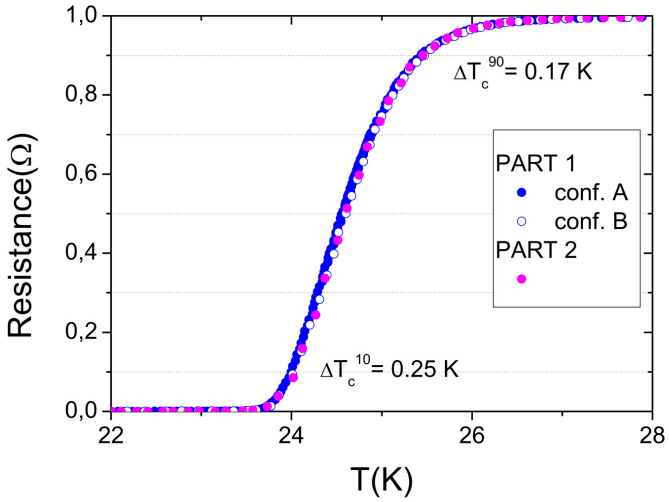

Figure 4.13: R vs T curves obtained in three parts of the same film in two collinear configurations (see PART1) and in vdP configuration (see PART2).

4.3 PCARS measurements: doping and critical temperature of the energy gaps

The dependence of the superconducting gaps in epitaxial $Ba(Fe_{1-x}Co_x)_2As_2$ thin films on the nominal doping x ($0.04 \leq x \leq 0.15$) was studied by means of point-contact Andreev-reflection spectroscopy.

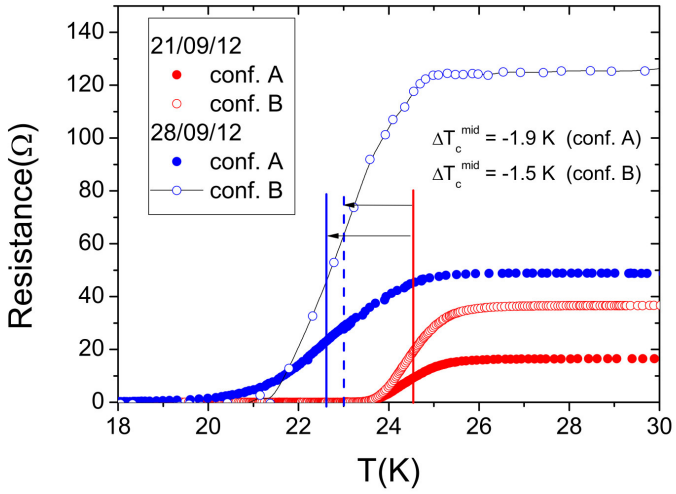

Figure 4.14: Aging effect on Cobalt-doped Ba-122 thin film.

4.3.1 Experimental details

PCARS measurements have been performed by using the "soft" technique (see section 3.3) in which a thin Au wire ($\varnothing = 18\mu$m) is kept in contact with the film surface by means of a small drop ($\varnothing \leq 100\mu$m) of Ag conducting paste. The effective size of the point contact (PC) is of course much smaller than the area covered by the Ag paste: Parallel nanoscopic contacts are likely to be formed here and there, between individual Ag grains and the sample surface. In the specific case of the Co-doped Ba-122 thin films analysed in this work, conventional point-contact measurements gave either featureless spectra, or spectra far from ideality, with a small Andreev signal superimposed to a background strongly decreasing with bias voltage [124] while the soft technique provides very often good spectra with a clear spectroscopic signal, as we will show in the following. Analyses of the surface of these films carried out by means of atomic force microscopy, x-ray photoemission spectroscopy, and scanning spreading resistance microscopy have provided an explanation for this different results [124]. They have shown the presence of a thin, inhomogeneous, poorly conducting layer, due to reaction with air, that makes the local conductivity of the surface highly position dependent. In these conditions, since the conventional technique probes a very small portion of the surface, the probability of making the contact in a clean region is rather low. In contrast, the drop of Ag paste used in the soft technique covers a larger surface and allows a natural selection of the more conducting channels within a micrometric region. It was also shown in section 4.2.1 that sample degradation can be sensibly reduced keeping the samples in inert atmosphere (and this is what was done with all the samples analysed in this work).
The PCARS spectra simply consist of the differential conductance dI/dV of the N-S contact, as a function of the voltage. In principle, a point contact can provide spectroscopic information only if the conduction is ballistic, i.e., electrons do not scatter in the contact

region (see section 3.3). The fact that in these films most of the contacts, irrespective of their resistance, do show clear Andreev signals is again related to the particular nature of the film surface and to the fact that each contact is actually the parallel of many nanoscopic contacts. As a matter of fact, the high residual resistivity ($120\,\mu\Omega$ cm for $x = 0.10$) of the films implies a small mean free path, reasonably of the order of a few nanometers (even though its precise determination from the resistivity is not straightforward and would at least require the calculation of the plasma frequencies of the different bands). In these conditions (as discussed in the case of PCARS on thin films of SmFeAs(O,F) and LaFeAs(O,F) [125]) the ballistic or, at least, the diffusive [64] regime can only be achieved when the (microscopic) PC is the parallel of several nanoscopic contacts that fulfill the ballistic or diffusive conditions, and whose individual resistance is thus much greater than that of the microscopic contact as a whole. This occurs rather naturally in our films thanks to the surface characteristics mentioned above.
Owing to the epitaxial structure of the films and to the smoothness of their surface, the current that flows through the point contact is mainly parallel to the crystallographic c-axis. By placing the contacts in different regions of the sample surface, we were able to check the homogeneity of the superconducting properties and to obtain some information about their distribution. To allow a comparison of the experimental dI/dV vs V curves to the theoretical models, the former must be first normalized, i.e., divided by the normal-state conductance curve $(dI/dV)_N$ vs V (in principle, recorded at the same temperature). This curve is inaccessible to experiments because of the very high upper critical field, and the normal-state conductance measured just above T_c is unusable because of an anomalous shift of the conductance curves across the superconducting transition, clearly visible in Fig. 4.15. This effect is typical of very thin films and is related to a temperature- and current-dependent spreading resistance contribution arising from the portion of the film between the point contact and the second voltage electrode [51].
A quantitative model has been recently proposed [68, 110]. For these reasons the normalization can be rather critical in Fe-based compounds; here it was chosen to divide the low-temperature conductance curves by a polynomial fit of their own high-voltage tails, as shown in the left inset of Fig. 4.15. For the same reason, the low-temperature spectra were studied here. The normalized curves were fitted with the 2D-BTK model (see section 3.3) in order to extract the gap values.
The local critical temperature (T_c^A) can be determined by simply looking at the temperature dependence of the raw conductance curves; T_c^A is identified with the temperature at which the features related to Andreev reflection disappear (see section 3.3), and its uncertainty is determined by the width of the temperature steps between the acquired spectra. T_c^A values are generally in very good agreement with the critical temperature of the whole film determined by resistance measurements as shown in the previous section since in most cases they fall between T_c^{10} and T_c^{90}. A noticeable exception is the underdoped sample ($x = 0.04$) in which some spectra show a zero-bias peak that becomes clearer on increasing temperature and persists in the normal state. This effect has also been observed by other groups [126, 127] and might be related to some magnetic scattering rather than to superconductivity. This issue is still under debate, and here only PCARS spectra that do not show this anomaly will be reported.

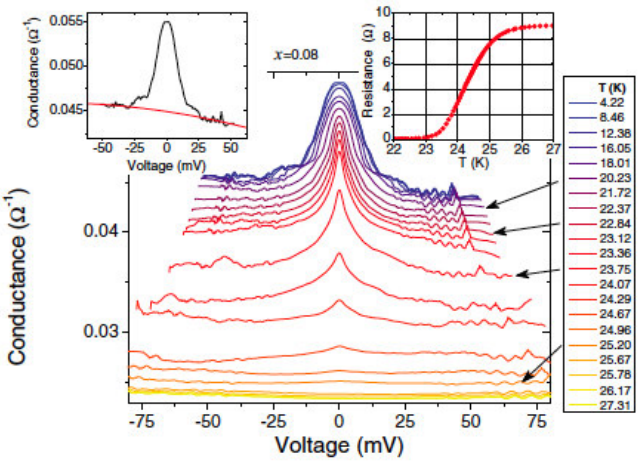

Figure 4.15: Temperature dependence of the spectrum of a point contact on an 8% Co-doped film, up to the critical temperature and above. The shift of the spectra is clearly seen. The left inset shows the low-temperature spectrum and the polynomial curve that fits its tails used for normalization. The right inset reports the temperature dependence of the resistance of the film. The shift of the spectra correlates with the onset of resistivity in the film. In this case, $T_c^A = 25.4 \pm 0.3$ K [35].

4.3.2 Results and discussion

Fig. 4.16 shows some representative examples of the many PCARS spectra recorded in films at different doping (symbols), from $x = 0.04$ (top panel) to $x = 0.15$ (bottom panel). For $x \geq 0.08$ the shape of all the curves is clearly incompatible with a single gap. These spectra show two symmetric maxima at low energy (or a small flat region around zero bias, as in the bottom panel) which are the hallmark of the small gap Δ_S, plus additional shoulders or changes in slope at higher energy that are due to the second, larger gap Δ_L. The case of $x = 0.04$, where the double-gap structure is not evident, is in some sense anomalous and will be discussed in more detail later. The additional structures often visible at higher energy (about 20 meV for $x \geq 0.08$) are related to the strong coupling between electrons and spin fluctuations [66, 68]. Here, these structures are disregarded as the main interest of this section is devoted to the gap amplitudes also because their presence does not affect in any way the values of the gaps extracted from the fit.
Solid lines superimposed to the experimental data of Fig. 4.16 represent their best fit within the two-band 2D-BTK model. The values of these parameters for the curves shown in Fig.4.16 are reported in Table 4.4. Because of the number of parameters, the set of their best-fitting values for a given spectrum is not univocal, especially when the signal is not very high as in Fe-based compounds.
Based on the results obtained in $Ba(Fe_{1-x}Co_x)As_2$ single crystals at optimal doping [66], the two gaps were initially assumed to be isotropic. This assumption works well in the whole doping range analyzed here, thus indicating that there are no clear signs of a change in the gap symmetry and structure on increasing the doping content. In this respect it should be noted that the 2D-BTK model is not the most sensitive to the subtle details of

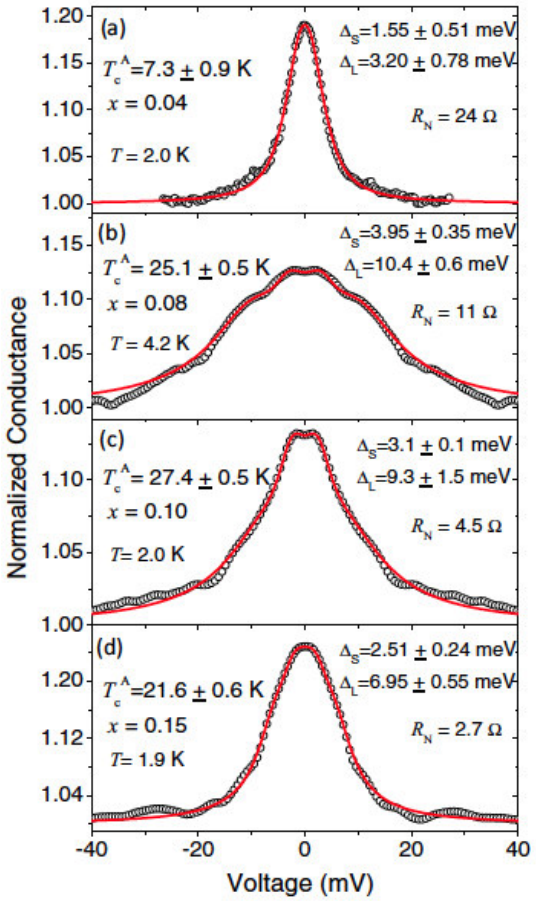

Figure 4.16: Low-temperature normalized PCARS spectra (symbols) in films with different Co content: $x = 0.04$ (a), $x = 0.08$ (b), $x = 0.10$ (c), and $x = 0.15$ (d), together with their two-band 2D-BTK fit (lines). The corresponding fitting parameters are listed in Table 4.4. The gap values Δ_S and Δ_L indicated in the panels are instead the average over different possible fits of the same curve, as explained in the text. The normal-state resistance of the contacts is also indicated, as well as the local critical temperature T_c^A.

x	Δ_S (meV)	Γ_S	Z_S	Δ_L (meV)	Γ_L	Z_L	W_S	$2\Delta_S/k_BT_c^2$	$2\Delta_L/k_BT_c^2$
0.04	1.80	1.52	0.16	3.6	2.59	0.17	0.48	5.73 ± 0.71	11.47 ± 1.41
0.08	3.90	2.70	0.23	10.60	7.00	0.39	0.40	3.61 ± 0.07	9.82 ± 0.20
0.10	3.20	2.40	0.25	8.80	7.30	0.32	0.50	2.72 ± 0.05	7.47 ± 0.14
0.15	2.75	2.03	0.20	7.00	2.90	0.20	0.50	2.96 ± 0.08	7.54 ± 0.21

Table 4.4: Fitting parameters of the spectra shown in Fig. 4.16 where each set of parameters is relevant to the individual BTK curve shown in the corresponding panel. The gaps Δ_S and Δ_L and the broadening parameters Γ_S and Γ_L are expressed in meV. The uncertainty on the gap ratio is due to the uncertainty on the critical temperature.

the gap structure, so this result does not exclude gap anisotropies either in the plane or in the c direction whose existence has been claimed or predicted in Co-doped Ba-122 [11] and

more generally in the 122 systems [77, 128]. It must be noted, however, that if extended node lines (predicted in particular conditions in 122 compounds [44]) were present, they would give rise to quasiparticle excitations with very small energy that can be detected by PCARS, as shown in the case of $Ca(Fe,Co)_2As_2$ [36].
Fig. 4.17 shows two examples of the many (almost 20) conductance curves measured in three different films with $x = 0.08$. The curves have different shapes but the values of the gaps extracted from their fit (indicated in the legend) are compatible with one another. The other fitting parameters are listed in the caption. As shown in panel (c) of the same figure, there is no correlation between the gap values extracted from the fit of different spectra and the resistance of the contact. This fact supports the spectroscopic nature of the contacts [125] and excludes the presence of spreading-resistance effects [51] in the measurements presented in this work at low temperature. More generally, the consistency of the gap values obtained in different regions of the same film is good proof of the macroscopic homogeneity of the superconducting properties, while the consistency of the values obtained in different films with the same doping is proof of the reproducibility of the deposition process.
For $x = 0.04$ the spectra often show very clear shoulders at energies of the order of 7 meV in addition to conductance maxima at about 3 meV, as shown in Fig. 4.18. The shoulders are fast suppressed on increasing temperature or upon application of a magnetic field (they look completely washed out already at 5 K, or in a field of 1 T). If one assumes that they are due to a superconducting gap and fits the spectra with the two-band 2D-BTK model, the relevant amplitude Δ^* turns out to be of the order of 6-9 meV. Since the measured film showed a T_c^{90} of less than 10 K, these values are clearly unphysical for a superconducting gap. The smaller gap obtained from the same 2D-BTK fit turns out to range between 1.1 and 3.2 meV and its Andreev signal shows a conventional dependence on temperature and magnetic field. In a small number of spectra, of which an example is shown in Fig. 4.18b the structures at about 7 meV are not present at all and a single, much narrower structure is observed, whose width is of the order of 3 meV. These spectra admit a fit with the single-gap BTK model, giving a gap of the order of 2 meV, but the two-band BTK model still works better [see the inset to Fig. 4.18(b)] and gives a small gap Δ_S of the order of 1.5 meV and a larger gap Δ_L of about 2.5-3.0 meV. Although this fact alone does not allow concluding that in this compound two gaps survive, we will refer from now on to the results of the two-gap fit on the basis of plausibility arguments. Indeed, even at 4% Co doping, the Ba-122 system retains a multiband electronic structure and there is no reason to believe that the two gaps observed at higher doping should "merge" into one. This effect is theoretically predicted in the presence of strong disorder [129] but would be accompanied by a strong suppression of the critical temperature, while the T_c of our 4% Co-doped film is identical to that of single crystals with the same Co content, where two gaps have been measured by specific heat [130].
Fig. 4.18(c) shows a summary of the values of Δ_S, Δ_L, and Δ^* obtained from the two-band fit of spectra of the first and second type, plotted as a function of the resistance of the contacts R_N. Clearly, the larger "energy scale" Δ^* depends on the contact resistance, which (together with the anomalous dependence on temperature and magnetic field) indicates that the structures around 7 meV are not due to a superconducting gap. Further

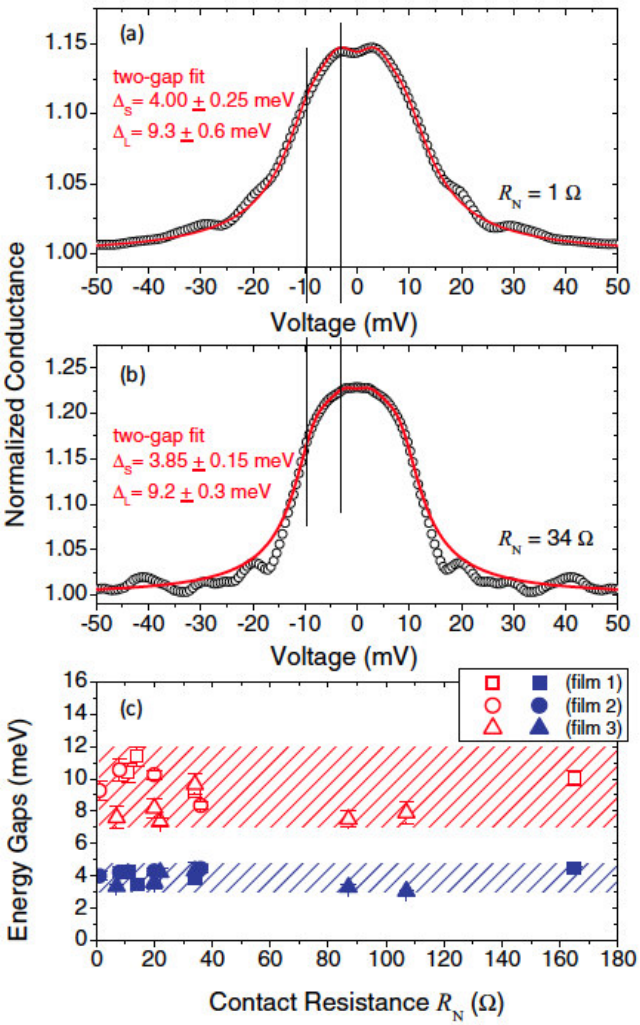

Figure 4.17: (a), (b) Two examples of PCARS spectra taken in different films of $Ba(Fe_{0.92}Co_{0.08})_2As_2$. Despite the different shape of the spectra, the gap values obtained from the fit are consistent. The fit shown in (a) was obtained with $\Delta_S = 4.25$ meV, $\Gamma_S = 3.60$ meV, $Z_S = 0.25$, $\Delta_L = 9.90$ meV, $\Gamma_L = 4.70$ meV, $Z_L = 0.34$, $w_L = 0.60$. The fit in (b) was obtained with $\Delta_S = 3.70$ meV, $\Gamma_S = 2.35$ meV, $Z_S = 0.18$, L = 9.00 meV, $\Delta_L = 3.25$ meV, $Z_L = 0.30$, $w_L = 0.40$. (c) Gap amplitudes as a function of the resistance of the contacts, which shows the absence of any correlation between these quantities and demonstrates the spectroscopic nature of the contacts. This panel includes data taken in three different films.

confirmation comes from the weight of Δ^* in the fit, which depends on R_N (unlike for superconducting gaps), decreasing from 0.8 to 0.6 when R_N goes from 58 Ω to 17 Ω. This reflects the fact that the amplitude of the relevant structures decreases on decreasing R_N; consequently, their position is less easily identifiable (which may partly account for the dependence of Δ^* from R_N). On this basis, understanding the origin of these structures is a difficult task. The 4% doped sample falls well in the region of the phase diagram where superconductivity and magnetism coexist, and which is still poorly understood. One might

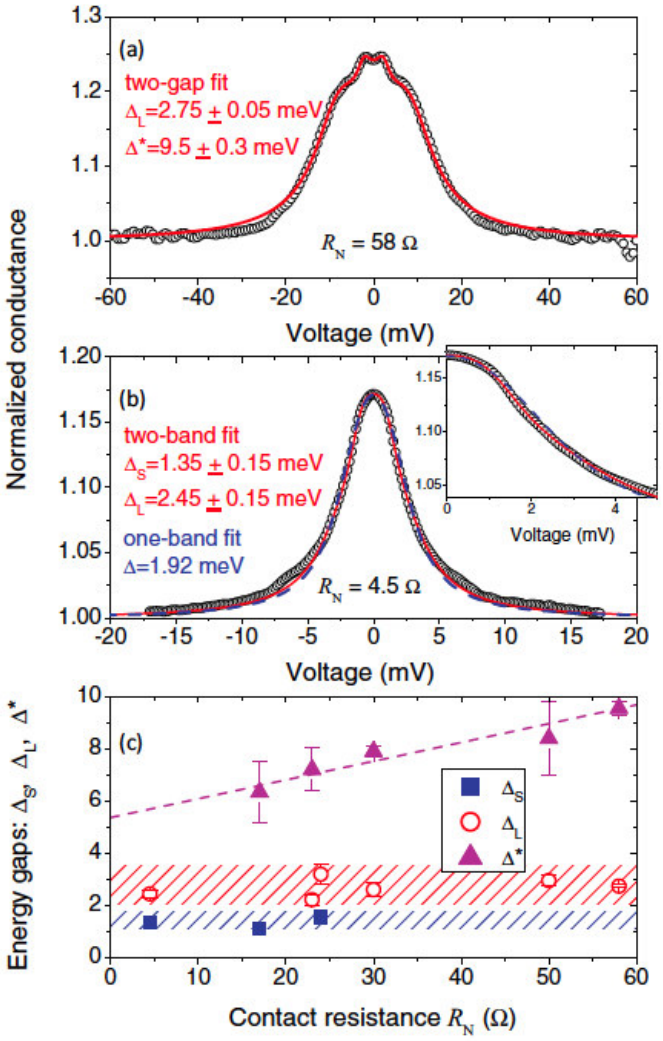

Figure 4.18: (a), (b) Two examples of PCARS spectra taken in different points of the same film (5 x 5 mm^2) of $Ba(Fe_{0.96}Co_{0.04})_2As_2$. The spectrum in (a) shows clear shoulders around 7 meV and conductance maxima at lower energy. The solid line represents the best fit of the curve obtained within the 2D-BTK model assuming that the shoulders are due to a superconducting gap Δ^*. The fitting parameters are $\Delta_L = 2.8$ meV, $\Gamma_L = 1.15$ meV, $Z_L = 0.24$, $\Delta^* = 9.8$ meV, $\Gamma^* = 4.75$ meV, $Z^* = 0.25$, $w_S = 0.2$. The spectrum in (b) instead does not show shoulders but a single maximum at zero bias, and the FWHM of the whole structure is of the order of 3 meV. The solid line is the two-band BTK fit, obtained with parameters $\Delta_S = 1.35$ meV, $\Gamma_S = 0.84$ meV, $Z_s = 0.18$, $\Delta_L = 2.6$ meV, $\Gamma_L = 1.8$ meV, $Z_L = 0.4$, $w_S = 0.6$. The dashed line is the single-band BTK fit, obtained with parameters $\Delta = 1.92$ meV, $\Gamma = 1.74$ meV, $Z = 0.12$. A magnification of the low-energy region (inset) shows that the two-gap fit is better. (c) Amplitudes of the "gap" Δ and of the gaps Δ_S and Δ_L as a function of the contact resistance R_N.

speculate that these structures arise from a magnetic phase probed by a subset of nanocontacts; the amplitude of the relevant signal in the spectrum, as well as the resistance of the contact as a whole, may thus be related to the fraction of conduction channels in this

phase.
Going back to Fig. 4.18(c), the smaller gaps do not show any dependence on the contact resistance and seem to cluster in two groups indicated by squares and circles for clarity. Although the two energy ranges are very close to each other, they do not overlap (even taking into account the error bars), further supporting the picture of two gaps Δ_S and Δ_L. Fig. 4.19 reports the (average) gap amplitudes Δ_S and Δ_L obtained in the various films as a function of the T_c^A (average) of the contacts. In other words, the values of Δ_S and Δ_L reported here are the midpoints of the corresponding range of gap amplitudes obtained in the fit of different curves. The width of the range is represented by the vertical error bars, while the horizontal error bars indicate the range of T_c^A values in all the point contacts made on that film.

In Fig. 4.19 also the results of PCARS in single crystals [66, 126, 136] are reported as

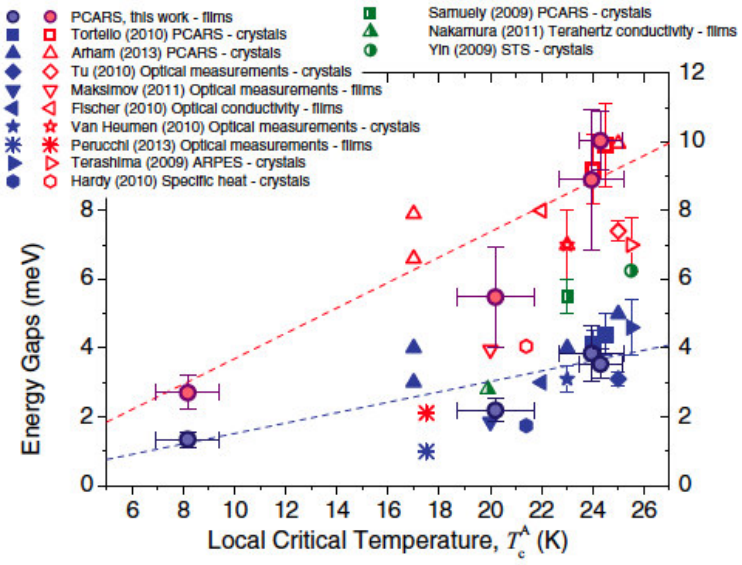

Figure 4.19: Average gap amplitudes in $Ba(Fe_{1-x}Co_x)_2As_2$thin films with different Co content obtained by PCARS measurements (filled circles), plotted as a function of T_c^A. The other data points are taken from literature, and specifically squares from Ref.[66], up triangles from Ref.[126], diamonds from Ref.[131], down triangles from Ref.[132], left triangles from Ref.[133], stars from Ref.[134], asterisks from Ref.[135], right triangles from Ref.[26], hexagons from Ref.[130], half-filled squares from Ref.[136], half-filled circles from Ref.[137], and half-filled triangles from Ref.[138]. The techniques used for these measurements are indicated in the legend. The upper and lower dashed lines correspond to a gap ratio $2\Delta/k_BT_c$ equal to 3.52 and 9.0, respectively.

well as the gap amplitudes determined either in films or single crystals by means of other techniques, namely, optical measurements [131, 132, 133, 137], specific heat [130], angle-resolved photoemission spectroscopy (ARPES) [26] and scanning tunnelling spectroscopy [138].
At the highest T_c values, corresponding to $x = 0.08$ and $x = 0.10$, the gap values agree rather well with those given by PCARS in single crystals [66, 126]. The large spread of Δ_L values given by PCARS has already been noticed in various Fe-based compounds [68] and

its origin may be either intrinsic (e.g., anisotropy of Δ_L) or extrinsic (uncertainty due to the normalization). Finally, the values given by PCARS (especially for Δ_L) are systematically larger than those given by optical measurements and specific-heat measurements. This may be due to the approximations on which the fit of the curves is based, but may also hide some more fundamental property of Fe-based compounds. The small gap Δ_S appears much better defined; the values provided by different techniques are well consistent with one another. Concerning the gap values away from optimal doping, it should be borne in mind that Fig. 4.19 reports in the same plot the data for underdoped and overdoped samples; in particular, the points at $T_c = 20.2$ K refer to the $x = 0.15$ thin film. If these points are temporarily excluded from the analysis, a roughly linear trend of the gaps as a function of T_c can be observed. The dashed lines in Fig. 4.19 have equations $2\Delta/k_BT_c = 3.52$ and $2\Delta/k_BT_c = 9.0$; it can be clearly seen that the small gap is approximately BCS for any x between 0.04 and 0.10. Even though Δ_L is affected by a much larger uncertainty, it can be said that $2\Delta_L/k_BT_c$ ranges between 7 and 10 in the same doping range. The points at $x = 0.15$ are instead outside this trend since the gap values here correspond to reduced gap ratios. This point can be clarified by plotting the gap amplitudes as a function of the nominal doping, as in Fig. 4.20.

As expected, the trend of the gaps mimics the trend of the critical temperature, showing

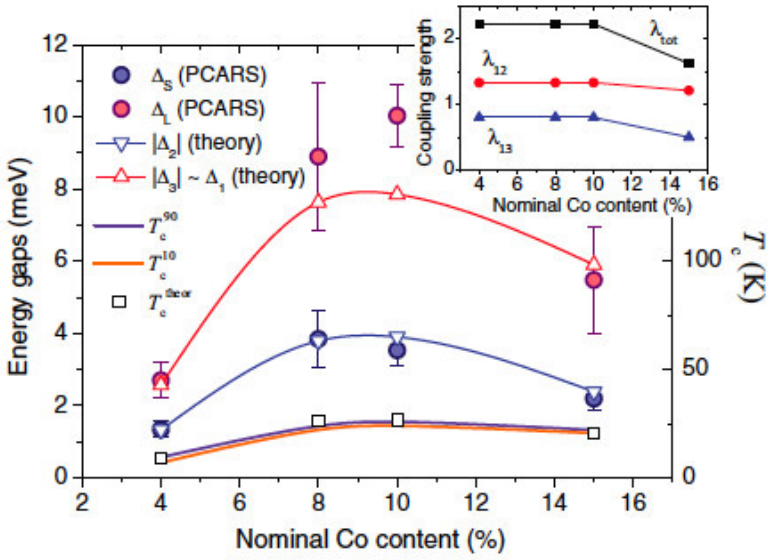

Figure 4.20: Doping dependence of the gaps measured by PCARS (circles, left vertical scale) and of the critical temperature from resistivity measurements (lines, right vertical scale). Triangles and squares indicate the values of the gaps and of the critical temperature calculated within the three-band Eliashberg model. The inset shows the dependence of the coupling strengths λ_{12} and λ_{13} on the Co content, together with the total electron-boson coupling constant.

a maximum at $x = 0.08 - 0.10$. However, the trend is not symmetric in the sense that in the overdoped region the gaps decrease "more" than the critical temperature, i.e., the gap ratios decrease. The theoretical analysis of these results is presented in the following

section.

4.3.3 PCARS measurements within the Eliashberg theory

The three-band Eliashberg model with a very small number of free parameters was already demonstrated [59, 69] to be a strong tool for the study of the phenomenology of Fe-based superconductors and allows explaining a large variety of their properties. Here the same model was used to try to rationalize the experimental trend of the gaps as a function of T_c or of the doping content x. The first assumption of the model is that the electronic structure of $Ba(Fe_{1-x}Co_x)_2As_2$ can be approximately described by one hole band (indicated in the following as band 1) and two electron bands (2 and 3)[66, 69]. The gap symmetry is assumed to be $s\pm$ [28] so that the sign of Δ_1 (here assumed positive) is opposite to that of Δ_2 and Δ_3. Although PCARS, as well as many other spectroscopic techniques, provides at most two gap amplitudes and does not allow associating them to a particular FS sheet, the use of (at least) three effective bands and thus three gaps is necessary for the Eliashberg model to be able to reproduce the experimental results. However, ARPES results in optimally Co-doped Ba-122 single crystals indicated that the larger gap belongs to the holelike FS sheet [26]. With this in mind, it was assumed $\Delta_1 \simeq |\Delta_3|$ and $|\Delta_2|$ to be the large and the small gaps measured by PCARS, respectively. This assumption is consistent with the fact that the experimental results do not resolve the two larger gaps. To obtain the gaps and the critical temperature within the $s\pm$ wave three-band Eliashberg model [139] one has to solve six coupled equations for the gaps $\Delta_i(i\omega_n)$ and the renormalization functions $Z_i(i\omega_n)$, where i is a band index ($i = 1.3$). The equations have been reported elsewhere [59] their solution requires a large number of input parameters (18 functions and 9 constants); however, some of these parameters are correlated, some can be extracted from experiments, and some can be fixed by suitable approximations. For example, the coupling constant matrix λ_{ij} can be greatly simplified. In general, one should consider that each matrix element has one contribution from phonons and one from antiferromagnetic (AFM) spin fluctuations (SF), i.e. $\lambda_{ij} = \lambda_{ij}^{ph} + \lambda_{ij}^{sf}$. However, the coupling between the two electron bands is small, and we thus take $\lambda_{23} = \lambda_{32} = 0$; the total electron-phonon coupling in pnictides is generally small [70] and phonons mainly provide intraband coupling, so that we assume $\lambda_{ij}^{ph} = 0$; spin fluctuations mainly provide interband coupling between the two quasi-nested FS sheets [28], and thus it was assumed $\lambda_{ij}^{sf} = 0$. Finally, the electron-boson coupling-constant matrix λ_{ij} takes the following form [12, 59, 66]:

$$\lambda_{ij} = \begin{pmatrix} \lambda_{11}^{ph} & \lambda_{12}^{sf} & \lambda_{13}^{sf} \\ \lambda_{21}^{sf} & \lambda_{22}^{ph} & 0 \\ \lambda_{31}^{sf} & 0 & \lambda_{33}^{ph} \end{pmatrix}$$

where $\lambda_{21}^{sf} = \lambda_{12}^{sf}\nu_{12}$ and $\lambda_{31}^{sf} = \lambda_{13}^{sf}\nu_{13}$, with $\nu_{ij} = N_i(0)/N_j(0)$ and $N_i(0)$ is the normal density of states at the Fermi level for the ith band. Another fundamental ingredient is the electron-boson spectral function $\alpha^2F(\Omega)$ of the boson responsible for the pairing. The shape of the electron-phonon spectral function is taken from literature [71] and we assume $\alpha_{11}^2F^{ph}(\Omega) = \alpha_{22}^2F^{ph}(\Omega) = \alpha_{33}^2F^{ph}(\Omega)$ with $\lambda_{ii}^{ph} = 0.2$ [72]. As for spin fluctuations, we

assume their spectrum to have a Lorentzian shape [59, 69]:

$$\alpha^2_{ij}F^{sf}(\Omega) = C_{ij}\{L(\Omega+\Omega_{ij},Y_{ij}) - L(\Omega-\Omega_{ij},Y_{ij})\}, \tag{4.1}$$

where $L(\Omega\pm\Omega_{ij},Y_{ij}) = \frac{1}{(\Omega\pm\Omega_{ij})^2+Y_{ij}}$. C_{ij} are normalization constants, necessary to obtain the proper values of λ_{ij} while Ω_{ij} and Y_{ij} are the peak energies and half-widths of the Lorentzian functions, respectively [59]. In all the calculations it was set $\Omega_{ij} = \Omega_0^{sf}$ and $Y_{ij} = Y_{ij}^{sf} = \Omega^{sf}/2$ [76]. Here, Ω_0^{sf} is the characteristic energy of the AFM SF, assumed to be equal to the spin-resonance energy, as verified experimentally by us in optimally Co-doped Ba-122 single crystals [66, 68]. Its value is determined according to the empirical relation $\Omega_0^{sf} = 4.65k_BT_c$ (proposed in Ref. [5]). Band-structure calculations provide information about the factors ν_{ij} that enter the definition of λ_{ij}. In the case of optimally doped $Ba(Fe_{1-x}Co_x)_2As_2$, $\nu_{12} = 1.12$ and $\nu_{13} = 4.50$ [140]. As a first approximation, these values have been used here for all Co contents. Moreover, based on the fact that the Coulomb pseudopotential is probably small in these compounds [77] we assume all the elements of the pseudopotential matrix to be identically zero ($\mu^*_{ii} = \mu^*_{ij} = 0$): finally, the effect of disorder was neglected, owing to the high quality of the films.
Finally, only two free parameters remain, i.e., the coupling constants λ_{12}^{sf} and λ_{13}^{sf}. These parameters can be tuned in such a way to reproduce the experimental values of the small gap Δ_S and of the critical temperature, which are the best-defined experimental data; the values of the large gap Δ_L are indeed affected by a larger relative uncertainty, and moreover they might actually be a sort of weighted ńńaverage" of the two gaps Δ_1 and $|\Delta_3|$. The larger gaps are therefore calculated with the values of λ_{12}^{sf} and λ_{12}^{sf} that allow reproducing Δ_S and T_c.
The result of these calculations is that (i) the trend of the experimental gaps Δ_S and Δ_L as a function of T_c and of x in the samples with nominal Co content $x = 0.04, 0.08$, and $x = 0.10$ can be reproduced by using $\lambda_{12}^{sf} = 0.8$ and $\lambda_{13}^{sf} = 1.33$, and only changing the value of the characteristic SF energy Ω_0 according to the change in T_c; (ii) to reproduce the values of the gaps and of T_c in the overdoped sample ($x = 0.15$) it is instead also necessary to reduce the values of the two coupling constants: $\lambda_{12}^{sf} = 0.5$ and $\lambda_{12}^{sf} = 1.21$. The values of these two parameters are shown as a function of x in the inset of Fig. 4.20. Note that the total coupling is $\lambda_{tot} = 2.22$ for $x = 0.04, 0.08$, and $x = 0.10$ and decreases to $\lambda_{tot} = 1.82$ at $x = 0.15$. These values are in agreement with those found in literature [69, 72] and indicate that Co-doped Ba-122 is a strongcoupling superconductor at all the doping contents analyzed here. The main panel of Fig. 4.20 also reports the calculated values of the gaps as a function of x. The agreement between the theoretical and experimental values of T_c and of the small gap is very good; the large gap is underestimated around optimal doping, but the trend is qualitatively correct. The agreement might be improved if the feedback effect of the condensate on the bosonic excitations [74, 75] was taken into account, which was not done in this work for simplicity.

Study of the surface homogeneity by means of PCARS

The determination of the local gap values is not a standard surface characterization technique for thin films; however, the homogeneity of the gap amplitude over the surface is a

useful indication if the films are meant to be used for electronic applications (especially in the long-term purpose of realizing circuits with multiple Josephson junctions, large-area SQUIDs and so on). Therefore the application of the Point-contact Andreev reflection spectroscopy for this purpose is here discussed briefly, after the discussion of the traditional application of this technique.
For example, the values of the gaps determined by means of PCARS in the same point contacts used for the measurement of the local T_c^A (see left inset to Fig. 4.9). Fig. 4.21a shows two of the normalized PCARS spectra measured at 4.2 K on one of the 8% Co-doped Ba122 thin films.
Fig. 4.21b reports the values of the gaps obtained in different point contacts. The values

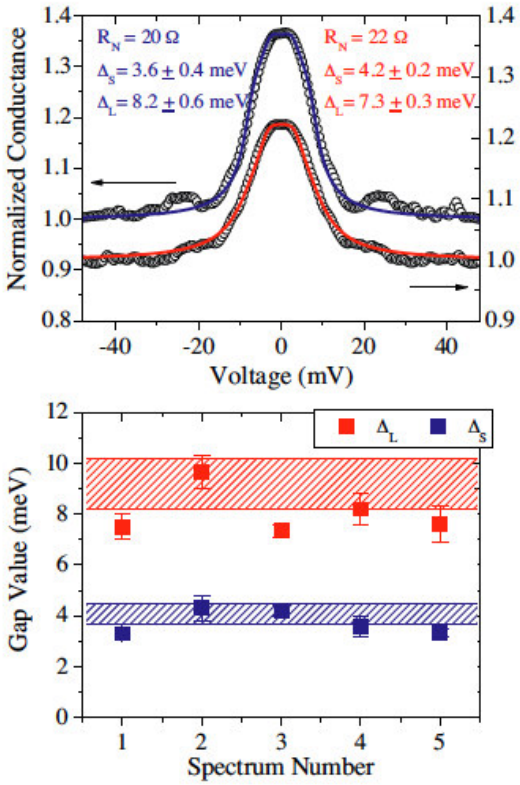

Figure 4.21: Examples of PCARS results on a Co-doped Ba-122 thin film. (a) Two examplesof normalized PCARS spectra measured in different points of the same 8% Co-dopedfilm (symbols) with the relevant 2D BTK fit (lines). The values of the gap amplitudes Δ_L and Δ_S are indicated in the labels. (b) Summary of gap values obtained in differentspectra in the same film (squares). The horizontal dashed bands represent the range of gap values found in single crystals with the same doping content [33].

are rather well compatible with one another; in particular, a good homogeneity of the small gap is observed, while the large gap shows greater spread: it varies within a range of about 3 meV including the error bars (this spread is however not unusual in Fe-based compounds [2]). Note that, as discussed in the previous section, the gap amplitudes show

no dependence on the contact resistance, that here varies by over one order of magnitude. The values of the gaps obtained in these films may be compared to those obtained in single crystals. In general, this comparison can tell whether the superconducting properties of the bulk are weakened in thin films. Here, because of the strong effect of the substrate, thin films are structurally different from the bulk material so that this comparison must be taken more cautiously. Anyway, just for the sake of discussion, the gap values measured in c-axis contacts in single crystals with critical temperature (measured by transport) $T_c^{onset} = 24.5$ K turned out to be $\Delta_S = 4.1 \pm 0.4$ meV and $\Delta_L = 9.2 \pm 1.0$ meV [66].
These ranges are indicated in Fig. 4.21 by dashed bands. It is clear that the values of Δ_S and Δ_L obtained in crystals lie well within the range of measured amplitudes in films, although in the latter case the spread is larger for both the small and the large gap. Itis also true, however, that single crystals were much smaller than the films (the top surface area was at most 1 x 1 mm^2) and that an extensive study of the spatial homogeneity of the gaps in these samples was not performed.

4.4 PCARS on Ba-122 thin films within the 3D-BTK model

Before the conclusions of this study of the $Ba(Fe,Co)_2As_2$ thin films, some results about the anisotropy of the pairing wavefunction or on the number, amplitude and symmetry of the energy gaps will be discussed. Moreover, it will be shown how the analysis of PCARS results within a suitable 3D generalization of the BTK model allowed obtaining qualitative information about the topology of the Fermi surface in 8% Co-doped Ba122 thin film on two different substrate. The epitaxial thin films growth on CaF_2 and on on MgO substrate with Fe buffer layer were described in section 4.1.1.

4.4.1 Calculation of the Fermi Surface

The FS of $Ba(Fe_{1-x}Co_x)_2As_2$ at $x = 0.08$ was calculated by using the lattice constants $a = b = 3.9625$ Å and $c = 13.0168$ Å as in Ref. [141], within the density-functional theory (DFT) by using the Elk FP-LAPW Code (http://elk.sourceforge.net/) and the GGA approach for the exchange correlation potential [142]. A virtual-crystal approximation was used in order to take into account the partial substitution of Fe with Co [143]. The choice of the doping content is based on the fact that the PCARS measurements here discussed were carried out on $Ba(Fe_{1.92}Co_{0.08})_2As_2$. The Fermi surface calculated as here described are shown in Fig. 4.22a.
The Fermi surface features two hole-like sheets around the $\Gamma - Z$ direction - both having the shape of warped cylinders, although the warping of the outer one is much more marked - and two electron-like warped cylinders with the characteristic 'elliptical" cross-section that depends on k_z.

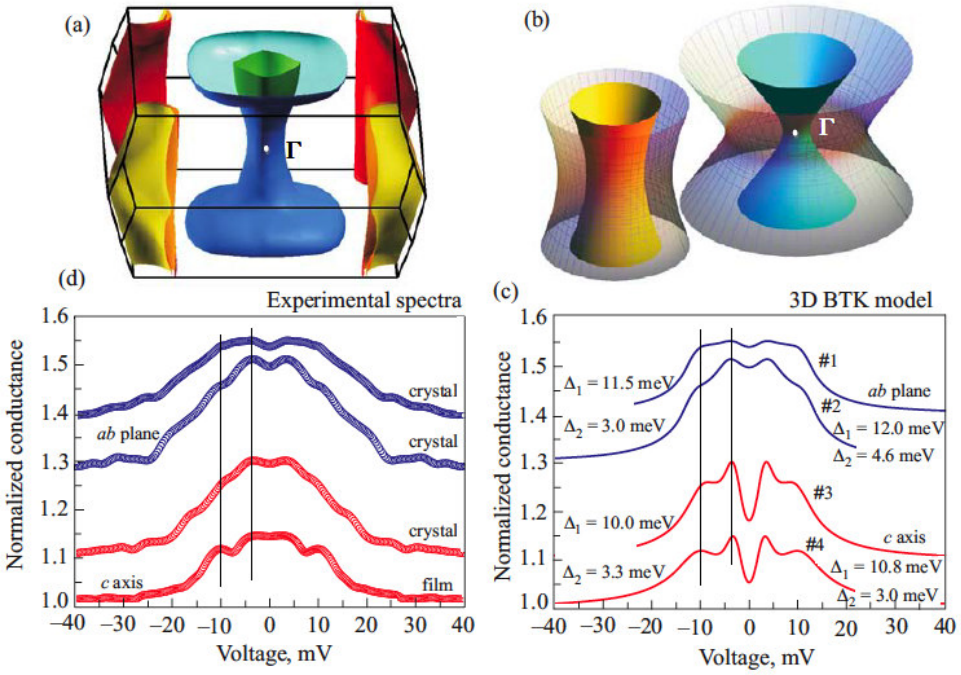

Figure 4.22: (a) Fermi surface of $Ba(Fe_{1.92}Co_{0.08})_2As_2$, with the strongly warped hole-like FS sheets around Γ and the electron-like FS sheets at the corners of the Brillouin zone. (b) The model Fermi surface used in the 3D BTK model. Matt surfaces are the Fermi surface sheets, while the gridded surfaces indicate the amplitude of the relevant gap. The drawing refers to the case of isotropic gaps on both the bands. (c) Theoretical curves calculated for I || ab (1 and 2) and I || c (3 and 4) and using the Fermi surface of panel (b). The gap amplitudes indicated in the labels were chosen in order to fit the position of the gap features in the experimental curves of panel (d). The other fitting parameters are the following: for curve 1, $\Gamma_1 = 1.85$ meV, $Z_1 = 0.03$, $\Gamma_2 = 3.6$ meV, $Z_2 = 0.31$; for curve 2, $\Gamma_1 = 1.75$ meV, $Z_1 = 0.08$, $\Gamma_2 = 3.0$ meV, $Z_2 = 0.245$; for curve 3, $\Gamma_1 = 2.8$ meV, $Z_1 = 0.05$, $\Gamma_2 = 1.3$ meV, $Z_2 = 0$; for curve 4, $\Gamma_1 = 3.85$ meV, $Z_1 = 0.1$, $\Gamma_2 = 1.4$ meV, $Z_2 = 0$. (d) Some examples of the experimental curves measured in 8% Co-doped $BaFe_2As_2$ with I || ab (top) and I || c (bottom). The lowest-lying curve was measured in the epitaxial films with x = 0.08 and $T_c = (23.8 \pm 0.7)$ K (see section 4.1.1), the others in single crystals [142].

4.4.2 3D-BTK model on Ba122 thin films PCARS spectra

Fig. 4.22b shows the shape of the FS that was chosen for the calculation of the PCARS spectra within the 3D BTK model. It is simply made up of two hyperboloids of revolution, one for the outer hole-like FS sheet (the inner one is neglected) and one for the two electron-like sheets. The problem now arises of which symmetry of the order parameter one should assume to calculate the PCARS spectra.
A number of experimental results reported in literature indicate for $Ba(Fe_{1-x}Co_x)_2As_2$ two isotropic gaps. The first directional PCARS measurements in single crystals ($x = 0.07$, $T_c = 23$ K) [144] that were carried out in the needle-anvil configuration and with the current along the c axis, showed clear Andreev signals but no evidence of multiple gaps and were fitted by a single- gap, s-wave 2D BTK model. Our directional PCARS measurements

in nominally 10% Co-doped Ba122 single crystals with $T_c = 24.5$ K [66] gave spectra with clear two-band structures in either the I || ab and I || c configurations. These spectra were successfully fitted by using a two-band 2D BTK model with two isotropic gaps, as the PCARS spectra in the previous section.
On the other hand, indications in favor of a complicated 3D structure of the gap (at least on the hole-like FS) with lines of zeros or deep minima were provided by directional thermal conductivity [50] and Raman spectroscopy [49] measurements; this possibility has been shown theoretically to be compatible with the general $s\pm$ symmetry [11].
Considering these suggestions, the theoretical PCARS spectra within the 3D BTK model by assuming two isotropic gaps, Δ_1 on the hole-like FS and Δ_2 on the electron-like FS were calculated, in order to verify whether this assumption allows reproducing the experimental data, in particular the representative spectra reported in Fig. 4.22d.
The first three spectra were measured in single crystals of $Ba(Fe_{1-x}Co_x)_2As_2$ with nominal $x = 0.1$, bulk $T_c^{on} = 24.5$ K and $\delta T_c = 1$ K [66], with the current parallel to the ab plane (first two curves) and to the c axis (third curve). All of them feature multiple structures that can be interpreted as being due to two distinct gaps and to the strong coupling of electrons to spin fluctuations whose characteristic energy Ω is around 12 meV (the relevant structure occurring at about $\Delta_1 + \Omega$ if Δ_1 is the large gap). The bottom curve of Fig. 4.22d was measured in epitaxial thin films (having the c axis normal to the surface) with $x = 0.08$ and $T_c = (23.8 \pm 0.7)$ K grown on a MgO substrate, with a Fe buffer layer. The multigap structures in this curve are even clearer than in single crystals; as shown by the vertical lines, the position of the gap features is the same for all the curves, which is a good indication of consistency. By using the 3D BTK model and the FS of panel (b), the experimental curves of panel (d) were fit. To do so, all the parameters (including the gap amplitudes) were taken as being adjustable, rather than fixing the values of the gaps as it was done for other compounds [142].
Fig. 4.22c reports the theoretical curves that best fit the experimental ones of panel (d). The gap amplitudes are reported in the legend, the other parameters in the caption. It is interesting to note that: i) the fit is generally capable of reproducing the position of the gap-related structures by using consistent values of the gaps, i.e., $\Delta_1 = (11.0 \pm 1.0)$ meV and $\Delta_2 = (3.8 \pm 0.8)$ meV; ii) the fit in the region eV$> \Delta_1$ works well in thin films, but fails in single crystals where large electron-boson coupling structures dominate the spectrum above 15 meV. This is actually obvious since the electron-boson structures cannot be reproduced by a BTK model unless the explicit energy dependence of the order parameter is taken into account; iii) the fit works well in the subgap region eV$< \Delta_1$ only in ab-plane contacts. In the case I || c instead the theoretical curves systematically show a zero-bias dip which is much deeper than the experimental one. This happens even if both Z_1 and Z_2 are unrealistically taken to be zero, because of the aforementioned Z-enhancing effect related to the shape of the relevant FS sheet. The failure of the model in reproducing the zero-bias region of the curves in c-axis contacts clearly indicates that either: i) there is some additional effect, not considered here, that gives rise to a zero-bias enhancing that partially compensates the signal depletion due to the shape of the FS, or ii) the smaller gap is not isotropic. The two possibilities are still under investigation, but preliminary (although detailed) results show that the existence on the hole-like FS of horizontal and/or vertical

node lines could not be sufficient to explain the observed discrepancy. In this regard, it is worth noting that only the use of the 3D BTK model allows unveiling effects like this, while the 2D BTK model (based on the assumption of spherical FS and with an adjustable weight) allows fitting the curves in both directions without any difficulty, as was done in [66].

4.5 Conclusions

The results reported so far on $Ba(Fe,Co)_2As_2$ represents the first systematic study of the superconductive properties carried out on thin films. Without any trivial measurements and data analysis, many unexpected results were obtained. Different Co-doped Ba-122 thin films of about 50 nm thickness, prepared by PLD on (001) CaF_2 single crystalline substrates, were morphologically and structurally characterized by means of RHEED, FE-SEM and AFM measurements. The films grow generally in a terraced island mode, with flat rectangular terraces that for example for 8% Cobalt content sample are of about 100 nm in size protruding by about 5 nm out of a back ground of well-connected grains. The surface of the samples is very smooth and homogeneous. The actual cobalt content, measured by EDX, is in good agreement with the nominal one for each samples here studied. Nevertheless, these films are slightly underdoped (indeed, the maximum T_c is achieved for $x = 0.10$) as also witnessed by the minimum in their R(T) curve. The discrepancy with the case of single crystals [115] is thus likely to arise from the strong compressive strain (and the consequent enhancement of the c/a ratio) induced by the CaF_2 substrate on Co-doped Ba-122 [113].
The critical temperature determined by electric transport measurements is indeed by almost 2 K higher than that of single crystals with the same cobalt content for the thin film with $x \geq 0.8$. The local surface critical temperature T_c^A was determined by point-contact spectroscopy in different regions of a given film. It turned out to be in perfect agreement with the resistive transition. The superconducting gaps measured by means of PCARS measurements are rather homogeneous over the surface on a millimetric scale, and their amplitudes are well compatible with those measured in single crystals of the same compound. All these features are fundamental in view of applications in superconducting electronics. The energy gaps of $Ba(Fe_{1-x}Co_x)_2As_2$ in a wide range of nominal doping ($0.04 < x < 0.15$) were determined by means of soft PCARS measurements. Several PCARS spectra were acquired on each sample, with the probe current injected perpendicular to the film surface and thus mainly along the c axis. In the optimal-overdoped region of the phase diagram the PCARS spectra admit a fit with the two-band 2D-BTK model using two isotropic gaps, and their shape does not suggest the presence of node lines on the FS; in the strongly underdoped sample ($x = 0.04$) a fit with a single isotropic gap is also possible, though a little worse than the two-gap one. Altogether, these results show no clear hints of changes in the gap symmetry or structure in the doping range of the films analysed in this work, although the shape of the spectra does not allow excluding some degree of gap anisotropy.
The small gap turns out to be approximately BCS, with a ratio $2\Delta_S/k_BT_c = 3.7 \pm 0.8$

(the uncertainty arises from the statistical spread of gap values) for $x < 0.10$, and smaller (2.6 ± 0.3) at $x = 0.15$. The second gap is much larger, with a ratio $2\Delta_L/k_BT_c$ of the order of 9 for $x < 0.10$ and 6.5 for $x = 0.15$.
The trend of the gaps and of T_c as a function of the Co content can be reproduced by a simple $s\pm$ Eliashberg model in which the spectrum of the mediating boson is that of spin fluctuations, and its characteristic energy coincides with the energy of the spin resonance. The decrease of the gap ratios in the overdoped samples is reflected in the values of the coupling strengths that are constant for $x < 0.10$ and slightly decrease at $x = 0.15$. This result finds a natural explanation within the picture of $s\pm$ superconductivity mediated by spin fluctuations: In the overdoped regime, far from the AFM region of the phase diagram, superconductivity may suffer from a suppression of the spin fluctuations and the loss of nesting [145], which could lead to a decrease in the superconducting interband coupling that, in turn, produces a larger decrease of the gaps in comparison *i*th the reduction of the critical temperature.
Finally, even if the experimental PCARS spectra do not show any zero-bias peak and can indeed be fitted well within the 2D BTK model by using two isotropic gaps, also the 3D BTK model gave some preliminary results. Indeed if the geometry of the FS is taken into account, as in the 3D model, it turns out that two isotropic gaps cannot account completely for the experimental spectra. In particular, a deep zero-bias dip for I || c is expected but not observed, suggesting that either the gap is zero in some regions of the FS (although simple node lines seem to be insufficient, which could point to the existence of 'hot spots" recently predicted on the hole-like FS), or additional phenomena are taking place that give rise to a zero-bias peak that partly compensates the depletion.

Chapter 5

Fe(Te,Se)

The Fe-based FSc $Fe(Te_{1-x}Se_x)$ has recently been the subject of an intense research effort, both experimental and theoretical. Despite its simpler structure if compared to 122 compounds [5], this material has been challenging the researchers and several of its properties have been (or still are) controversial. From the experimental point of view, for example, the presence of exceeding Fe has effects on the critical temperature, on the transport properties and on the magnetic properties (i.e. the spin fluctuations) which are not so easy to disentangle from the effects of the Se substitution [24]. Moreover, one of the fundamental steps in the study of new superconductors is the determination of the number, the symmetry and the amplitude of the superconducting energy gaps, but also in this respect $Fe(Te_{1-x}Se_x)$ has long been a puzzle. Various experimental techniques have given conflicting results, ranging from single [24, 52, 146, 147, 148] or multiple isotropic gaps [149, 150, 151, 152], to highly anisotropic or nodal gap(s) [153, 154]. The amplitudes of the gaps and of the gap ratios $2\Delta/k_BT_c$ are considerably scattered as well, so that it is difficult to extract a consistent picture. This is complicated by the fact that all the measurements reported in literature have been performed on a *single* doping content.
In this chapter the study of $Fe(Te_{1-x}Se_x)$ compounds with different Se content is reported. The investigation of the transport properties and of the energy gaps of $Fe(Te_{1-x}Se_x)$ thin films with different Se content ($x = 0.3$, 0.4 and 0.5) by the group of Prof. Maeda at the Univeristy of Tokyo (partner of the Japanese consortium of the EU-Japan Project IRON SEA) was carried out by the candidate mainly by means of PCARS spectroscopy. A deep analysis of the properties of this compound were performed by means of resistance and PCARS measurements also on $Fe(Te_{1-x}Se_x)$ single crystals.

5.1 Properties of $Fe(Te_{1-x}Se_x)$ samples

In this section the general properties of the samples of $Fe(Te_{1-x}Se_x)$ compounds are reported. The results of the preliminary characterization were performed by the partners of the Iron Sea Project after the deposition in order to clarify the interplay between thin films and substrate by means of EDX and TEM measurements [155].
Unfortunately these compounds are air-sensitive. This did not allow performing all the

measurements performed on Ba-122 thin films in order to characterize the morphological properties of the surface and the structural properties. Indeed the exposure to air was minimized and no AFM and FESEM measurements were performed on $Fe(Te_{1-x}Se_x)$ thin films, after the characterization measurements performed after the deposition.

5.1.1 Samples growth

Thin films on CaF_2 substrate

The films were grown by the group of prof. Maeda at the Tokyo University by pulsed laser deposition (PLD) using a KrF excimer laser (wavelength 248 nm) starting from a $Fe(Te_{1-x}Se_x)$ target, on top of commercially available CaF_2 (100) substrates. They reported the following parameters of the deposition: laser repetition rate 10 Hz, laser energy 300 mJ, substrate temperature 280°C, back pressure 10^{-7} Torr [155, 156, 157]. Some of the films were deposited by using a specially designed metal mask, directly put on top of the substrate, in order to obtain a six-terminal shape convenient for transport (resistivity) measurements (see Fig. 5.1 left panel). Others were instead deposited on the whole substrate (about $0.5 \times 0.5\,cm^2$) just to provide a larger area for point-contact spectroscopy measurements (see Fig5.1 right panel).

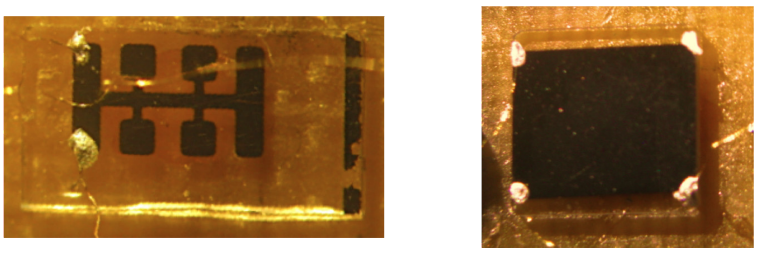

Figure 5.1: $Fe(Te_{1-x}Se_x)$ thin film with $x = 0.3$ Se content deposited by using a specially designed metal mask, directly put on top of the CaF_2 substrate (left panel) and with $x = 0.5$ Se content deposited on the whole area of the CaF_2 substrate (right panel).

Thin films on MgO substrate

The films were grown by pulsed laser ablation in a ultra high vacuum system [158, 159] starting from a $Fe(Te_{0.5}Se_{0.5})$ target prepared by direct synthesis from high-purity materials (Fe 99.9%, Se 99.9% and Te 99.999%) with a two-step procedure on single-crystals MgO substrate. The details of the deposition of the samples grown by the group of Dr. Ferdeghini (CNR-SPIN in Genova), are reported in [159].
The substrates were glued with silver paint onto a stainless steel sample holder compatible with the used scanning tunneling microscope (STM) (Omicron Nanotechnology GmbH). Deposition temperature, as measured by an infrared pyrometer, ranged between 300 and 650 ∘C. The films were deposited under high-vacuum conditions at a residual gas pressure of $5x10^{-9}$ mbar at the deposition temperature. The quality of the growth was in situ monitored by reflection high energy electron diffraction (RHEED) analysis and completed

by X-ray analysis [159].
The samples were analysed by means of transport and PCARS measurements. However the interdiffusion of oxygen and the evidence that the fluoride substrates are more suitable as substrates for Fe 11 superconducting thin film than oxide substrate [155] have led to prefer thin film on CaF_2 (100) substrates. In any case a comparison between the thin films on different substrates is reported at least in the phase diagram reported in the following section.

Single crystals

The $Fe(Se_{0.2}Te_{0.8})$ single crystals (used here as a term of comparison for thin films) were grown by the group of prof. Maeda at the Tokyo University, as described in ref. [160], by using Bridgman method starting from stoichiometrically weighed Fe (99.999% pure), Se (99.999% pure) and Te (99.999% pure). The as-grown crystals were then annealed in a moderate vacuum atmosphere ($\simeq$ 1 Pa). Unlike annealing in high vacuum, this process has been shown to increase significantly the critical temperature, probably thanks to the formation of an iron oxide layer on the surface (due to the reaction with the residual oxygen) that drags the excess Fe out of the bulk. The oxide layer is then removed mechanically.

5.1.2 Effect of substrate on the properties of thin films

The CaF_2 substrate is known to cause a sizable lattice strain in films of $Ba(Fe,Co)_2As_2$ that results in a stretch of the phase diagram with respect to that of single crystals [35]. In the case of $Fe(Te_{1-x}Se_x)$ films, the a-axis (c-axis) parameter is shorter (larger) than in single crystals [157, 161] and the critical temperature is considerably enhanced as well [157, 162]. Even if at a first glance this was expected to be correlated to strain effect of the substrate, TEM and EDX measurements have recently revealed that this seems to arise mainly from the chemical substitution of anions at the $Fe(Te_{1-x}Se_x)/CaF_2$ interface, while the lattice mismatch plays a secondary role [155]. In other words the close correlation between T_c and the structure of the lattice parameters of the thin films [156, 163] should be considered together with the chemical contamination.
Indeed the question of what substrates are suitable for the growth of thin films remains open. It seems that superconductivity is not correlated with the lattice mismatch; rather it is correlated with the degree of in-plane orientation and with the lattice parameter ratio c/a [156]. In this dissertation the candidate handled with $Fe(Te_{1-x}Se_x)$ thin films on two different substrates. The results were compared in order to highlight the effect of substrates on the critical temperature T_c.
In $Fe(Te_{1-x}Se_x)$ thin films on CaF_2 substrate, chemical interdiffusion is clearly visible in TEM measurements performed by the group of prof. Maeda and it occurs in a thin region of the order of 10 nm across the interface (see e.g. films A and B of ref.[155]). Since the thickness of these films is 100 nm for $x = 0.3$ and 0.4, and 86 nm for $x = 0.5$, this does not affect the composition of the films at the surface, as also clearly shown by EDX measurements at different depths [155]. The same results, as well as the absence of anomalous Hall effect [164] indicate that the excess Fe is negligible in these films. As

witnessed by XRD measurements, the films do not present detectable amounts of impurity phases, are c-axis oriented, and grow with a 45° rotation with respect to the underlying CaF_2 substrate, i.e. $Fe(Te_{1-x}Se_x)$ [100] ∥ CaF_2 [110].
In $Fe(Te_{0.5}Se_{0.5})$ thin films on MgO substrate broad peaks were observed by XRD analysis indicating probably the not excellent quality of the layer [159] due to the intrinsic nature of the substrate as confirm the same results obtained by Y. Imai and coworkers [156].

5.2 Resistance measurements

The transport properties, in terms of critical temperature on millimeter scale, were analysed by the candidate on the $Fe(Te_{1-x}Se_x)$ samples in order to verify also the good condition of the superconducting properties of the thin films. The resistivity was measured by using the four-probe van der Pauw configuration which is shown in Fig. 5.1 (right panel) on the $Fe(Te_{0.5}Se_{0.5})/CaF_2$ thin film. The resistivity of the single crystals were gently measured by the group of prof. Maeda (Tokyo University).
Fig. 5.2a reports the resistivity of the three films on CaF_2 substrate with $x = 0.3, 0.4$ and 0.5 as a function of temperature. The critical temperatures T_c^{90} and T_c^{10} are listed in the caption of the same figure. A magnification of the (normalized) curves in the region of the transition is reported in Fig. 5.2b, where also the normalized resistivity of a $Fe(Se_{0.2}Te_{0.8})$ single crystal is reported for comparison.
Fig. 5.3 reports the critical temperatures (T_c^{10} and T_c^{90}) of the samples studied in this PhD work by means of resistance and of PCARS measurements on top of a phase diagram for Fe(Te,Se) recently appeared in literature together with the measured performed on the $FeTe_{0.5}Se_{0.5}$ thin film on MgO. The measures performed on this sample did not contribute to the study of the fundamental properties carried on the Fe(Te,Se) compounds as previous justified. Nevertheless, the comparison between the results obtained on different substrates agree and complete the results present in literature [156, 159].
The critical temperature of the $FeTe_{0.6}Se_{0.4}$ thin film on CaF_2 agree with that found in single crystals (blue dots) while T_c of the $Fe(Te_{0.7}Se_{0.3})$ and $Fe(Te_{0.5}Se_{0.5})$ thin films are higher. The T_c of the film of $FeSe_{0.5}Te_{0.5}$ on MgO substrate is higher than that of single crystals. This disagreements are not surprising because of the effects of the substrate on the superconducting properties as mentioned in the previous section.
The comparison between the local critical temperatures determined by PCARS in thin Fe(Se,Te) films and the R vs T curve measured in the same films (as done on $Ba(Fe, Co)_2As_2$ compounds) is provided in the next section.

5.3 Point-contact Andreev-reflection measurements

PCARS measurements were performed by the candidate on the samples studied in this chapter by using the "soft" pressureless technique in which a thin Au wire ($\varnothing$ = 18 m) is kept in contact with the sample surface by means of a small drop ($\varnothing \leq$ 100 m) of Ag conducting paste, as shown in Fig. 5.4.
In this way, as previous mentioned, parallel nanometric contacts (that can well fulfill the

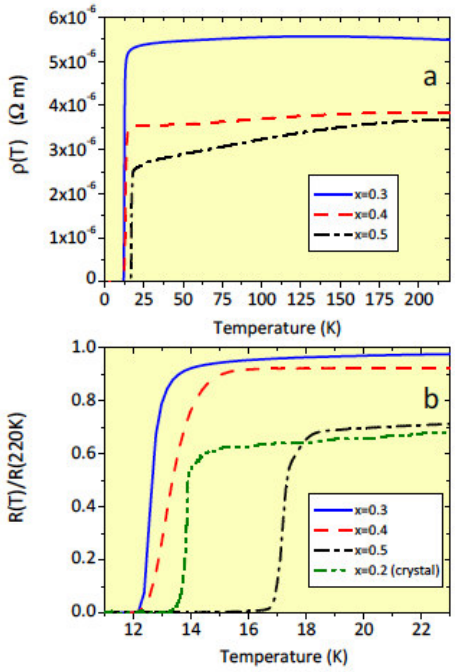

Figure 5.2: (a) Resistivity vs. temperature for the three films at different Se contents. The critical temperatures as determined from the resistive transitions are the following: for $x = 0.5$, $T_c^{90} = 17.3$ K and $T_c^{10} = 16.8$ K; for $x = 0.4$, $T_c^{90} = 14.3$ K and $T_c^{10} = 12.6$ K; for $x = 0.3$, $T_c^{90} = 13.3$ K and $T_c^{10} = 12.3$ K. (b) Normalized resistance R(T)/R(220 K) of the same films and of the $x = 0.2$ single crystal used for PCARS measurements, in the region of the superconducting transition. In the case of the single crystal, $T_c^{90} = 14.1$ K and $T_c^{10} = 13.6$ K.

requirement for the ballistic or diffusive conduction that are indispensable for PCARS [64]) are established here and there within the area covered by the Ag paste. This means that each PCARS spectrum is actually the result of a spatial average over a microscopic area of the sample surface. Also on $Fe(Te_{1-x}Se_x)$ thin film, the reason to prefer the "soft" pressure less technique to the conventional "needle-anvil" one is due both to the fragility of the CaF_2 substrate and to the much better thermal and mechanical stability of the PCARS spectra obtained in that way. Moreover the surface of the $Fe(Te_{1-x}Se_x)$ thin film were noticed to be more fragile that the $Ba(Fe_{1-x}Co_x)_2As_2$ systems, to the touch (as few stripes that are visible on the surface in Fig. 5.4 reveal) and air exposure. Therefore inert atmosphere and "soft" pressure less technique became fundamental in order to preserves the samples and allow repeatable measurements.

Thanks to the c-axis orientation of the films, the normal/superconductor interface is always parallel to the ab plane, that means that the probe current is always injected (mainly) along the c axis. All the contacts were in the regime of Andreev reflection, in which the potential barrier at the N-S interface is low enough to make Andreev reflection dominate over quasiparticle tunneling in the conduction through the contact. PCARS measurements

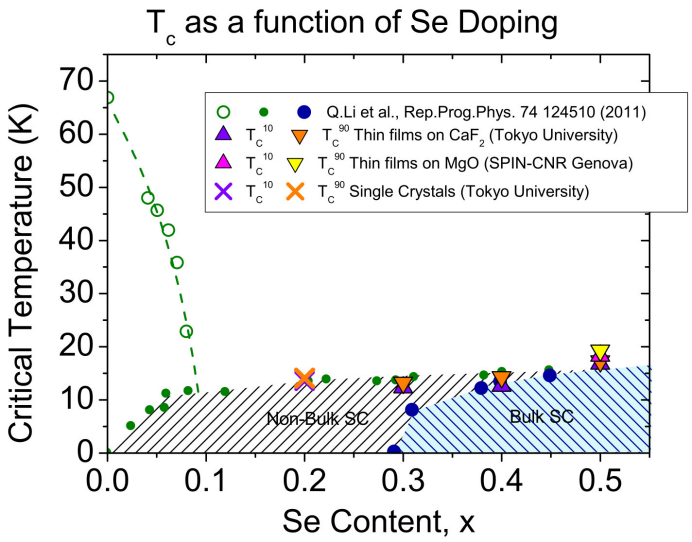

Figure 5.3: Critical temperatures (T_c^{10} and T_c^{90}) of the Fe(Se,Te) samples analysed in this work, compared to the phase diagram for single crystals taken from literature [165].

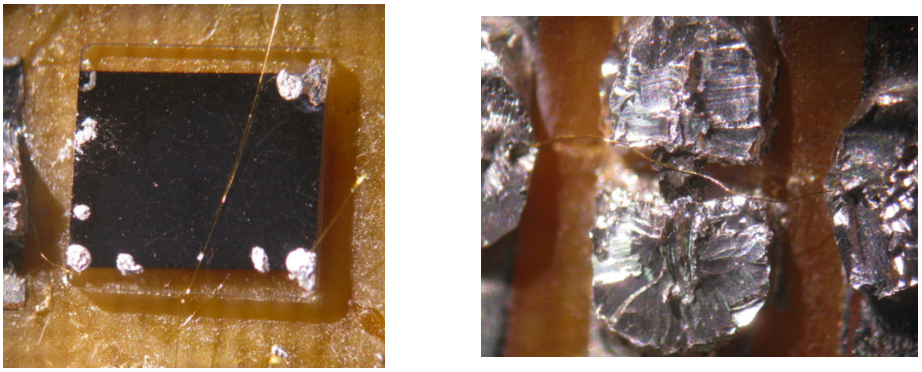

Figure 5.4: PCARS mounting on $Fe(Te_{0.5}Se_{0.5})/CaF_2$ thin film (left panel) and on $Fe(Te_{0.2}Se_{0.8})/CaF_2$ single crystals (right panel).

have been made in different points of the thin films under study in order to collect data from several zones of the surface.
Fig. 5.5 shows an example of the temperature dependence of the differential conductance curve (dI = dV vs. V) of a point contact whose resistance is R = 73.5 Ω, made on the film with $x = 0.3$.
The low-temperature curve presents no traces of anomalous features (zero-bias anomalies, downward bending of the high-energy tails, dips and so on) that could suggest the breakdown of the conditions for energy-resolved spectroscopy [2]. Instead, it presents the typical conductance enhancement (with symmetric maxima) caused by Andreev reflection at the interface, superimposed to an almost flat background. On increasing the temperature the

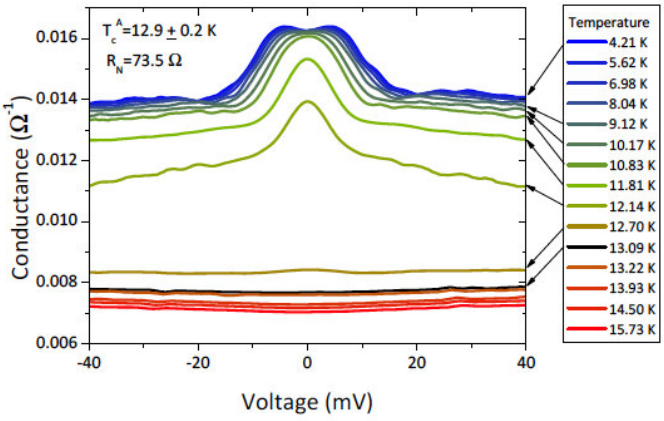

Figure 5.5: Temperature dependence of the raw conductance curves of a point contact on the film with $x = 0.3$. The black curve (T= 13.09 K) is the normal-state conductance.

Andreev reflection structure is progressively suppressed, as a consequence of both the thermal smearing and the decrease in gap amplitude, and the curves shift downward. At T $\geq$ 13.09 K the shape of the conductance curves does not change any longer. The relevant conductance curve (black) is identified with the normal-state conductance of the junction. Note that the local critical Andreev temperature T_c^A falls somewhere between 12.70 K and 13.09 K and thus we assume conservatively $T_c^A = 12.9 \pm 0.2$ K, which lies between T_c^{10} and T_c^{90} for this film as shown in the previous section and in Fig. 5.2.

5.3.1 Local critical temperature on micrometer scale

The comparison between the local critical temperature determined by PCARS in thin Fe(Se,Te) films and the R vs T curve measured in each thin film under study is provided in Fig. 5.6 and in Fig. 5.7. In these graphs the horizontal coordinate of the black points represents the local T_c^A, while their vertical coordinate is arbitrary and has been chosen for convenience to coincide with the resistance of the film at that temperature.
In general, the local critical temperatures T_c^A fall on the steeper part of the resistive transition. In the the film with $x = 0.4$ all the point instead lie between T_c^{90} and T_c^{onset}. Therefore thin films shows a general good homogeneity of the critical temperature at micrometer and millimeter scale An anomaly can be seen in the $x = 0.3$ film where one point lies in the region where the resistivity of the film is zero. It is likely that this point contact was made on a region with lower T_c, which is not seen in transport (i.e. because it is shunted by surrounding regions with higher critical temperature).

5.3.2 PCARS results and discussion

Coming back to the PCARS spectra collected on the different thin films, the first step of the data analysis was the calculation of the experimental normalized conductance. This is not an easy task to deal with PCARS spectra obtained on thin films. Indeed also in

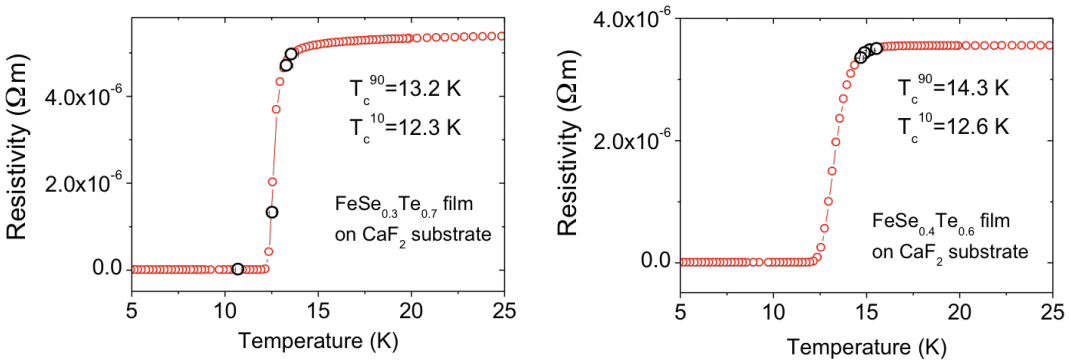

Figure 5.6: Local critical temperatures of the point contacts made on a $Fe(Se_{0.3}Te_{0.7})$ film on CaF_2 substrate (black symbols) compared with the temperature dependence of the resistivity of the same film (red symbols) in the left panel. (b) Same as in (a) but for $Fe(Se_{0.4}Te_{0.6})$ film on CaF_2 substrate in the right panel.

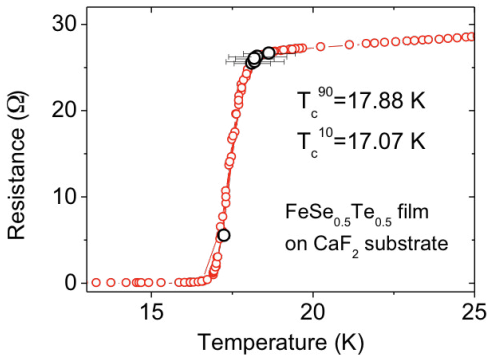

Figure 5.7: Local critical temperatures of the point contacts made on a $Fe(Se_{0.5}Te_{0.5})$ film on CaF_2 substrate, compared to the resistance of the same film.

$Fe(Se_{0.5}Te_{0.5})$ system the downward shift appear evident in the temperature dependence of the raw conductance curves (see Fig. 5.5). This downward shift of the conductance curves is typical of films (as already shown for $Ba(Fe,Co)_2As_2$) and is due to the spreading resistance contribution arising from the portion of the film between the point contact and the second voltage electrode [51, 110]. This means that: i) only the low-temperature curves have the correct voltage scale and can be used for spectroscopic purposes; ii) the conductance curve in the normal state cannot be used for the normalization of these curves, which is necessary in order to compare them with theoretical models and extract the gap values. The normalization therefore, as usual in Fe-based compounds [68], requires some caution and becomes somewhat arbitrary.
The problem was solved by using different (reasonable) normalization criteria for the same curve as was already explained for $Ba(Fe,Co)_2As_2$ PCARS spectra. Each PCARS spectra

was divided it by the normal-state conductance (vertically shifted until its tails coincide with those of the curve to be normalized) or by a polynomial fit of its high-energy tails. For any given contact, the spectra obtained by different normalization criteria were fitted independently; then, the amplitudes of the gaps were averaged and the spread of gap values obtained in all the fits was used to express the uncertainty on the gap values. In this way the uncertainty associated to the normalization is treated on the same footing as the other sources of uncertainty.
In Fig. 5.8 three examples, one for each doping content, of normalized conductance curves (symbols) are shown. Only the result of one of the possible normalization procedures is reported for clarity. In particular, here each raw spectrum was divided by a quartic curve that fits its high-energy tails.

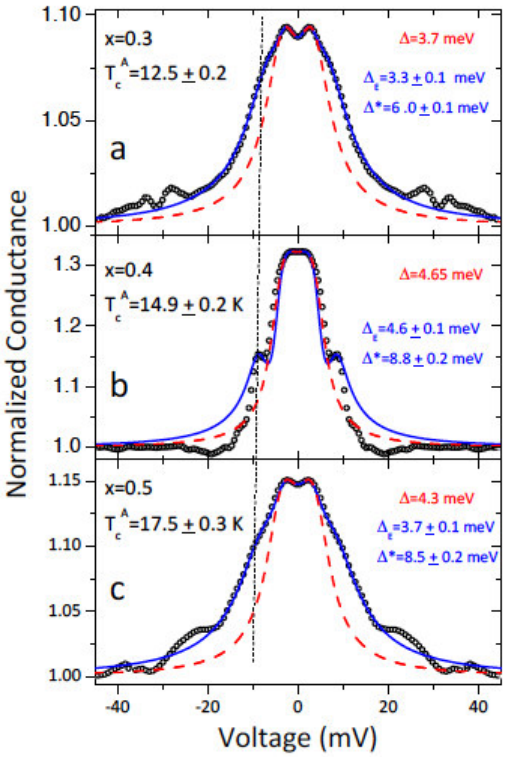

Figure 5.8: Three examples of normalized PCARS spectra (symbols) in films with different Se content, i.e. $x = 0.3, 0.4$ and 0.5 (from top to bottom). Red dashed lines: fit of the curves with the single-gap BTK model; the amplitude of the gap Δ is reported in the top right label of each plot. Solid blue lines: fit of the spectra with the 2D BTK model. The amplitude of the gap Δ_E and of the energy scale Δ^* (that actually corresponds to the EBI) are reported in the bottom right label of each plot.

All the spectra feature a pair of conductance maxima (or a smooth plateau) at an energy of the order of 3 meV, which are the typical features associated to a nodeless superconducting gap. Additional structures are present as well, that can take the form of smooth,

but well pronounced shoulders (as in panels a and c), or even small peaks (as in panel b). The shape of these structures is, in all cases, perfectly compatible with that expected for the features associated to a larger superconducting gap and indeed curves very similar to these have been actually measured in various multiband compounds, including hole- and electron-doped Ba-122 (see [68] and references therein). The problem here is that the energy of these structures is of the order of $8-9$ meV. For example, in the spectrum of Fig. 5.8 where the peaks are easy to identify, their energy is ± 8.8 meV. A gap of this amplitude would result in a gap ratio $2\Delta/k_BT_c \approx 13$ which looks absolutely unreasonable, even for iron-based compounds where values of the order of 9 have been sometimes found [68]. It is thus rather likely that these structures are the signature of another energy scale, which is not a superconducting gap but pertains to the superconducting state as well, because the structures disappear at the critical temperature of the contact. It is thus practically impossible to extract only the spectral information about the energy gap and to get rid of these structures, which moreover have a very high spectral weight.

The number of energy gaps in Fe(Se,Te) system is highly debated. Most of the experimental techniques used so far to investigate this material show a single gap; in particular, this holds for STS [52, 147] and tunnel measurements [148]. In the $Fe(Se_{0.4}Te_{0.6})$ thin film the point-contact spectra often showed tunnel-like structures instead of Andreev-reflection ones. This may be due to the presence of an insulating or highly diffusive layer on the surface. The tunnel-like features were actually very weak and impossible to compare with any model. Some examples are reported in Fig. 5.9 together with tunnel, STS and PCARS spectra from literature. The spectra of this sample shows a weak conductance depletion at zero bias, and structures at about ± 3.3 meV and ± 6.5 meV. The former are compatible with the PCARS spectra by Park et al.[166] and with the STS spectra by Kato et al. [147], but not with those by Hanaguri et al. [52]; the second feature can be also detected in some of the PCARS spectra in literature but is not seen by tunnel or STS. This may seem to indicate that only the smaller feature is due to a gap. Interestingly, however, optical conductivity measurements [149] have given two gaps of 2.5 meV and 5.2 meV in a $FeTe_{0.55}Se_{0.45}$ sample with $T_c = 14$ K.

At a first analysis, it is not even clear whether a single-gap fit that completely disregards the structures at energy above 4 meV provides a reliable amplitude of the superconducting gap. Dashed lines in Fig. 5.8 represent the results of fitting the spectra with the standard 2D-BTK model for a single-gap superconductor [111]. This model (as described in 2.4) contains three parameters, i.e. the gap amplitude Δ, the effective broadening Γ, and a dimensionless parameter Z that accounts for both the height of the potential barrier at the interface and the mismatch of the Fermi velocities between the normal metal and the superconductor. The amplitudes of the gap obtained from the fit are reported in the top right label in each panel of Fig. 5.8. Even though they certainly provide the order of magnitude of the energy gap, these values suffer from the uncertainty on what has to be considered the real amplitude of the Andreev signal associated to the superconducting gap, because of the contemporary presence of the higher-energy structures.

If instead one acts as if also the shoulders were due to a superconducting gap and thus fits the spectra with the two-band 2D BTK model, one obtains the solid blue lines superimposed to the experimental data. Therefore keeping in mind that the larger energy scale is

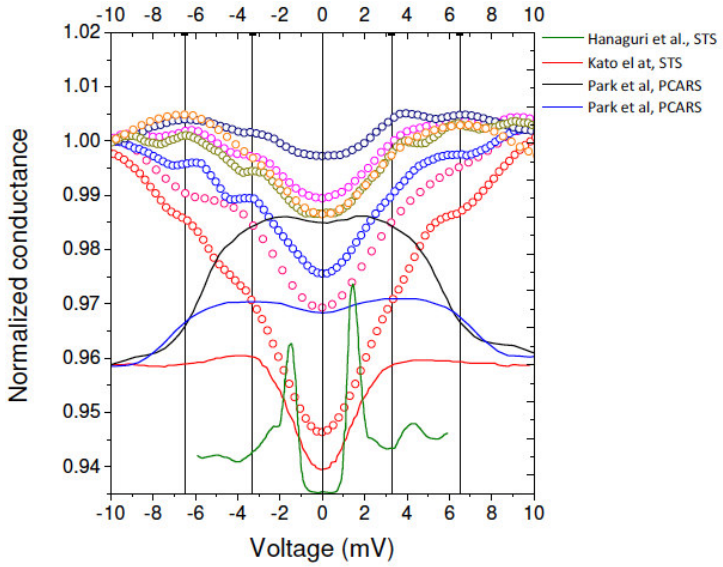

Figure 5.9: Examples of tunnel-like spectra often measured in the $Fe(Se_{0.4}Te_{0.6})$ thin film. (symbols) compared to PCARS and STS data from literature (lines). Our data, although the signal is too small to be fitted, show features at about 3.3 meV that correspond to the energy gap measured by STS (Kato et al.) and additional structures at about 6.5 meV occasionally seen also by Park et al. as a kink in their PCARS spectra. Whether these structures are due to a second gap is a debated point; the fact that they are not seen by STS seems to indicate that they are not.

likely not to be a gap, the fit the curves by using a two-band BTK model, was done. Let us call Δ_E the amplitude of the true superconducting gap and Δ^* the energy scale of the additional structures. The reason to do so will be clear in the following. Then an effective two-gap 2D BTK model was used in which the normalized conductance is expressed as a weighted sum of two contributions, i.e. $G = w_E\sigma_E + w^*\sigma^*$ [2]. The fitting function thus contains three parameters for each contribution, i.e. the energy scale (Δ_E or Δ^*), the effective broadening (Γ_E or Γ^*), and the barrier parameter (Z_E or Z^*). Also the weight w_E (or $w^* = 1 - w_E$) is a free parameter. The number of parameters makes the fit be nonunivocal, in the sense that there is actually a range of best-fitting parameters for a single curve. This model is surprisingly effective in reproducing all the main features of the curves. The values of Δ_E and Δ^*, with the relevant uncertainty, are reported in the labels. Note that Δ_E has a small uncertainty because it is associated to rather sharp conductance maxima whose position is not affected by the choice of the normalization criterion. Moreover, the amplitude of Δ_E is smaller (especially in panels a and c) than the value obtained by means of the single-gap fit. Finally, it is possible to show that there is no correlation between the values of Δ_E and Δ^* and the contact resistance, which indicates that the features we have fitted as gaps are not artifacts due, for example, to the non-spectroscopic nature of the contacts [51, 64]. On the contrary, the values of Δ_E scale rather well with the local critical temperature T_c^A giving a constant gap ratio $2\Delta_E/k_BT_c \approx 5.5$, which is well above the BCS weak-coupling limit but not abnormal in Fe-based compounds. The values of Δ^* are more

scattered, but their overall trend as a function of T_c^A can be approximately expressed as $2\Delta^*/k_BT_c \approx 11.5$.
Two points must then be clarified:
i) which of the two fitting procedures (with a single-gap or a two-gap model) gives the correct value of the superconducting gap Δ_E;
ii) what is Δ^*.
As for the first point, a possible cause of the structures at Δ^* could be the strong electron-boson interaction (EBI). As a matter of fact, it was already shown in Co-doped Ba-122 [66] and in F-doped Sm-1111 [68] that EBI structures are indeed observable by point-contact spectroscopy not only in the tunneling regime but also in the Andreev-reflection regime. It was also shown that these structures can be accounted for rather well by inserting into the BTK model the energy-dependent order parameters calculated, within the Eliashberg theory, by using a Lorentzian electron-boson spectrum $\alpha^2F(\Omega)$ peaked at the energy of the spin resonance Ω_0 (measured by inelastic neutron scattering experiments [167]) that scales with T_c according to the empirical law $\Omega_0 = 4.65k_BT_c$ [5]. As shown elsewhere [68], the peak in the $\alpha^2F(\Omega)$ results in a peak in the sign-changed derivative of the conductance, $-d^2I/dV^2$ vs. V , that approximately occurs at $\Omega_0 + \Delta max$. This method was also applied to study the Ba122 thin films as reported in the previous chapter will good results and it was also applied on $Fe(Te_{1-x}Se_x)$ thin films.

5.3.3 PCARS measurements within the Eliashberg theory

Let us assume that Δ_E is the energy gap, and check whether the coupling of electrons with spin fluctuations can give rise to higher-bias additional structures similar to those observed experimentally. For example, let us focus on $Fe(Te_{1-x}Se_x)$ with a critical temperature of about 14 K and $\Delta_E = \frac{5.5}{2}k_BT_c = 3.3$ meV. Recent angle-resolved photoemission spectroscopy (ARPES) measurements have given direct evidence of 3 bands crossing the Fermi level in $Fe(Te_{0.55}Se_{0.45})$ with $T_c = 14.5$ K, i.e. two holelike bands at the Γ point of the Brillouin zone and one electronlike band at the M point [151]. DFT calculations [153] give evidence of two holelike FS sheets (almost perfectly cylindrical) and two electronlike FS sheets, of which the inner one is almost cylindrical while the outer one displays a strong warping.
The effective three-band Eliashberg model was build by using two effective holelike Fermi surfaces (labeled as 1 and 2 in the following) at Γ and one electronlike FS (labeled as 3) at M. The ratio of the density of states at the Fermi level was estimated from DFT calculations, obtaining $N_1 = N_3 = 0.46$ and $N_2 = N_3 = 1$, and the following assumptions (for details see ref. [59, 69]) was done as usual:
i) the contribution of phonons to the coupling is negligible;
ii) the interband coupling is mediated by spin fluctuations, while the intraband coupling is negligible; iii) the Eliashberg function $\alpha^2F(\Omega)$ has the same shape for all coupling channels, but its height is modulated by the corresponding coupling constant (i.e. λ_{12}, λ_{13}, λ_{23});
iv) the coupling between the two holelike bands is negligible, so $\lambda_{12} \simeq 0$; v) the $\alpha^2F(\Omega)$ is a Lorentzian curve peaked at the energy of the spin resonance, $\Omega_0 = 4.65k_BT_c$ [5], and its half-width at half maximum is $\Omega_0/2$ as it is possible to in the left inset in Fig. 5.10;

vi) the Coulomb pseudopotential is negligible (and thus it was assumed $\mu^*_{ij} = 0$ for any i, j.

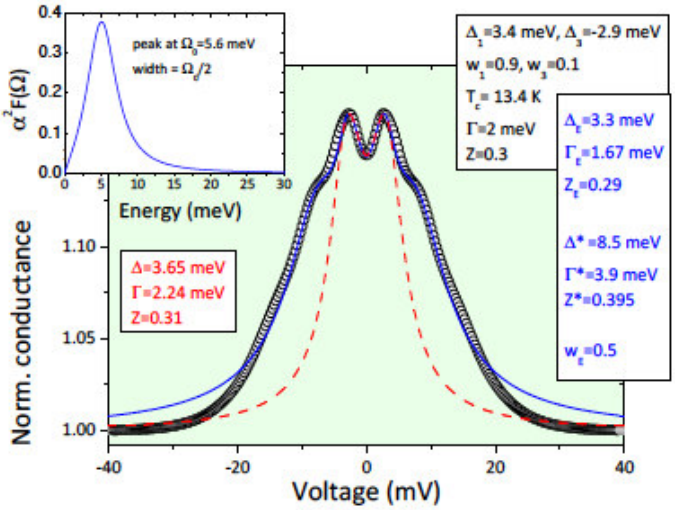

Figure 5.10: Symbols: theoretical PCARS spectrum calculated within the two-band 2D BTK model by using the energy-dependent order parameters Δ_1 and Δ_1 obtained from the Eliashberg model. The parameters of the BTK model are reported in the top right label, including the amplitude of the gaps whose different sign is due to the $s\pm$ symmetry. The theoretical spectrum presents, in addition to the conductance maxima due to the gaps (almost identical in amplitude) clear shoulders due to the EBI. Solid blue line: fit of the theoretical PCARS spectrum with a two-band 2D BTK model. The fit is made by treating the EBI shoulders as if they were due to a large gap Δ^*. The best-fit parameters are listed in the bottom right label. Red dashed line: fit of the theoretical PCARS spectrum with a single-band 2D BTK model. The best fitting parameters are reported on the left label. Inset: the shape of the electron-boson spectrum (Eliashberg function) used in the calculations.

In the end, the model contains only two free parameters, λ_{13} and λ_{23}, that can be adjusted to reproduce the values of the gaps. Since the position of the EBI structures depends on the energy of the mediating boson and on the largest superconducting gap, and since the idea was just to check whether these structures can be mistaken by a gap, the simplest possible assumption, i.e. that two gaps exist of similar amplitude, was used. Once λ_{13} and λ_{12} are determined, the critical temperature is calculated with no additional adjustment of the parameters. It was so found that the experimental situation (T_c of about 14 K, and one single gap amplitude of about 3.3 meV) can be obtained by using $\lambda_{13} = 0$ and $\lambda_{23} = 4.1$ (this value looks large but corresponds to a total coupling constant $\lambda_{tot} = 1.56$). In particular, it turned out that $T_c = 13.4$ K, $\Delta_1 = 3.4$ meV, $\Delta_2 = 0$, $\Delta_3 = -2.9$ meV. The two non-zero gaps are very similar in amplitude but differ in sign because of the $s\pm$ symmetry. The problem has thus been reduced to a two-band one and therefore the energy-dependent order parameters can be inserted into the two-band 2D BTK model to

calculate the normalized conductance. Keeping the same labels for the bands, the conductance can be conveniently expressed as $G(V) = w_{11}(V) + (1 - w_1)\sigma_3(V)$. The resulting curve always shows maxima due to the gaps at about 3 meV, plus additional shoulders or even small peaks due to the EBI. A curve qualitatively similar, in amplitude and shape, to the experimental ones is shown in Fig. 5.10 (symbols). It was obtained by choosing $w_1 = 0.9$, $Z_1 = Z_3 = 0.3$ and $\Gamma_1 = \Gamma_3 = 2$ meV. For a further check, this curve was tried to fit with the two- band 2D BTK model with constant (BCS) energy gap, thus doing exactly what was done with the experimental spectra, and treating the EBI structures as if they were due to a larger gap. The result of the fit is shown by a solid blue line in Fig. 5.10, and the corresponding parameters are listed in the label. Note that the fit gives $\Delta_E = 3.3$ meV, in very good agreement with the original amplitude of the gap with which the curve was generated, and $\Delta^* = 8.5$ meV, which is perfectly compatible with the values of Δ^* obtained from the two-gap fit of the experimental PCARS spectra at $T_c^A = 14$ K. Instead, the single-gap fit of the conductance curve (dashed red line in Fig. 5.10) would give a gap amplitude $\Delta = 3.65$ meV which is slightly overestimated.
The above discussion proves that: i) the high-energy structures observed in the PCARS spectra are very likely to be due to the EBI; ii) Δ^* is not a gap, but rather the energy at which the EBI manifests itself in the conductance; iii) the amplitude of the superconducting gap Δ_E is better reproduced by the two-gap BTK fit than by the single-gap fit.
A step forward can now made in order to understand whether Δ_E is the only superconducting gap detected by PCARS. Interestingly, this gap is in very good agreement with the gap that has been recently measured by ARPES on the electronlike FS [151]. Actually, in the films with $x = 0.5$ there are some experimental facts that suggest that a second, smaller gap might be present as well, even though with a small weight. This evidence results not so clear in the films with $x = 0.3$ and $x = 0.4$ possibly because the second gap is too small to be detected. In some curves, the single-gap fit or even the two-gap fit (with Δ_E and Δ^*) are not completely satisfactory in the low-energy region eV $< \Delta_E$, where a small excess conductance exists as shown in Fig. 5.11.
This small discrepancy can be removed if the low-energy part of the curves is fitted (disregarding the EBI structures) by means of the two-band BTK model and, in addition to Δ_E, a second smaller gap Δ_H is considered (blue solid lines in Fig. 5.11a and b). The fit is obtained here with $\Delta_E = 5.0 \pm 0.3$ meV and $\Delta_H = 2.3 \pm 0.1$ meV (panel a) and $\Delta_E = 4.4 \pm 0.2$ meV and $\Delta_H = 2.5 \pm 0.1$ meV (panel b). A more convincing evidence for the existence of the small gap Δ_H comes from some PCARS curves in which the EBI shoulders are hardly detectable (for unknown reasons) and the Andreev-reflection structures are not, or poorly, disturbed by them. An example is given in Fig. 5.11c. The fit of this curve again gives $\Delta_H = 2.3 \pm 0.1$ meV and $\Delta_E = 4.1 \pm 0.2$ meV. Finally, the most striking proof of the fact that an additional smaller gap exists comes from PCARS measurements carried out, with the same technique and in the same configuration (c-axis injection) in single crystals of $Fe(Te_{0.8}Se_{0.2})$. An example of these curves is shown in Fig. 5.11d. Note that the local critical temperature of this contact is higher than T_c^{90} of the crystal (see Fig. **??**). This anomaly has been already observed in $Fe(Te_{0.55}Se_{0.45})$ crystals [146] and might be due to a different local concentration of excess Fe. In our case, the point contacts were made on a fresh surface exposed by cleaving the crystal while the contacts for the resistance

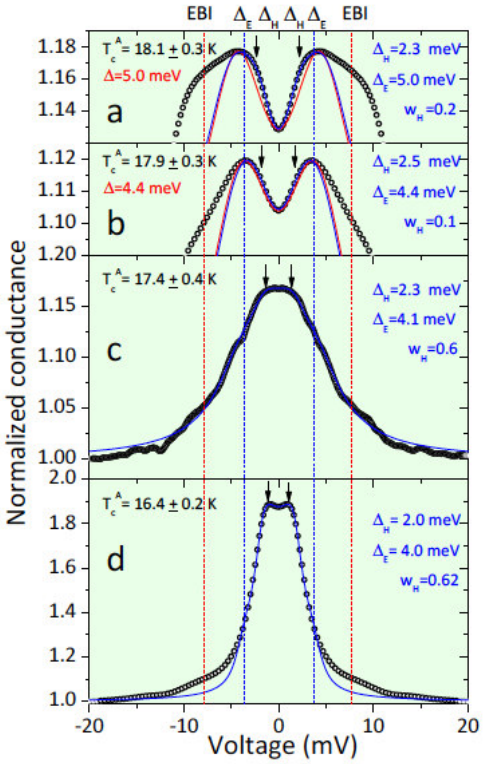

Figure 5.11: Some examples of PCARS curves giving evidence for the smaller gap Δ_H. In all cases the gap amplitude obtained from the fit are indicated in the labels. (a,b) Detail of two spectra measured in Fe(Te,Se) thin films with $x = 0.5$ that show a small excess conductance inside the maxima associated to Δ_E that cannot be fitted by a single-gap model (red line) and is instead perfectly captured by a two-gap model (blue line) with Δ_E and the inner gap Δ_H. (c) one of the few curves in the $x = 0.5$ films where the EBI structures are less pronounced and a two-band fit with the gaps Δ_H and Δ_E is able to reproduce most of the curve. (d) A PCARS spectrum taken in a single crystal, in which the superconducting signal is almost ideal, with the relevant fit (blue line). Vertical dashed lines approximately indicate the position of the features associated to the EBI and to the gap Δ_E. Arrows indicate the structures associated to the smaller gap Δ_H.

measurements were placed on the original surface. This, taking into account the process of outward migration of interstitial Fe atoms induced by annealing, probably explains the discrepancy in the critical temperatures. The superconducting signal is extremely high here, close to the theoretical limit of 2, which means the contact is nearly ideal. The experimental curve shows two clear maxima corresponding to Δ_H, a change in slope at an energy corresponding to Δ_H and wide, but much lower, EBI shoulders at higher energy. The two-band fit of the curve (neglecting the EBI structures) gives $\Delta_H = 2.00 \pm 0.5$ meV and $\Delta_E = 4.0 \pm 0.1$ meV. Now all the information on the three energy scales obtained so far can be considered together i) the results of the two-band BTK fit of the conductance curves that give evidence of Δ_E and of the EBI structures at Δ^* and not of Δ_H. All the PCARS spectra in the films with $x = 0.3$ and $x = 0.4$, but also some of the spectra in the

$x = 0.5$ film, are of this kind (see Fig, 5.8); ii) the results of the fit of all the spectra that also provide evidence for the smaller gap Δ_H, like those in Fig. 5.11 and others obtained in similar situations. All the available values of Δ_H, Δ_E and Δ^* are plotted in Fig. 5.12 as a function of the local critical temperature of the contacts, T_c^A.

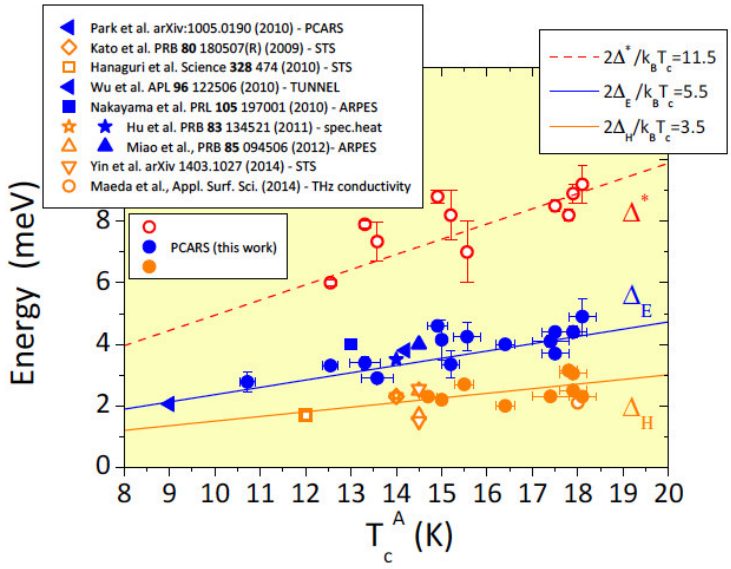

Figure 5.12: Gap amplitudes Δ_H (orange symbols) and Δ_E (blue symbols) and EBI energy Δ^* (red open symbols) as a function of the local critical temperature T_c^A. Data from literature are added for comparison; in these cases, the critical temperature is the one declared in the original papers. The data come from PCARS [146], STS [52, 147, 152], ARPES [24, 151], tunnel spectroscopy [148], specific heat [168] and THz spectroscopy [169].

A clear picture emerges in which all the three energy scales depend on the critical temperature in a linear way. The gaps scale rather well with the critical temperature according to a constant gap ratio, i.e. $2\Delta_H/k_BT_c^A = 3.5$ for Δ_H and $2\Delta_E/k_BT_c^A = 5.5$ for Δ_E. For the energy Δ^*, the values are more scattered but approximately fall on the line $2\Delta^*/k_BT_c^A = 11.5$. The same figure also reports the results of many measurements of the energy gaps in $Fe(Te_{1-x}Se_x)$ taken from literature; in these cases, the critical temperature is that declared in the original paper. The agreement with our results is excellent; actually, the systematic investigation of the energy gaps as a function of T_c^A (and thus of the doping) performed here for the first time allows understanding and explaining within a single simple picture the apparent scattering of gap data present in literature. It is possible to see that PCARS data perfectly agree with recent results of ARPES [151] and STS [152] as well as with the results of THz conductivity carried out in the same films at $x = 0.5$ [169]. With respect to the ARPES result, it is possible to conclude that PCARS can detect very easily the gap Δ_E associated to the electronlike FS, and with more difficulty a gap Δ_H that is probably the average of the gaps residing on the two holelike pockets, and that are too close to be resolved by PCARS. The easier detection of Δ_E might be explained by the

fact that the electronlike FS is more 3D than the holelike ones and this makes its weight for c-axis conduction be greater. This explanation however conflicts with the fact that STS measurements [152] performed with I ∥ c axis, exactly as in PCARS measurements performed on thin films, detect the two holelike gaps and not the electronlike one as shown in Fig. 5.13.

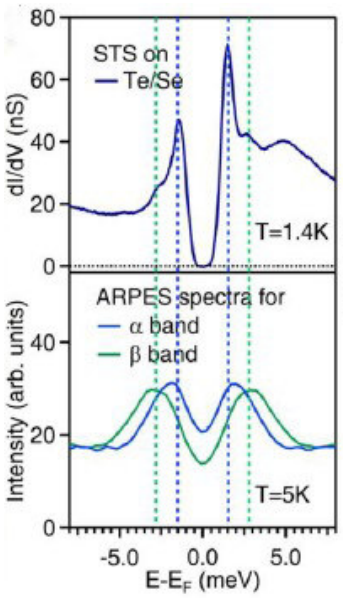

Figure 5.13: STS and ARPES measurement of the energy gap [152].

The reason for this discrepancy may be due to the higher directionality of tunneling spectroscopy (so that it mainly probes states with small in-plane momentum component and thus is more sensitive to the region around Γ [1]) with respect to Andreev-reflection spectroscopy. Indeed, in the pure Andreev-reflection regime ($Z = 0$) the normal-state probability of electron injection is isotropic (i.e. identical for all directions in the whole half-space). In these conditions, the "weight" of each FS sheet in the spectra is proportional to the area of its projection on a plane perpendicular to the direction of current injection [142], which means that the FS sheets with enhanced 3D character should dominate the conductance for I ∥ c. In the pure tunneling regime ($Z = \infty$), instead, the probability of electron injection strongly decreases on going away from the normal direction, and this makes the FS sheets with small transverse component of k be dominant in the spectrum. The experimental curves were always fitted by using isotropic gaps. This is due to the fact that the PCARS spectra do not show any clear evidence of nodes in the order parameters, although this does not exclude the presence of local gap minima in some of the Fermi surfaces. This said, in c-axis contacts there were found no clear hints in favor of the fourfold gap anisotropy observed by directional specific-heat experiments [153]. It is true, however, that also ARPES [151] and STS [152] results are compatible with isotropic gaps. Maybe a possible explanation of this disagreement is that given in ref. [151] where the anisotropy

observed by directional specific heat is ascribed to the anisotropy of the Fermi surface with respect to the Γ point, rather than to the anisotropy of the gap on a single specific FS sheet. To investigate this point in greater detail, further PCARS measurements maybe in single crystals could be performed.

5.4 Conclusions

The results of the first extensive study of the superconducting gaps in $Fe(Te_{1-x}Se_x)$ with various Se contents, i.e $x = 0.3$, $x = 0.4$ and $x = 0.5$ were presented in this chapter. The resistance measurements (performed by van der Pauw method) and the local critical temperature performed by PCARS were compared in order to verify the homogeneity of the superconductive properties on the samples.
The gaps were been determined by means of PCARS in epitaxial films grown by PLD on single-crystalline CaF_2 substrates. The PCARS spectra generally show clear symmetric maxima associated to a superconducting gap of amplitude $\Delta_E \approx 2.75 k_B T_c$ and additional, very clear shoulders that can be mistaken for a gap of amplitude $\Delta^* \approx 6 k_B T_c$ but are very probably the signature of the strong coupling of electrons with a bosonic mode peaked at an energy Ω_0 - that roughly obeys the empirical rule $\Omega_0 = 4.65 k_B T_c$ demonstrated for the spin resonance energy. A comparison with the results of ARPES suggests that the gap Δ_E might be located on the electronlike FS sheet. A careful analysis of the low-energy region of some spectra taken in the $x = 0.5$ films suggests the existence of a (hardly detectable) smaller gap $\Delta_H = 1.75 k_B T_c$. More reliable evidences of this smaller gap come from the fit of a few spectra where the EBI structures are partly suppressed, and even more from PCARS measurements in single crystals, which clearly show both the gaps Δ_E and Δ_H and the EBI structures. Once plotted as a function of the local critical temperature, Δ_E and Δ_H provide a unifying framework in which all the data reported in literature (and characterized up to now by an apparently unreasonable spread) perfectly fit. In particular, the smaller gap Δ_H turns out to be the "average" of the two gaps residing on the holelike FS sheets recently identified by ARPES and STS.

Chapter 6

Summary and conclusions

The characterization and the fundamental study of Fe-based SCs, belonging to the 122 and 11 families, mainly in the form of epitaxial thin films, was carried out in this dissertation. By means of Atomic Force Microscopy (AFM), Field Emission Scanning Electron Microscopy (FESEM) and Energy-dispersive X-ray spectroscopy (EDX) the morphological and the chemical composition of the surface was investigated. Electrical transport measurements (mainly resistivity and resistance) and point-contact Andreev-reflection spectroscopy (PCARS) were used to carry out both the advanced characterization and the investigation of the fundamental properties.
The phase diagram of $Ba(Fe_{1-x}Co_x)_2As_2$ and $FeTe_{1-x}Se_x$ compounds was studied in mainly two steps:

- the analysis of the effect of aliovalent doping on the critical temperature T_c and on the amplitude, number and symmetry of the superconducting gaps;
- the calculation of the characteristic energy of the mediating boson and the coupling strengths as a function of doping, within the Eliashberg theory applied to the experimental PCARS spectra.

Although the study of the these compounds was carried out mainly with the same experimental techniques and the same theoretical model, some differences in the method of investigation were mandatory due to the different level of sensitivity and degradation to air exposure. Since the detailed conclusions of the studies were reported in the prevoius chapters, here the summary of the investigation of $Ba(Fe_{1-x}Co_x)_2As_2$ and $FeTe_{1-x}Se_x$ compounds is reported. The steps followed in the study of each compounds are briefly described here before pointing out their differences and similarities.

$\mathbf{Ba(Fe_{1-x}Co_x)_2As_2}$

Co-doped Ba-122 thin films were investigated in the following steps:

- FESEM, AFM and EDX measurements in order to characterize the morphological and chemical properties. The surface of the samples was generally very smooth and

homogeneous also in terms of chemical composition which was in agreement with the nominal (i.e. target) value.

- resistance measurements (performed by collinear and vdP method) in order to determine the critical temperature. The local critical temperature T_c^A was determined by PCARS in different regions of the thin films and it turned out to be in perfect agreement with the relevant R vs T curve.
  A difference was found between the value of the critical temperature of the thin films (even 2 K higher) and the one of single crystals with the same cobalt content. This was more visible in the overdoped region of the phase diagram. The strain-effect of the substrate [113] can well explain this experimental results.

- PCARS measurements in order to investigate the number and the amplitude of the energy gaps. Rather homogeneous values of two gaps were measured the surface of the thin films obtained by fitting the PCARS spectra with a 2D BTK model with two isotropic gaps. The values of the amplitude of the gaps in thin films agreed in general with the values measured on single crystals [66].

- the trend of the gaps and of T_c as a function of the cobalt content was investigated by three-band Eliashberg model. It turned out to be compatible with a mechanism of superconducting coupling mediated by antiferromagnetic spin fluctuations.

- PCARS measurements were also fit by using the 3D BTK model. The results so obtained showed the failure of the 3D BTK model may be due to several factors, which in any case deserve investigation.

Also a sample of 8% cobalt doped Ba122 compound on MgO with Fe buffer layer was investigated. Unfortunately the evidence that the Fe layer acts as a shunt [170] suggested to prefer thin films on a different substrate.

$FeTe_{1-x}Se_x$

The morphological and the chemical properties of the $FeTe_{1-x}Se_x$ on CaF_2 thin films were not systematically studied by using FESEM, AFM and EDX measurements. The strong air sensitivity of these samples did not allow to carry out the study that was completed in Ba122 thin films.
This compound was investigated by keeping the samples in inert atmosphere during all the time of measurements in following steps:

- resistance measurements in order to determine the critical temperature. The local critical temperature T_c^A was determined by PCARS measurements also in these compounds and in general it turned out to be in perfect agreement with the resistive transition.

- PCARS measurements in order to investigate the number and the amplitude of the energy gaps. Rather homogeneous values of two gaps were measured of the surface of the thin films obtained by obtained by fitting the PCARS spectra with a 2D BTK

model with two isotropic gaps. The values of the amplitude of the thin films agreed in general with the values found in literature.

- PCARS were analysed within the $s\pm$ three-band Eliashberg model. The results so found turned out to be compatible with a mechanism of superconducting coupling mediated by spin fluctuations.

$Fe(Se_{0.2}Te_{0.8})$ single crystals were analysed within two steps:

- PCARS measurements in order to investigate the number and the amplitude of the energy gaps and to compare the values so obtained with those obtained in thin films measurements. PCARS spectra were obtained by fitting the PCARS spectra with a 2D BTK model with two isotropic gaps. The values of the amplitude of single crystals seems to confirm the trend of the energy gaps obtained on thin films.

- PCARS spectra were analysed also by using the three-band Eliashberg model. The results so obtained seems to confirm a mechanism of superconducting coupling mediated by spin fluctuations.

Similarities and differences

The high quality of the $Ba(Fe_{1-x}Co_x)_2As_2$ and $FeTe_{1-x}Se_x$ thin films allowed obtaining really good results. Even if epitaxial thin films are not the usual systems considered in order to carry out fundamental study, the homogeneity of the superconductive properties generally (verified on all the samples analysed in this work) allowed obtaining really good and unexpected results in the matter of 122 and 11 Fe-bases SCs.
The transition temperatures as determined from resitivity measurements of both the compounds turned out to be in good agreement with the local critical temperature T_c^A measured by PCARS. $Ba(Fe_{1-x}Co_x)_2As_2$ samples revealed in general to be stronger to air exposure then $FeTe_{1-x}Se_x$ thin films, despite aging effect due to a quite long period (one or two weeks) in which the samples were kept into humid atmosphere. This characteristic allowed investigating morphological and chemical features in Ba122 thin films by means of several FESEM, AFM and EDX measurements.
The effect of the substrate on the critical temperature was clearly underlined in literature [113, 155] but it was not specifically investigated in this work. Few points were discussed about both $Ba(Fe_{1-x}Co_x)_2As_2$ and $FeTe_{1-x}Se_x$ thin films. They seem to show a different behaviour even if they were deposited on the same CaF_2 substrate: the strong strain effect of this substrate on $Ba(Fe_{1-x}Co_x)_2As_2$ system seems not to cause the same increase in critical temperature in $FeTe_{1-x}Se_x$ compound. Moreover all the measurements involved in the fundamental study were performed on systems with the same substrate and different doping content, in order to consider thin films with the same strain/stress effect. Ultimately the energy gap behaviour was studied as a function of the critical temperature. A possible development of this work could be the comparison of the same Fe-based SCs compounds with the same doping content but on different substrates in order to analyse the effect of strain/stress on the number, the amplitude and the symmetry of the energy gaps. Kurth F. et al. [112] developed this idea by studying the effect of disorder and impurity

scattering and Engelmann J. et al. [34] by studying the Ba-122 parent compound.
Three structures were measured by PCARS on $FeTe_{1-x}Se_x$ and two on $Ba(Fe_{1-x}Co_x)_2As_2$ samples. Two energy gaps in 11 systems with $\Delta_H \approx 1.75 k_B T_c$ and $\Delta_E \approx 2.75 k_B T_c$ were measured and a third structure ($\Delta^* \approx 6 k_B T_c$ that can be mistaken by a gap) was clearly visible. Different values were obtained in 122 system. One energy gap was measured with $2\Delta_S \approx 3.7 k_B T_c$ in 122 system. A second structure was measured in this compound with $2\Delta_L \approx 9 k_B T_c$ in 122 system. Despite the high value of the ratio (not so strange in Fe-based SCs) was considered an EBI structure because of the significant results obtained on single crystals measurements [66].
PCARS measurements performed both $FeTe_{1-x}Se_x$ and $Ba(Fe_{1-x}Co_x)_2As_2$ analysed within the Eliashberg theory agree to the strong-coupling nature of the Fe-based materials. Different energy values of the EBI structure in these compounds could be connected to the different SDW phase in the two materials. The decrease of the value of the interband coupling next to the AFM region probably due to the suppression of spin fluctuations clearly visible in $Ba(Fe_{1-x}Co_x)_2As_2$ thin films was not underlined from measurements on $FeTe_{1-x}Se_x$ compounds. Indeed the phase diagram obtained from $Fe_{1+\delta}Te_{1-x}Se_x$ discussed in literature [171] seems to be different from the 122 phase diagram generally reported [5, 11]: the first one contains a spin glass phase between the AFM and SC phase while the second one has a partial coexistence of the AFM and SC phase. More measurements will be carried out on different doping content Fe-based materials in order to analyze further in depth many points of this study.

Bibliography

[1] A. A. Golubov and I. Mazin. *Appl. Phys. Lett.*, 102:032601, 2013.

[2] D. Daghero and R.S. Gonnelli. *Supercond. Sci. Technol.*, 23:043001, 2010.

[3] Y. Kamihara, T. Watanabe, M. Hirano, and H. Hosono. *J. Am. Chem. Soc.*, 130: 3296, 2008.

[4] J. G. Bednorz and K. A. Mueller. *EPJ B*, 64:189–193, 1986.

[5] J. Paglione and R. L. Greene. *Nature Phys.*, 6:645–58, 2010.

[6] C. de la Cruz, Q. Huang, J. W. Lynn, J. Li, W. Ratcliff, J. L. Zarestky, H. A. Mook, G. F. Chen, J. L. Luo, N. L. Wang, and P. Dai. *Nature Lett.*, 453:899, 2008.

[7] Athena S. Sefat, Ashfia Huq, Michael A. McGuire, Rongying Jin, Brian C. Sales, David Mandrus, Lachlan M. D. Cranswick, Peter W. Stephens, and Kevin H. Stone. *Phys. Rev. B*, 78:104505, 2008.

[8] S. Sharma, S. Bharathi, A.and Chandra, V.R. Reddy, Pualraj S., Satya A.T., V.S. Sastry, Gupta A., and C.S. Sundar. *Phys. Rev. B*, 81:174512, 2010.

[9] L. Zhang and Singh D. J. *Phys. Rev. B*, 79:174530, 2009.

[10] Michael A. McGuire, David J. Singh, Athena S. Sefat, Brian C. Sales, and David Mandrus. *J. Solid State Chem.*, 182:2326, 2009.

[11] I. I. Mazin, T. P. Devereaux, R. Hackl, B. Muschler, J. G. Analytis, Jiun-Haw Chu, and I. R. Fisher. *Phys. Rev. B*, 82:180502(R), 2010.

[12] I. I. Mazin and J. Schmalian. *Physica C*, 469:614, 2009.

[13] D. J. Singh. *Physica C*, 469:418–424, 2009.

[14] T. Kondo, A. F. Santander-Syro, O. Copie, C. Liu, M. E. Tillman, E. D. Mun, J. Schmalian, S. L. Bud'ko, M. A. Tanatar, P. C. Canfield, and A. Kaminski. *Phys. Rev. Lett*, 101:147003, 2008.

[15] H. Ding, P. Richard, K. Nakayama, K. Sugawara, T. Arakane, Y. Sekiba, A. Takayama, S. Souma, T. Sato, T. Takahashi, Z. Wang, X. Dai, Z. Fang, G. F. Chen, J. L. Luo, and N. L. Wang. *Europhys. Lett.*, 83:47001, 2008.

[16] L. Zhao, W. Liu, H.and Zhang, J. Meng, X. Jia, G. Liu, G.F. Dong, X.and Chen, J.L. Luo, G. Wang, N.L.and Wang, Y. Zhou, Y. Zhu, X. Wang, Z. Zhao, Z. Xu, C. Chen, and X.J. Zhou. *Chin. Phys. Lett.*, 25:4402, 2008.

[17] L. Wray, D. Qian, D. Hsieh, Y. Xia, L. Li, J.G. Checkelsky, A. Pasupathy, C.V. Gomes, K.K.and Parker, A.V. Fedorov, G.F. Chen, J.L. Luo, A. Yazdani, N.P. Ong, N.L. Wang, and M.Z. Hasan. *Phys. Rev. B*, 78:184508, 2008.

[18] E. G. Maksimov, A. E. Karakozov, B. P. Gorshunov, A.S. Prokhorov, A. A. Voronkov, and E. S. Zhukova. *Physica C*, 263:510, 1996.

[19] A.I. Coldea, J.D. Fletcher, A. Carrington, J.G. Analytis, A.F. Bangura, J.-H. Chu, A.S. Erickson, I.R. Fisher, N.E. Hussey, and R.D. McDonald. *Phys. Rev. Lett.*, 101: 216402, 2008.

[20] L. Zhao, H. Liu, W. Zhang, J. Meng, X. Jia, G. Liu, X. Dong, G.F. Chen, J.L. Luo, N.L. Wang, G. Wang, Y. Zhou, Y. Zhu, X. Wang, Z. Zhao, Z. Xu, C. Chen, and X.J. Zhou. *Nature*, 455:81, 2008.

[21] S.E. Sebastian, J. Gillett, N. Harrison, P.H.C. Lau, C.H. Mielke, and G.G. Lonzarich. *J. Phys. Condens. Matter.*, 20:422203, 2008.

[22] A. Subedi, L. Zhang, D. J. Singh, and M. H. Du. *Phys. Rev. B*, 78:134514, 2008.

[23] Y Misuguchi and Y. Takano. *J. Phys. Soc.*, 79:102001, 2010.

[24] K. Nakayama, T. Sato, R. Richard, P. T. Kawahara, Y. Sekiba, T. Qian, G. F. Chen, J. L. Luo, N. L. Wang, H. Ding, and T. Takahashi. *Phys. Rev. Lett.*, 105:197001, 2010.

[25] A. D. Christianson, E. A. Goremychkin, R. Osborn, S. Rosenkranz, M. D. Lumsden, C. D. Malliakas, I. S. Todorov, H. Claus, D. Y. Chung, M. G. Kanatzidis, R. I. Bewley, and T. Guidi. *Nature*, 456:930–932, 2008.

[26] K. Terashima, Y Sekiba, J. H. Bowen, K. Nakayama, T. Kawahara, T. Sato, P. Richard, Y.-M. Xu, L. J. Li, G. H. Cao, Z.-A. Xu, H. Ding, and T. Takahashi. *Proc. Natl. Acad. Sci (USA)*, 106:7330, 2009.

[27] P. Richard, T. Sato, K. Nakayama, T. Takahashi, and H. Ding. *Rep. Prog. Phys.*, 74:124512, 2011.

[28] I. I. Mazin, D. J. Singh, M. D. Johannes, and M. H. Du. *Phys. Rev. Lett.*, 101: 057003, 2008.

[29] K. Kuroki, S. Onari, R. Arita, H. Usui, Y. Tanaka, H. Kontani, and H. Aoki. *Phys. Rev. Lett.*, 101:087004, 2008.

[30] A. M. Kadin. *J.Wiley & Sons Inc.*, 1999.

[31] P. Seide. *Supercond. Sci. Technol.*, 24:043001, 2011.

[32] K. Iida, J. Hänisch, S. Trommler, S. Haindl, F. Kurth, R. Hühne, L. Schultz, and B. Holzapfel. *Supercond. Sci. Technol.*, 24:125009, 2011.

[33] D. Daghero, P. Pecchio, F. Laviano, R. S. Gonnelli, F. Kurth, V. Grinenko, and Iida K. *Appl. Surf. Sci.*, 2014.

[34] J. Engelmann, V. Grinenko, P. Chekhonin, W. Skrotzki, W. D.V. Efremov, S. Oswald, K. Iida, R. Hühne, J. Hänisch, M. Hoffmann, F. Kurth, L. Schultz, and B. Holzapfel. *Nature Comm.*, 4:2877, 2013.

[35] P. Pecchio, D. Daghero, G. A. Ummarino, R. S. Gonnelli, Kurth F., and K. Holzapfel, B. Iida. *Phys. Rev. B*, 88:174506, 2013.

[36] R. S. Gonnelli, M. Tortello, D. Daghero, P. Pecchio, S. Galasso, V. A. Stepanov, Z. Bukovski, N. D. Zhigadlo, J. Karpinski, K. Iida, and B. Holzapfel. *J. Supercond. Nov. Magn.*, 26:1331, 2013.

[37] J. F. Annett. *Superconductivity, Superfluids and Condensates.* Oxford University Press, 2003.

[38] J. Bardeen, L. N. Cooper, and J. R. Schrieffer. *Phys. Rev.*, 108:1175–204, 1957.

[39] J. R. Waldram. *Superconductivity of metals and cuprates.* Insitute of Physics Publishing, 1996.

[40] M. A. Biondi, M. P. Garfunkel, and A. O. McCoubrey. *Phys. Rev.*, 108:495, 1957.

[41] X. H. Chen, T. Wu, G. Wu, R. H. Liu, H. Chen, and D. F. Fang. *Nature (London)*, 453:1224, 2008.

[42] R.A. Klemm, C.T. Rieck, and K. Scharnberg. *Phys. Rev. B*, 66:108, 2000.

[43] K.H. Bennemann and J.B. (Eds.) Ketterson. *The Physics of superconductors.* Springer, 2004.

[44] K. Suzuki, H. Usui, and K. Kuroki. *J. Phys. Soc. Jpn.*, 80:013710, 2011.

[45] J. K. Dong, S.Y. Zhou, T.Y. Guan, H. Zhang, Y. F. Dai, X. Qiu, X. F. Wang, Y. He, X. H. Chen, and S. Y. Li. *Phys. Rev. Lett.*, 104:087005, 2010.

[46] J.-Ph. Reid, A. Juneau-Fecteau, R. T. Gordon, S. René de Cotret, N. Doiron-Leyraud, X. G. Luo, H. Shakeripour, J. Chang, M. A. Tanatar, H. Kim, R. Prozorov, T. Saito, H. Fukazawa, Y. Kohori, K. Kihou, C. H. Lee, A. Iyo, H Eisaki, B. Shen, H.-H. Wen, and L. Taillefer. *Supercond. Sci. Technol.*, 25:084013, 2012.

[47] K. Hashimoto, M. Yamashita, S. Kasahara, Y. Senshu, N. Nakata, S. Tonegawa, K. Ikada, A. Serafin, A. Carrington, T. Terashima, H. Ikeda, T. Shibauchi, and Y. Matsuda. *Phys. Rev. B*, 81:220501, 2010.

[48] Y. Nakai, T. Iye, S. Kitagawa, K. Ishida, S. Kasahara, T. Shibauchi, Y. Matsuda, and T. Terashima. *Phys. Rev. B*, 81:020503(R), 2010.

[49] B. Muschler, W. Prestel, R. Hackl, T. P. Devereaux, J. G. Analytis, J.-H. Chu, and I. R. Fisher. *Phys. Rev. B*, 80:180510(R), 2009.

[50] J.-Ph. Reid, M. A. Tanatar, X. G. Luo, H. Shakeripour, N. Doiron-Leyraud, N. Ni, S. L. BudŠko, P. C. Canfield, R. Prozorov, and Louis Taillefer. *Phys. Rev. B*, 82: 064501, 2010.

[51] C.-T. Chen, C. C. Tsuei, M. B. Ketchen, Z.-A. Ren, and Z. X. Zhao. *Nature Phys.*, 6:260, 2010.

[52] T. Hanaguri, S. Niitaka, K. Kuroki, and H. Takagi. *Science*, 328:474, 2010.

[53] H. Suhl, B. T. Matthias, and L. R. Walker. *Phys. Rev. Lett.*, 3:552, 1959.

[54] V. A. Moskalenko. *Fiz. Met. i Met*, 4:503, 1959.

[55] A. A. Golubov and I. I. Mazin. *Physica C*, 243:153–159, 1995.

[56] R. S. Gonnelli, G. A. Ummarino, D. Daghero, A. Calzolari, and V. A. Stepanov. *J. Mod. Phys. B*, 16:1553, 2002.

[57] A. A. Golubov, J. Kortus, O. V. Dolgov, O. Jepsen, Y. Kong, O. K. Andersen, B. J. Gibson, K. Ahn, and R. K. Kremer. *J. Phys.: condens. matter*, 14:1353, 2002.

[58] O. V. Dolgov, I.I. Mazin, D. Parker, and Golubov. *Phys. Rev. B*, 79:060502(R), 2009.

[59] G. A. Ummarino, M. Tortello, D. Daghero, and R. S. Gonnelli. *Phys. Rev. B*, 80: 172503–1–4, 2009.

[60] Z.J Yao, J.X. Li, and Z.D. Wang. *New J. Phys.*, 11:025009, 2009.

[61] M. D. Lumsden and A. D. Christianson. *J. Phys.: Condens. Matter*, 22:203203, 2010.

[62] I. K. Yanson. *Sov. Phys. JETP*, 39:506–513, 1974.

[63] I. K. Yanson, V. V. Fisun, A. G. M. Jansen, P. Wyder, P. C. Canfield, B. K. Cho, C. V. Tomy, and D. McK. Paul. *Phys. Rev. Lett.*, 78:935, 1997.

[64] Yu. G. Naidyuk and I. K. Yanson. *Point Contact Spectroscopy*, volume 145 of *Springer Series in Solid-State Sciences*. Springer, 2004.

[65] E. L. Wolf. *Principles of electron tunneling spectroscopy*. Oxford University Press, New York, 1985.

[66] M. Tortello, D. Daghero, G. A. Ummarino, V. A. Stepanov, J. Jiang, J. D. Weiss, E. E. Hellstrom, and R. S. Gonnelli. *Phys. Rev. Lett.*, 105:237002, 2010.

[67] G.A. Ummarino, Sara Galasso, and A Sanna. *J. Phys. Cond. Matt.*, 25(20):205701, 2013.

[68] D. Daghero, M. Tortello, G.A. Ummarino, and R. S. Gonnelli. *Rep. Prog. Phys.*, 74: 124509, 2011.

[69] G. A. Ummarino. *Phys. Rev. B*, 83:092508–1–4, 2011.

[70] L. Boeri, Calandra M., Mazin I., O. V. Dolgov, and Mauri F. *Phys. Rev. B*, 82: 020506–1–4, 2010.

[71] R. Mittal, Y. Su, S. Rols, T. Chatterji, S. L. Chaplot, H. Schober, M. Rotter, D. Johrendt, and Th. Brueckel. *Phys. Rev. B*, 78:104514, 2008.

[72] P. Popovich, A. V. Boris, O. V. Dolgov, A. A. Golubov, D. L. Sun, C. T. Lin, R. K. Kremer, and B. Keimer. *Phys. Rev. Lett.*, 105:027003, 2010.

[73] G. A. Ummarino, D. Daghero, M. Tortello, and R. S. Gonnelli. *J. Supercond. Nov. Magn.*, 24:247–253, 2011.

[74] G. A. Ummarino. *J. Supercond. Nov. Magn.*, 25:1333–1337, 2012.

[75] D. Daghero, M. Tortello, G.A. Ummarino, V. A. Stepanov, F. Bernardini, M. Tropeano, M. Putti, and R. S. Gonnelli. *Supercond. Sci. Technol.*, 25:084012, 2012.

[76] D. S. Inosov, J. T. Park, P. Bourges, D. L. Sun, Y. Sidis, A. Schneidewind, K. Hradil, D. Haug, C. T. Lin, B: Keimer, and V. Hinkov. *Nature Phys.*, 6:178–81, 2010.

[77] P. J. Hirschfeld, M. M. Korshunov, and I. I. Mazin. *Rep. Prog. Phys.*, 74:124508, 2011.

[78] A. Andreev. *Zh. Eksp. Teor. Fiz.*, 46:1823, 1964. Engl. Transl. Sov. Phys.-JETP **19**, 1228 (1974).

[79] P. De Gennes. Benjamin, New York, 1966.

[80] G. E. Blonder, M. Tinkham, and T. M. Klapwijk. *Phys. Rev. B*, 25:4515, 1982.

[81] S. Kashiwaya, Y. Tanaka, M. Koyanagi, and K. Kajimura. *Phys. Rev. B*, 53:2667, 1996.

[82] G.E. Blonder and M. Tinkham. *Phys. Rev. B*, 27:112, 1983.

[83] R. C. Dynes, V. Narayanamurti, and J. P. Garno. *Phys. Rev. Lett.*, 41:1509, 1978.

[84] A. Plecenik, M. Grajcar, Š. Beňačka, P. Seidel, and A. Pfuch. *Phys. Rev. B*, 49: 10016, 1994.

[85] H. Srikanth and A. K. Raychaudhuri. *Physica C*, 190:229, 1992.

[86] I. I. Mazin. *Phys. Rev. Lett.*, 83:1427, 1999.

[87] A. Brinkman, A. A. Golubov, H. Rogalla, O. V. Dolgov, J. Kortus, Y. Kong, O. Jepsen, and O. K. Andersen. *Phys. Rev. B*, 65:180517, 2002.

[88] A. Y. Liu, I. I. Mazin, and J. Kortus. *Phys. Rev. Lett.*, 87:87005, 2001.

[89] R. S. Gonnelli, D. Daghero, A. Calzolari, G. A. Ummarino, V. Dellarocca, V. A. Stepanov, S. M. Kazakov, J. Karpinski, C. Portesi, E. Monticone, V. Ferrando, and C. Ferdeghini. *Supercond. Sci. Technol.*, 17:S93, 2004.

[90] *Low Level Measurements Handbook*. Keithley, 2013.

[91] L. J. van der Pauw. *Philips Res. Repts.*, 13:1, 1958.

[92] L. J. van der Pauw. *Philips Tech.Rev.*, 20:220, 1958.

[93] D.W. Koon. *Rev. Sci. Instrum.*, 60:271, 1989.

[94] D.W. Koon, Bahl A.A., and Duncan E.O. *Rev. Sci. Instrum.*, 60:275, 1989.

[95] Mosqueira J., Pomar A., Diaz A., Veira J. A., and Vidal F. *Physica C*, 34:225, 1994.

[96] D.W. Koon and C.J. Knickerbocker. *Rev. Sci. Instrum.*, 67:4282, 1996.

[97] D.W. Koon and Chan W.K. *Rev. Sci. Instrum.*, 69:4218, 1996.

[98] A. G. M. Jansen, A. P. van Gelder, and P. Wyder. *J. Phys. C: Solid state Phys.*, 13: 6073, 1980.

[99] Yu. V. Sharvin. 48:984, 1965. Engl. Transl. Sov. Phys.-JETP **21**, 655 (1965).

[100] A. M. Duif, A. G. M. Jansen, and P. Wyder. *J. Phys.: Condens. Matter*, 1:3157–3189, 1989.

[101] V. Baltz, A. D. Naylor, K. M. Seemann, W. Elder, S. Sheen, K. Westerholt, H. Zabel, G. Burnell, C. H. Marrows, and B. J. Hickey. *J. Phys. Condens. Matter*, 21:095701, 2009.

[102] G. Wexler. *Proc. Phys. Soc. London*, 89:927, 1966.

[103] D. Daghero, R. S. Gonnelli, G. A. Ummarino, A. Calzolari, V. Dellarocca, V. A. Stepanov, S. M. Kazakov, J. Jun, and J. Karpinski. *J. Phys. Chem. Solids*, 67:424, 2006.

[104] G. Deutscher. *Rev. Mod. Phys.*, 77:109–35, 2005.

[105] Yu. G. Naidyuk and I. K. Yanson. page arXiv:0312016, 2008.

[106] G. Sheet, S. Mukhopadhyay, and P. Raychaudhuri. *Phys. Rev. B*, 69:134507, 2004.

[107] I. I. Mazin, A. A. Golubov, and B. Nadgorny. *J. Appl. Phys.*, 89:7576, 2001.

[108] G. T. Woods, R. J. Soulen, I. I. Mazin, B. Nadgorny, M. S. Osofsky, J. Sanders, H. Srikanth, W. F. Egelhoff, and R. Datla. *Phys. Rev. B*, 70:054416, 2004.

[109] T. Y. Chen, S. X. Huang, and C. L. Chien. *Phys. Rev. B*, 81:214444, 2010.

[110] S. DŽring, S. Schmidt, S. Gottwals, F. Schmidl, V. Tympel, I. MŽnch, F. Kurth, K. Iida, B. Holzapfel, and P. Seidel. *J. Phys. Conf. Series*, 507:012008, 2014.

[111] S. Kashiwaya and Y. Tanaka. *Rep. Prog. Phys.*, 63:1641Ű1724, 2000.

[112] F. Kurth, E. Reich, J. Hänisch, A. Ichinose, I Tsukada, R. Hühne, S. Trommler, J. Engelmann, L. Schultz, B. Holzapfel, and K. Iida. *Appl. Phys. Lett.*, 102:142601, 2013.

[113] F. Kurth, K. Iida, S. Trommler, J. Hänisch, K. Nenkov, J. Engelmann, S. Oswald, J. Werner, L. Schultz, B Holzapfel, and S. Haindl. *Supercond. Sci. Technol.*, 26: 025014, 2013.

[114] N. Ni, M. E. Tillman, J. Q. Yan, A. Kracher, S. T. Hannahs, S. L. BudÕko, and P. C. Canfield. *Phys. Rev. B*, 78:214515, 2008.

[115] J.-H. Chu, J.G. Analytis, C. Kucharczyk, and I.R. Fisher. *Phys. Rev. B*, 79:014506, 2009.

[116] F. L. Ning, K. Ahilan, T. Imai, A. S. Sefat, M. A. McGuire, D. Sales, B. C.and Mandrus, P. Cheng, B. Shen, and H.-H Wen. *Phys. Rev. Lett.*, 104:037001, 2010.

[117] G. F. Chen, Z. Li, J. Dong, G. Li, W. Z. X. Hu, X. H. Zhang, D. Song, P. Zheng, N. L. Wang, and J. L. Luo. *Phys. Rev. B*, 88:224512, 2008.

[118] P. Mele. *Sci. Technol. Adv. Mater.*, 13:054301, 2012.

[119] K. Iida, J. Hänisch, R. Hühne, F. Kurth, M. Kidszun, S. Haindl, J. Werner, L. Schultz, and B. Holzapfel. *Appl. Phys. Lett*, 95:192501, 2009.

[120] J. S. Kim, R. Jin, L. R. Walker, J. Y. Howe, M. H. Pan, J. F. Wendelken, J.R. Thompson, A. S. Sefat, M. A. McGuire, B. C. Sales, D. Mandrus, and A. P. Li. *Phys. Rev. B*, 80:214518, 2009.

[121] S. C. Speller, T. B. Britton, G. M. Hughes, A. Krzton-Maziopa, E. Pomjakushina, K. Conder, A. T. Boothroyd, and C. R. M. Grovenor. *Supercond.Sci.Technol.*, 25: 084023, 2012.

[122] R. Vaglio, C. Attanasio, L. Maritato, and A. Ruosi. *Phys. Rev. B*, 47:15302, 1993.

[123] K. Iida, F. Kurth, V. Grinenko, J. Engelmann, M. Larger, P. Pecchio, D. Daghero, R.S. Gonnelli, R. Hühne, J. Hänisch, S. Aswartham, M. Erge, I. Mönch, S. Wurmehl, B. Büchner, L. Schultz, and B. Holzapfel. *IUMRS-International Conference in Asia (IUMRS-ICA 2014)*, 2014.

[124] T. Plecenik, M. Gregor, R. Sobota, M. Truchly, L. Satrapinskyy, F. Kurth, B. Holzapfel, K. Iida, P. Kus, and A. Plecenik. *Appl. Phys. Lett.*, 103:052601, 2013.

[125] Yu. G. Naidyuk, O. E. Kvitnitskaya, L. V. Tiutrina, I. K. Yanson, G. Behr, G. Fuchs, S.-L. Drechsler, K. Nenkov, and L. Schults. *Phys. Rev. B*, 84:094516, 2011.

[126] H. Z. Arham, C. R. Hunt, J. Gillett, S. D. Das, S. E. Sebastian, D. Y. Chung, M. G. Kanatzidis, and L. H. Greene. arXiv:1307.1908, 2013.

[127] G. Sheet, M. Mehta, D. A. Dikin, S. Lee, C.W. Bark, J. Jiang, J. D. Weiss, E. E. Hellstrom, M. S. Rzchowski, C. B. Eom, and V. Chandrasekhar. *Phys. Rev. Lett.*, 105:167003, 2010.

[128] S. Graser, A. F. Kemper, T. A. Maier, H.-P. Cheng, P. J. Hirschfeld, and D. J. Scalapino. *Phys. Rev. B*, 81:21450, 2010.

[129] D. V. Efremov, M. M. Korshunov, O. V. Dolgov, A. A. Golubov, and P. J. Hirschfeld. *Phys. Rev. B*, 84:180512(R), 2011.

[130] F. Hardy, P. Burger, T. Wolf, R. A. Fisher, P. Schweiss, P. Adelmann, R. Heid, R. Fromknecht, R. Eder, D. Ernst, H. v. Löhneysen, and C. Meingast. *Europhys. Lett.*, 91:47008, 2010.

[131] J. J. Tu, J. Li, W. Liu, and A. Punnoose. *Phys. Rev. B*, 82:174509, 2010.

[132] E. G. Maksimov, A. E. Karakozov, B. P. Gorshunov, A.S. Prokhorov, A. A. Voronkov, and E. S. Zhukova. *Phys. Rev. B*, 83:140502(R), 2011.

[133] T Fisher, A.V. Pronin, J. Wosnitza, K. Iida, F. Kurth, S. Haindl, L. Schultz, B. Holzapfel, and E. Schachinger. *Phys. Rev. B*, 82:224507, 2010.

[134] E. van Heumen, Y. Huang, S. de Jong, A. B. Kuzmenko, M. S. Golden, and D. van der Marel. *Eur. Phys. Lett,*, 90:37005, 2010.

[135] A. Perucchi, L. Baldassarre, B. Joseph, S. Lupi, S. Lee, C. B. Eom, J. Jiang, J. D. Weiss, E. E. Hellstrom, and P. Dore. *Eur. Phys. J. B*, 86:274, 2013.

[136] P. Samuely, Z. Pribulová, P. Szabó, G. Pristáš, S. L. Bud'ko, and P. C. Canfield. *Physica C*, 469:507, 2009.

[137] D. Nakamura, Y. Imai, A. Maeda, T. Katase, H. Hiramatsu, and H. Hosono. *Physica C*, 471:634, 2011.

[138] Yi Yin, M. Zech, T. L. Williams, X. F. Wang, X. H. Chen, and J. E. Hoffman. *Phys. Rev. Lett.*, 102:097002, 2009.

[139] G. M. Eliashberg. *Sov. Phys. JETP*, 11:696, 1963.

[140] I. I. Mazin. private communication, 2012.

[141] D. J. Singh and M.-H. Du. *Phys. Rev. Lett.*, 100:237003, 2008.

[142] D. Daghero, M. Tortello, P. Pecchio, V. A. Stepanov, and R. S. Gonnelli. Low. Temp. Phys., 2013.

[143] R. S. Gonnelli, M. Tortello, D. Daghero, R. K. Kremer, Z. Bukovski, N. D. Zhigadlo, and J. Karpinski. *Supercond. Sci. Technol.*, 25:065007, 2012.

[144] P. Samuely, P. Szabó, Z. Pribulová, M.E. Tillman, S. L. Bud'ko, and P. C. Canfield. *Supercond. Sci. Technol.*, 22:014003, 2009.

[145] L. Fang, H. Luo, P. Cheng, Z. Wang, Y. Jia, G. Mu, B. Shen, I. I. Mazin, L. Shan, C. Ren, and H. H. Wen. *Phys. Rev. B*, 80:140508(R), 2009.

[146] W. K. Park, C. R. Hunt, H. Z. Arham, Z. J. Xu, J. S. Wen, Z. W. Lin, Q. Li, G. D. Gu, and L. H. Greene. Preprint at arXiv:1005.0190, 2010.

[147] T. Kato, Y. Mizuguchi, T. Machida, H. Sakata, and Y. Takano. *Phys. Rev. B*, 80: 180507(R), 2009.

[148] C. T. Wu, H.H. Chang, J. Y. Luo, F. C. Hsu, T.K. chen, M.J. Wang, and M. K. Wu. *Appl. Phys. Lett.*, 96:122506, 2010.

[149] C. C. Homes, A. Akrap, J. S. Wen, Z. J. Xu, Z. W. Lin, Q. Li, and G. D. Gu. *Phys. Rev. B*, 81:180508(R), 2010.

[150] M. Bendele, S. Weyeneth, R. Puzniak, A. Maisuradze, E. Pomjakushina, K. Conder, V. Pomjakushin, H. Luetkens, S. Katrych, A. Wisniewski, R. Khasanov, and H. Keller. *Phys. Rev. B*, 81:224520, 2010.

[151] H. Miao, P. Richard, Y. Tanaka, K. Nakayama, T. Qian, K. Umezawa, T. Sato, Y. M. Xu, Y. B. Shi, N. Xu, X. P. Wang, P. Zhang, H. B. Yang, Z. J. Xu, J. S. Wen, G. D. Gu, X. Dai, J. P. Hu, T. Takahashi, and H. Ding. *Phys. Rev. B*, 85:094506, 2012.

[152] J. X. Yin, Z. Wu, J. H. Wang, Z. Y. Ye, J. Gong, X. Y. Hou, L. Shan, A. Li, X. J. Liang, X. X. Wu, J. Li, C. S. Ting, Z. Wang, J. P. Hu, P. H. Hor, H. Ding, and S. H. Pan. *arXiv:1403.10270*, 2014.

[153] B. Zeng, G. Mu, H. Luo, T. Xiang, I. Mazin, H. Yang, L. Shan, C. Ren, P. Dai, and H. H. Wen. *Nat. Commun.*, 1:112, 2010.

[154] H. Kim, C. Martin, R. T. Gordon, M. A. Tanatar, J. Hu, B. Qian, Z. Q. Mao, R. Hu, C. Petrovic, N. Salovich, R. Giannetta, and R. Prozorov. *Phys. Rev. B*, 81: 180503(R), 2010.

[155] A. Ichinose, F. Nabeshima, I. Tsukada, M. Hanawa, S. Komiya, T. Akiike, Y. Imai, and A. Maeda. 26:075002, 2013.

[156] Y. Imai, T. Akiike, M. Hanawa, I. Tsukada, A. Ichinose, A. Maeda, T. Hikage, T. Kawaguchi, and H. Ikuta. *Appl. Phys. Express.*, 3:043102, 2010.

[157] I. Tsukada, M. Hanawa, T. Akiike, F. Nabeshima, Y. Imai, A. Ichinose, S. Komiya, T. Hikage, T. Kawaguchi, H. Ikuta, and A. Maeda. *Appl. Phys. Express*, 4:053101, 2011.

[158] M. R. Cimberle, C. Ferdeghini, G. Grassano, D. MarrŐ, M. Putti, A.S. Siri, and F. Canepa. *IEEE Trans. Appl. Supercond.*, 9:1727, 1999.

[159] E. Bellingeri, I. Pallecchi, R. Buzio, A. Gerbi, D. MarrŔ, M. R. Cimberle, M. Tropeano, M. Putti, A. Palenzona, S. Kaciulis, and C. Ferdeghini. *J. Supercond. Nov. Magn.*, 24:34–41, 2011.

[160] S. Komiya, M. Hanawa, I. Tsukada, and A. Maeda. *J. Phys. Soc. Jpn.*, 82:064710, 2013.

[161] B. C. Sales, A. S. Sefat, M. A. McGuire, R. Y. Jin, D. Mandrus, and Y. Mozharivskyj. *Phys. Rev B*, 79:094521, 2009.

[162] F. Nabeshima, Y. Imai, M. Hanawa, I. Tsukada, and A. Maeda. *Appl. Phys. Lett.*, 103:172602, 2013.

[163] E. Bellingeri, I. Pallecchi, R. Buzio, A. Gerbi, D. MarrŔ, M. R. Cimberle, M. Tropeano, M. Putti, A. Palenzona, and C. Ferdeghini. 96:102512, 2010.

[164] I. Tsukada, M. Hanawa, S. Komiya, R. Tanaka, Y. Imai, and A. Maeda. *Phys. Rev B*, 81:054515, 2010.

[165] Q. Li, W. Si, and I. K. Dimitrov. *Rep. Prog. Phys.*, 74:124510, 2011.

[166] J. T. Park, D. S. Inosov, Ch. Niedermayer, G. L. Sun, D. Haug, N. B. Christensen, R. Dinnebier, A. V. Boris, A. J. Drew, L. Schulz, T. Shapoval, U. Wolff, V. Neu, Xiaoping Yang, C. T. Lin, B. Keimer, and V. Hinkov. *Phys. Rev. Lett.*, 102:117006, 2009.

[167] Y. Qiu, W. Bao, Y. Zhao, C. Broholm, V. Stanev, Z. Tesanovic, Y. C. Gasparovic, S. Chang, J. Hu, B. Qian, M. Fang, and Z. Mao. *Phys. Rev. Lett.*, 103:067008, 2009.

[168] R. Hu, S. Ran, S.L. Bud'ko, W. E. Straszheim, and P. C. Canfield. Unpublished, arXiv:1111.7034, Nov 2011.

[169] A. Maeda, F. Nabeshima, H. Takahashi, T. Okada, Y. Imai, I. Tsukada, M. Hanawa, S. Komiya, and A. Ichinose. *Appl. Surf. Sci.*, in press, 2014.

[170] S. Trommler, R Hühne, J. Hänisch, E. Reich, K. Iida, S. Haindl, V. Matias, L. Schultz, and B. Holzapfel. *Appl. Phys. Lett.*, 100:122602, 2012.

[171] D.C. Jonhston. *Advances in Physics*, 59:803 – 1061, 2010.